Lecture Note on
Strong Motion Seismology

Kojiro Irikura (Aichi Institute of Technology and Kyoto University)
Hiroe Miyake (Earthquake Research Institute, University of Tokyo)

Preface

Accumulated strong ground motion data provides researchers with very important information about the rupture processes of earthquakes, wave-propagation in real complex underground structures, simulation of ground motions, and mechanisms of structural damage due to ground shaking. Rapid progress has been achieved in the basic theory and application of this data for simulating ground motions and structural responses during large earthquakes. We here propose a "recipe" for the prediction of strong ground motion based on the most recent findings of seismology and earthquake engineering. This lecture note focuses on summarizing recent developments in strong motion seismology.

This lecture note consists of five chapters. Chapter 1 contains an Introduction of Strong Motion Seismology. Chapter 2 gives the basic theory of the "Empirical Green's Function Method" for simulating strong ground motions from a large earthquake. This method was developed by combining the representation theory for estimating ground motions generated from a source fault and the similarity law of earthquakes for fault parameters and ground motion generation. Chapter 3 shows the methodology for simulating long period ground motion using the three-dimensional finite difference method. An example is given involving the numerical calculation of long period ground motions in the Osaka basin from great subduction-zone earthquakes occurring along the Nankai trough. Chapter 4 shows a hybrid method for simulating strong ground motion from a large earthquake. Long-period and short-period ground motions from the source faults for a large event are calculated using the three-dimensional finite difference method and the stochastic Green's function method. Then, the broadband ground motions from large events are synthesized, summing the long-period and short-period ground motions with a matching filter. Chapter 5 summarizes the "recipe" for predicting strong ground motions from the source faults of specific earthquakes. The "recipe" is used to create fault models for predicting strong ground motion by combining the information from the geo-morphological and geological surveys of active faults with the scaling relations of the fault parameters.

We hope the basic theory and methodology described in this lecture note are useful in helping graduate-course students and young researchers and engineers to understand strong motion seismology.

This lecture note was completed only through the support of many people.

Chapter 2 was based on a paper written in collaboration with Tomotaka Iwata and Chapter 3 was based on a paper written in collaboration with Hidenori Kawabe and Kazuhiro Kamae. Chapter 4 was based on a paper written in collaboration with Kazuhiro Kamae. Chapter 5 was done as a part of the governmental project, "National Seismic Hazard Maps for Japan," sponsored by the Headquarters for Earthquake Research Promotion of Japan under the Ministry of Education, Culture, Sports, Science, and Technology. We express deep thanks for allowing us to refer to the results and figures of the Seismic Hazard Map presented by the Earthquake Research Committee.

Our work has been performed through the support given to our research projects over the years, including the Grants-in-Aids for Scientific Research from the Japan Society for the Promotion of Science, the Special Project for Earthquake Disaster Mitigation in Urban Areas from the Ministry of Education, Culture, Sports, Science, and Technology of Japan, and Special Coordination Funds for Promoting Science and Technology from the Japan Science and Technology Agency.

This lecture note was written for courses on Seismology and Earthquake Engineering at the International Institute of Seismology and Earthquake Engineering, Building Research Institute, Japan. We acknowledge the great support received from Toshiaki Yokoi, Chief Research Scientist, Building Research Institute, Japan.

Kojiro Irikura

Chapter 1: Introduction

Strong Motion Seismology is defined as a science and technology based on strong motion data and the earthquake disaster records near earthquake sources. The objectives of strong motion seismology include the following three basic subjects: a study of the source dynamics of the ground motions generated from seismic faults; the seismic-wave propagation effects due to complex geological structures in the propagation-path from source to site, including wave attenuation and scattering; and the amplification and de-amplification of seismic motions due to surface geology and topography, including the nonlinear behavior of soft soils in relation to strong motions. The goal is to develop methodologies for predicting strong ground motions from seismic sources related to active faults and subduction-zones with a high probability of earthquake occurrence in order to mitigate earthquake disasters.

The Kobe earthquake of 17 January 1995, had a serious impact, not only on Japan, but also worldwide. This earthquake was medium in magnitude, M_w 6.9, but the damage encountered was enormous, the worst in Japan since the great Kanto earthquake of 1923. The occurrence of this earthquake disaster was a great shock to earthquake scientists and engineers. They were reminded that earthquake science and engineering have not been sufficiently developed to provide the scientific support needed to prevent such disasters.

There is an obvious need for strong motion data to make clear why and how such heavy damage is caused during earthquakes. However, back then, there were very few strong motion observation stations in the Kobe region, or anywhere in Japan. This made it difficulty to study the characteristics of strong ground motions and the causes of the structural damage during the Kobe earthquake. Since this earthquake, strong motion networks, such as the K-NET and KiK-net, have been steadily constructed nationwide by local governments, as well as by the central government.

One of the lessons that we learned from the 1995 Kobe earthquake is the importance of evaluating strong ground motions for future earthquakes to mitigate the earthquake damage in urbanized areas surrounded by active faults and located close to subduction-zone earthquakes. The basic preparation policy for earthquake hazards in Japan was defined as the 1999 fundamental mission statement governing earthquake research over the next ten years as, “The promotion of earthquake research -- comprehensive basic policies for the promotion of seismic research through the

observation, measurement, and survey of earthquakes," established by the Headquarters for Earthquake Research Promotion of the Ministry of Education, Culture, Sports, Science, and Technology of Japan. It proposed the creation of seismic hazard maps by promoting a survey of active faults, along with the long-term evaluation of occurrence potentials and the prediction of strong ground motion.

Under the direction of their Headquarters, the Earthquake Research Committee began to make the seismic hazard maps from two different approaches, i.e., probabilistic and deterministic approaches. A probabilistic seismic hazard map shows the predicted likelihood of a ground motion level, such as a PGA, PGV, or seismic intensity, occurring in a given area within a set period of time. It provides important information for land use planning, structural design standards, and enlightening the public about seismic risks. A deterministic seismic hazard map shows the distribution of the ground motion level predicted for a specific earthquake fault. The strong ground motions at specific sites near the source fault should be estimated as time histories, as well as shaking levels. These ground motion time histories are effectively used for the nonlinear dynamic analyses of structures, which are needed to design earthquake-resistant buildings, bridges, lifelines, and so on. They are particularly important for securing the seismic safety of critical structures, such as nuclear power plants.

To obtain the ground motion time histories (waveforms) from individual specific earthquakes, we developed a new methodology, a "recipe for strong motion prediction." This recipe provides source modeling for specific earthquakes based on the source characteristics from the waveform inversion using strong motion data. The main features of the source models are characterized by three kinds of parameters, which we call: outer, inner, and extra fault parameters. The outer fault parameters are used to outline the overall picture of the target earthquake, such as the entire source area and seismic moment. The inner fault parameters are parameters that characterize the stress heterogeneity inside the fault area. The extra fault parameters are considered to complete the source model, such as the starting point and propagation pattern of the rupture. The validity and applicability of the procedures for characterizing the earthquake sources for strong ground prediction were examined in comparison with the observed records and broadband simulated motions for recent earthquakes, such as the 1995 Kobe and 2003 Tokachi-oki earthquakes. In future research, it would be beneficial in the prediction of strong ground motions to constrain the fault parameters by physically taking into account the source dynamics, as well as using the empirical data from past earthquakes.

Since the 1995 Kobe earthquake, other disastrous earthquakes have occurred,

killing about 17,000 people in Kocaeli, Turkey in 1999, about 22,300 people in Gujarat, India in 2001, 31,000 in Bam, Iran in 2003, and so on. Further, very recently, the 2004 Sumatra-Andaman earthquake that occurred to the northwest of Sumatra Island generated catastrophic tsunamis that hit coastal areas in the Indian Ocean, as well as Indonesia, with more than 200,000 people killed. The 2005 Kashmir earthquake that occurred in northern Pakistan flattened almost all of the houses and other structures in towns near the source area, killing more than 80,000 people. There were very few stations with seismometers for observing strong ground motions during those earthquakes. With no records, it is difficult to determine the near-field ground motions that caused the destruction of houses and other structures. Another consideration is that seismometers for tsunami warnings are distributed in a biased manner in the Pacific Ocean, with few in the Indian Ocean.

These facts again taught us the importance of strong motion prediction and seismic hazard analysis, as well as the need for tsunami warning systems to mitigate earthquake disasters.

Kojiro Irikura

Chapter 2. Empirical Green's Function Method for Simulating Strong Ground Motion

Summary

One of the most effective methods for simulating the broadband strong ground motion that comes from a large earthquake is to use the observation records from small earthquakes that have occurred around the source area for the large earthquake. The actual geological structure from the source to a site is generally more complex than that assumed in theoretical models. Hence, the actual ground motion is complicated, not only by the refraction and reflection due to the layer interfaces and ground surface, but also by the scattering and attenuation due to the lateral heterogeneities and anelastic properties of the propagation path. The complete modeling of the wave field in realistic media would be extremely difficult. A semi-empirical approach attempts to overcome such difficulties. This chapter describes the basic theory for simulating the strong ground motion of a large earthquake, incorporating the similarity law of earthquakes in the formulation. Then a description is given of source modeling and ground motion simulation applications using the empirical Green's function method for several earthquakes. This chapter was partially based on Miyake *et al*. (2003).

Formulation of the Empirical Green's Function Method

The technique by which waveforms for large events are synthesized follows the empirical Green's function method proposed by Hartzell (1978). Revisions have been made by Kanamori (1979), Irikura (1983, 1986), and others. We used the empirical Green's function method formulated by Irikura (1986), based on the scaling law of fault parameters for large and small events (Kanamori and Anderson, 1975) and the omega-squared source spectra (Aki, 1967). The waveform for a large event is synthesized by summing the records of small events with corrections for the difference in the slip velocity time function between the large and small events following the above scaling laws. This method does not require knowledge of the explicit shapes of the slip velocity time functions for the small events.

The numerical equations for summing the records of small events are,

$$U(t) = \sum_{i=1}^{N}\sum_{j=1}^{N} \frac{r}{r_{ij}} F(t) * \ (C \cdot \ u(t)) \tag{1}$$

$$F(t) = \delta(t - t_{ij}) + \frac{1}{n'} \sum_{k=1}^{(N-1)n'} [\delta\{t - t_{ij} - \frac{(k-1)T}{(N-1)n'}\}] \tag{2}$$

$$t_{ij} = \frac{r_{ij} - r_o}{V_s} + \frac{\xi_{ij}}{V_r} \tag{3}$$

where $U(t)$ is the simulated waveform for the large event, $u(t)$ is the observed waveform for the small event, N and C are the ratios of the fault dimensions and stress drops between the large and small events, respectively, and the * indicates convolution. $F(t)$ is the filtering function (correction function) used to adjust for the difference in the slip velocity time functions between the large and small events. V_s and V_r are the *S*-wave velocity near the source area and the rupture velocity on the fault plane, respectively. T is the risetime for the large event, defined as the duration of the filtering function $F(t)$ (in Fig. 1(b) and (c)). It corresponds to the duration of the slip velocity time function on a subfault from the beginning to the time before the tail starts. *n'* is an appropriate integer to weaken the artificial periodicity of n, and to adjust the interval of the tick to be the sampling rate. The other parameters are given in Fig 1(a).

Regarding the filtering function $F(t)$, Irikura *et al.* (1997) proposed a modification to equation (2) in order to prevent sag at multiples of $1/T$ (Hz) from appearing in the amplitude spectra. The discretized equation for the modified $F(t)$ is,

$$F(t) = \delta(t - t_{ij}) + \frac{1}{n'(1 - \frac{1}{e})} \sum_{k=1}^{(N-1)n'} [\frac{1}{e^{\frac{(k-1)}{(N-1)n'}}} \delta\{t - t_{ij} - \frac{(k-1)T}{(N-1)n'}\}]. \tag{4}$$

The shape of equation (4) is shown in Fig. 1(c). In Irikura (1986), the scaling parameters needed for this technique, N (integer value) and C, can be derived from the constant levels of the displacement and acceleration amplitude spectra of the large and small events with the formulas,

$$\frac{U_o}{u_o} = \frac{M_o}{m_o} = CN^3 \tag{5}$$

$$\frac{A_o}{a_o} = CN. \tag{6}$$

Here, U_0 and u_0 indicate the constant amplitude levels of the displacement spectra for the large and small events, respectively. M_0 and m_0 correspond to the seismic moments for the large and small events, respectively. A_0 and a_0 indicate the constant

amplitude levels of the acceleration spectra for the large and small events, respectively (Fig. 1(d), (e)).

N and *C* are derived from equations (5) and (6),

$$N = \left(\frac{U_0}{u_0}\right)^{\frac{1}{2}} \left(\frac{a_0}{A_0}\right)^{\frac{1}{2}} \tag{7}$$

$$C = \left(\frac{u_0}{U_0}\right)^{\frac{1}{2}} \left(\frac{A_0}{a_0}\right)^{\frac{3}{2}} \tag{8}$$

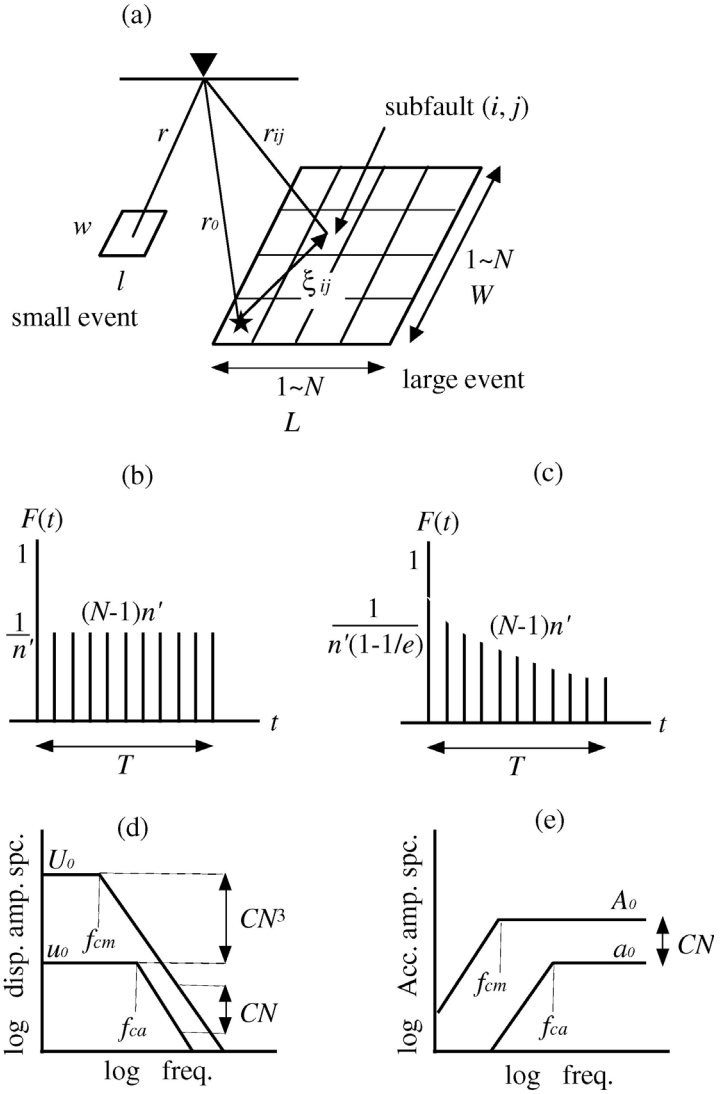

Figure 1. Schematic illustrations of the empirical Green's function method. (a) Fault areas of large and small events are defined as $L \times W$ and $l \times w$, respectively, where $L/l = W/w = N$. (b) Filtering function $F(t)$ (after Irikura, 1986) used to adjust for the difference in the slip velocity functions between the large and small events. This function is expressed as the sum of a delta and a boxcar function. (c) Modified filtering function (after Irikura *et al*., 1997) with an exponentially decaying

function instead of a boxcar function. T is the risetime for the large event. (d) Schematic displacement amplitude spectra following the omega-squared source scaling model, assuming a stress drop ratio C between the large and small events. (e) Acceleration amplitude spectra following the omega-squared source scaling model (after Miyake *et al*., 1999).

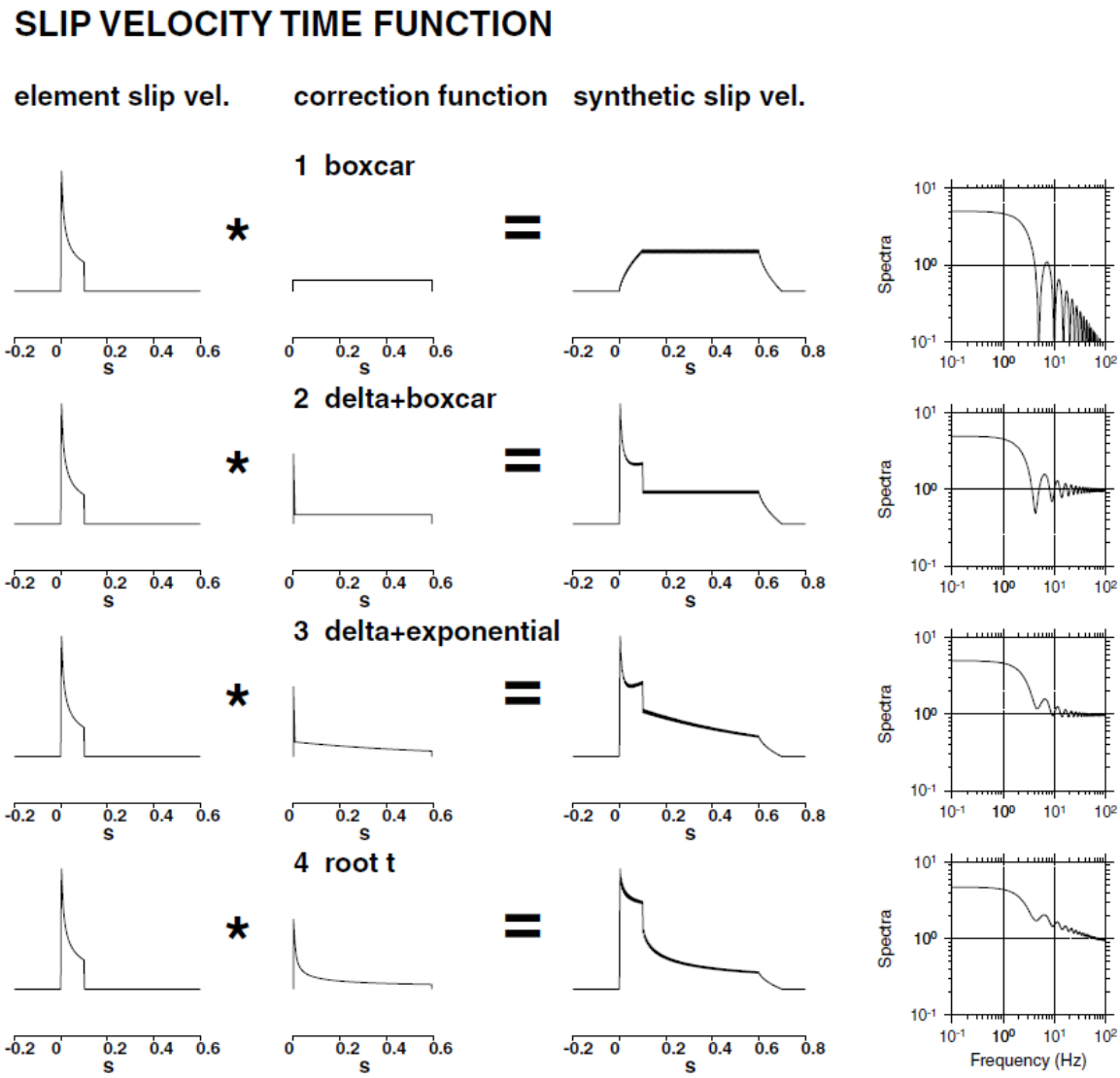

Figure 2. The effect of correction function $F(t)$ used in the empirical Green's function method on the synthetic slip velocity. The slip velocity of an element event is a Kostrov-type function with a finite slip duration (left). The correction function $F(t)$ is (a) a boxcar function, considering only the low-frequency scaling by Irikura (1983), (b) the conventional one (delta + boxcar functions) by Irikura (1986), (c) a modified one (delta + exponential-decay functions) by Irikura *et al*. (1997), or (d) a normalized Kostrov-type function with the finite slip duration given by Day (1982). The spectral shapes of the $F(t)$ correction functions are shown on the right (after Miyake *et al*., 1999).

Parameter Estimation for the Empirical Green's Function Method by the Source Spectral Fitting Method

For an objective estimation of parameters N and C, which are required for the empirical Green's function method of Irikura (1986), Miyake *et al*. (1999) proposed a source spectral fitting method. This method derives these parameters by fitting the observed source spectral ratio between the large and small events to the theoretical source spectral ratio, which obeys the omega-squared source model of Brune (1970, 1971).

The observed waveform $O(t)$ can be expressed as a convolution of the source effect $S(t)$, propagation path effect $P(t)$, and site amplification effect $G(t)$, assuming linear systems:

$$O(t) = S(t) * P(t) * G(t). \tag{9}$$

In the frequency domain, the observed spectrum $O(f)$ is expressed as a product of these effects:

$$O(f) = S(f) \cdot P(f) \cdot G(f). \tag{10}$$

From equation (10), the observed source amplitude spectral ratio of the large and small events for one station is,

$$\frac{S(f)}{s(f)} = \frac{O(f)/P(f)}{o(f)/p(f)} = \frac{O(f)\Big/\dfrac{1}{R}e^{\frac{-\pi fR}{Q_s(f)Vs}}}{o(f)\Big/\dfrac{1}{r}e^{\frac{-\pi fr}{Q_s(f)Vs}}}, \tag{11}$$

where the capital and lowercase letters indicate the factors for the large and small events, respectively. The propagation path effect is given by the geometrical spreading of the body waves and by a frequency-dependent attenuation factor $Q_s(f)$ for the S-waves.

The observed source amplitude spectral ratio for each station is first calculated using the mainshock and its aftershock. Then the observed source amplitude spectral ratio is divided into m windows in the frequency domain, in which the central frequency is f_i (i=1 to m), and the log-averages $S(f_i)/s(f_i)$ and log standard deviations $S.D.(f_i)$ are obtained (Fig. 4).

The equation for the amplitude spectra, based on the omega-squared source model by Brune (1970, 1971) is given as,

$$S(f) = \frac{M_0}{1 + \left(f/f_c\right)^2} \tag{12}$$

where f_c is the corner frequency. Using equation (12), the source spectral ratio function (SSRF) is,

$$SSRF(f) = \frac{M_0}{m_0} \cdot \frac{1 + (f/f_{ca})^2}{1 + (f/f_{cm})^2} \tag{13}$$

where M_0/m_0 indicates the seismic moment ratio between a large and small event at the lowest frequency, and f_{cm} and f_{ca} are the corner frequencies for the mainshock and aftershock, respectively. We searched for the minimum value of the weighted least-squares (equation (14)), applying the observed source amplitude spectral ratio, equation (11), to fit the SSRF (equation (13), Fig. 4) in the frequency domain for *nst* stations:

$$\sum_{i=1}^{nst} \left(\frac{SSRF(f_i) - S(f_i)/s(f_i)}{S.D.(f_i)} \right)^2 = min\,. \tag{14}$$

This method provides estimates of M_0/m_0, f_{cm}, and f_{ca}. The relationships between these parameters, N, and C are given as,

$$\frac{M_o}{m_o} = CN^3 \qquad (f \to 0) \tag{15}$$

$$\left(\frac{M_o}{m_o}\right)\left(\frac{f_{cm}}{f_{ca}}\right)^2 = CN \qquad (f \to \infty). \tag{16}$$

The high-frequency limit $(f \to \infty)$ corresponds to the frequency where the acceleration source spectrum is constant at frequencies of more than f_{ca} and less than f_{max} (f_{max} is the high-frequency cut-off for the constant level of the acceleration source spectrum).

According to equations (15) and (16), N and C are:

$$N = \frac{f_{ca}}{f_{cm}} \tag{17}$$

$$C = \left(\frac{M_o}{m_o}\right)\left(\frac{f_{cm}}{f_{ca}}\right)^3 \tag{18}$$

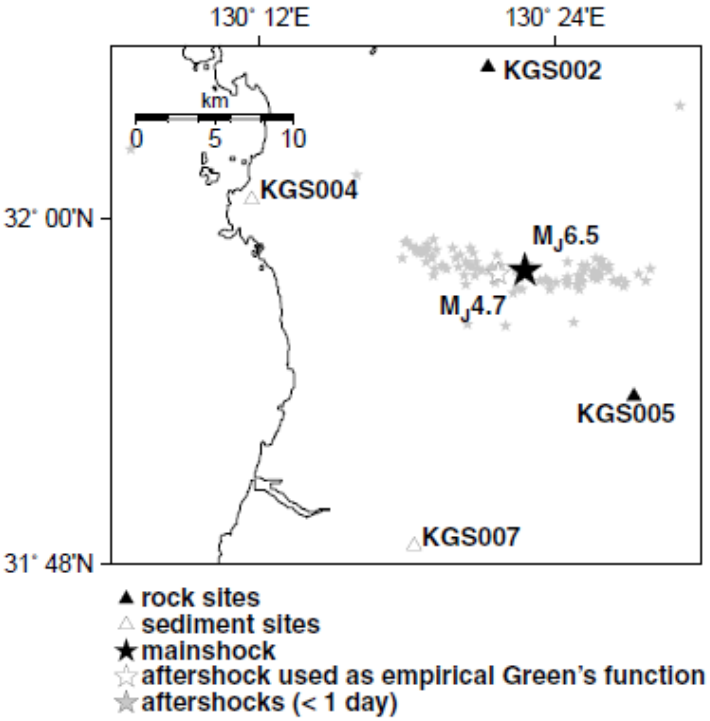

Figure. 3. Map showing the dataset used for the 1997 Kagoshima-ken Hokuseibu earthquake of 26 March 1997 (M_{JMA} 6.5), along with the aftershock distributions.

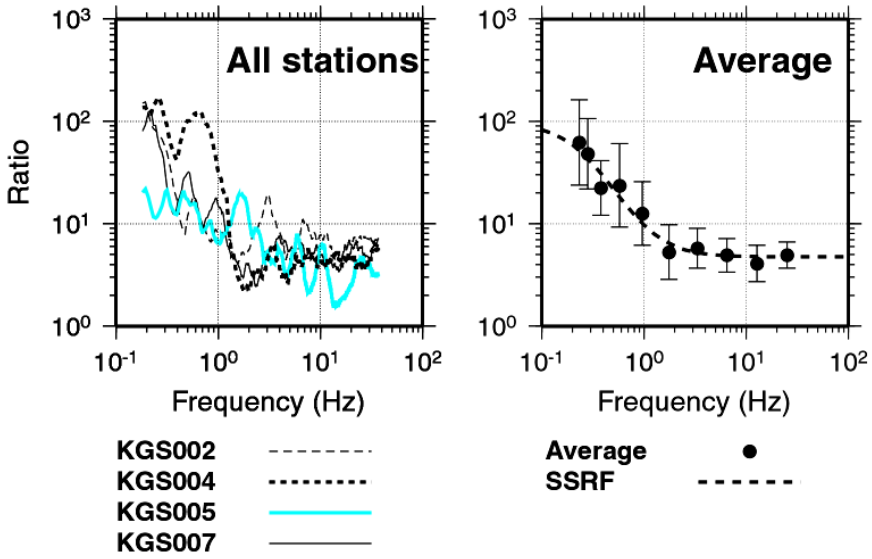

Figure 4. Source spectral ratios of the mainshock to aftershock records used as the empirical Green's function for the March 1997 Kagoshima-ken Hokuseibu earthquake. Left: Spectral ratios for all of the sites. Right: Comparison of average values of the observed ratios and best-fit source spectral ratio function (SSRF, broken line). Filled circles represent the average and bars the standard deviation of the observed ratios (after Miyake *et al*., 1999).

Near-Source Ground Motion Simulation to Estimate Strong Motion Generation Area

The modeling of the strong motion generation area using the empirical Green's function method is a useful technique for kinematically simulating both low- and high-frequency wave generation from the source using an appropriate filtering function, $F(t)$. The filtering function $F(t)$ provides the rupture growth with Kostrov-like slip velocity time functions.

We defined the "strong motion generation area" as the area characterized by a large uniform slip velocity within the total rupture area, which reproduces near-source strong ground motions of up to 10 Hz. The strong motion generation area of each mainshock was estimated by waveform fitting based on the empirical Green's function method. The low-frequency limit was constrained by the signal to noise level ratio of the small event record used as an empirical Green's function.

Numerous studies have performed ground motion simulations of target earthquakes using the empirical Green's function method to estimate the strong motion generation area. These simulations utilized acceleration, velocity, and displacement records from several stations surrounding the source area. The frequency range available for simulation was generally from 0.2 to 10 Hz, depending on the noise levels of the aftershock records. First, the *S*-wave arrival times of the velocity waveforms for the target and element earthquakes were set. Then 5 parameters, representing the size (length and width) and position (starting point of the rupture in the strike and dip directions) of the strong motion generation area, along with the risetime, were estimated to minimize the residuals of the displacement waveform and acceleration envelope fitting. The fitting was done by the Genetic Algorithm method (e.g., Holland, 1975) or forward modeling.

We followed this same approach to estimate the strong motion generation areas for the target earthquakes. Synthetic waveforms for the best source models fit the observed acceleration and velocity data well, while some displacement synthetics seemed to be smaller in amplitude than the observations (Fig. 5). The estimated strong motion generation area is shown in Fig. 6.

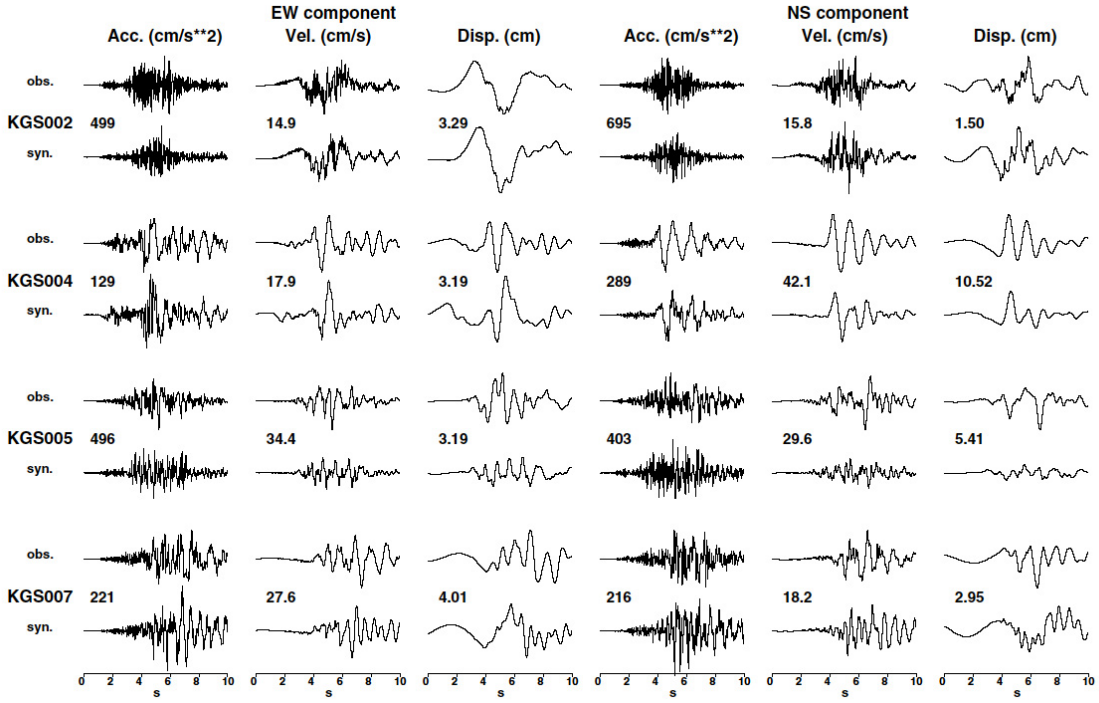

Figure 5. Comparison of observed and synthetic acceleration, velocity, and displacement waveforms for the March 1997 Kagoshima-ken Hokuseibu earthquake, at the four nearest K-NET stations. The numbers show the maximum amplitude values of the observed waveforms (after Miyake *et al*., 1999).

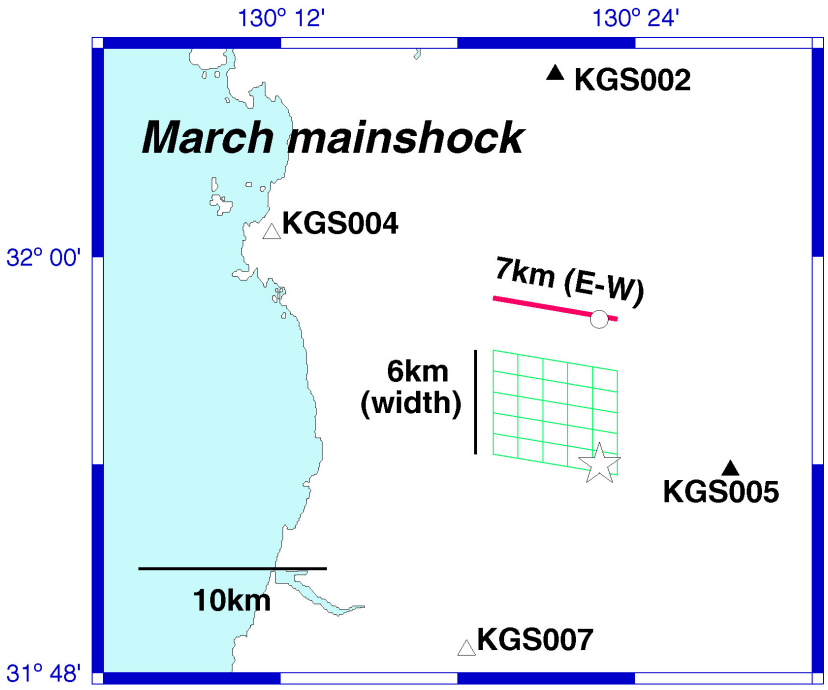

Figure 6. Strong motion generation area estimated by the empirical Green's function method for the March 1997 Kagoshima-ken Hokuseibu earthquake (after Miyake *et al*., 1999).

Relationship between Strong Motion Generation Area and Seismic Moment

For low-frequency source models, the heterogeneous slip distributions of crustal earthquakes have been analyzed to study the characteristics of the slip heterogeneity (e.g., Somerville *et al*., 1999; Mai and Beroza, 2000, 2002). Somerville *et al*. (1999) studied the slip characterizations by analyzing the heterogeneous slip distributions derived from waveform inversions of strong motion and teleseismic records in the low-frequency range. They found that the size of the asperities (areas of large slip) follow self-similar scaling with respect to seismic moment.

Miyake *et al.* (2003) compared the relationship between the size of the strong motion generation area (0.2-10 Hz) and seismic moment using the scaling relationship characterizing the slip distributions of crustal earthquakes (< 1 Hz) proposed by Somerville *et al*. (1999), as shown in Fig. 7. The strong motion generation area is proportional to $M_0^{2/3}$, indicating self-similar scaling for the range of seismic moments between 1.83×10^{16} Nm (M_w 4.8) to 1.38×10^{18} Nm (M_w 6.0). Since the absolute seismic moment values cannot be estimated from this procedure using the empirical Green's function itself, the seismic moments for the mainshocks were adopted as values, as determined by moment tensor inversions. This scaling of the strong motion generation area was close to that of the combined area of asperities reported by Somerville *et al*. (1999). The effective source area generating strong ground motions occupied almost a quarter of the total rupture area obtained by low-frequency waveform inversions. This scaling showed no clear dependence on the rupture propagation direction or focal mechanism. We made a comparison to the combined size of the three strong motion generation areas for the 1994 Northridge earthquake (M_w 6.6) (Kamae and Irikura, 1998b) and the 1995 Hyogo-ken Nanbu earthquake (M_w 6.8) (Kamae and Irikura, 1998a). These researchers used forward modeling to estimate the strong motion generation areas that best fit the velocity and acceleration waveforms. The sizes of their strong motion generation areas were also close to that of the combined area of asperities by Somerville *et al*. (1999).

For several earthquakes, the strong motion generation areas were located at almost the same positions as the asperity areas, based on the criteria of Somerville *et al*. (1999). These asperity areas were determined from the heterogeneous slip distribution results of waveform inversions in the frequency range of 0.1 to 0.5 Hz (Miyakoshi *et al*., 2000). Our analyses indicated that the large slip areas (asperities from low-frequency waveform inversion) and large slip velocity areas (strong motion generation areas in this study) occupied almost the same regions.

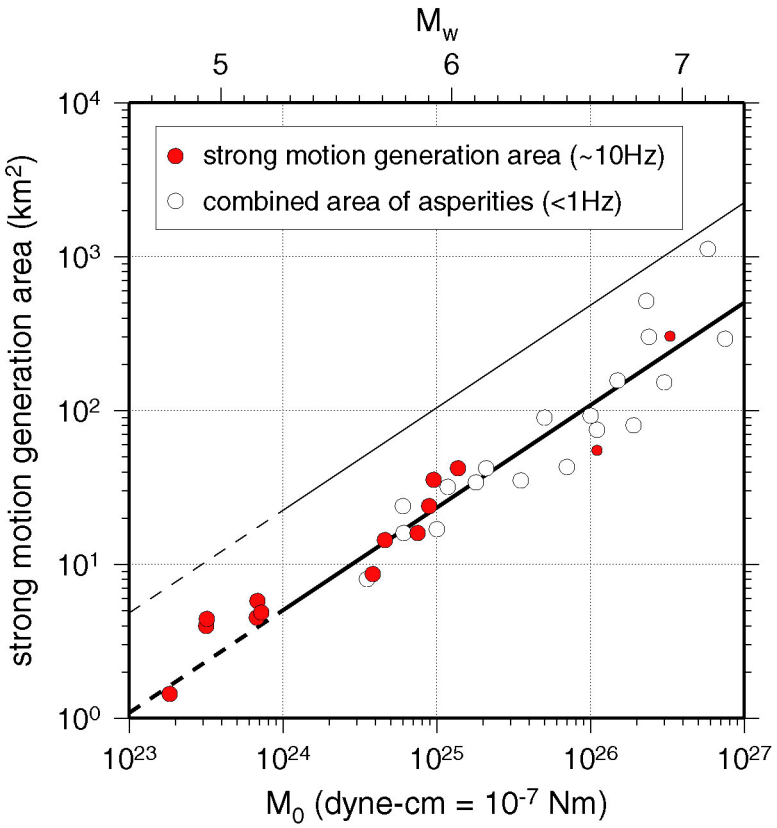

Figure 7. Scaling of the strong motion generation area to seismic moment. Solid and open circles, respectively, show the strong motion generation areas studied and the combined areas of asperities reported by Somerville *et al*. (1999). Thick and thin solid lines respectively correspond to the combined area of asperities and total rupture areas, as a function of the seismic moment (Somerville *et al*., 1999). Small solid circles are the areas for the 1994 Northridge earthquake (Kamae and Irikura, 1998b) and for the 1995 Hyogo-ken Nanbu earthquake (Kamae and Irikura, 1998a). The moment magnitude M_w was calculated according to Kanamori (1977) (after Miyake *et al*., 2003).

For broadband ground motion simulation, we proposed a characterized source model comprised of strong motion generation areas with large slip velocities and a background slip area with a small slip velocity. To show the importance of slip velocities in our source model, we simulated the ground motions for the 26 March 1997 Kagoshima-ken Hokuseibu earthquake in the frequency range of 0.2 to 10 Hz based on the empirical Green's function method, and compared the differences in the synthetic waveforms from the strong motion generation area, background slip area, and combined strong motion generation area and background slip area.

The ground motions from the strong motion generation area were almost identical to those from the characterized source model, both in acceleration and velocity (Fig. 8). In contrast, the acceleration and velocity contributions from the background slip area were small, although that of the displacement was slightly more significant.

This suggests that near-source strong ground motions are mainly controlled by the size of the strong motion generation area and its risetime.

Our characterized source model was constructed from the viewpoint of slip-velocity, and the target frequency was 0.2–10 Hz. Miyakoshi *et al.* (2000) characterized their heterogeneous source model from the viewpoint of the slip itself, and used a target frequency of 0.1–0.5 Hz. We showed that the characterized source model of slip in the low-frequency range was equivalent to the characterized source model of slip-velocity in the broadband frequency range.

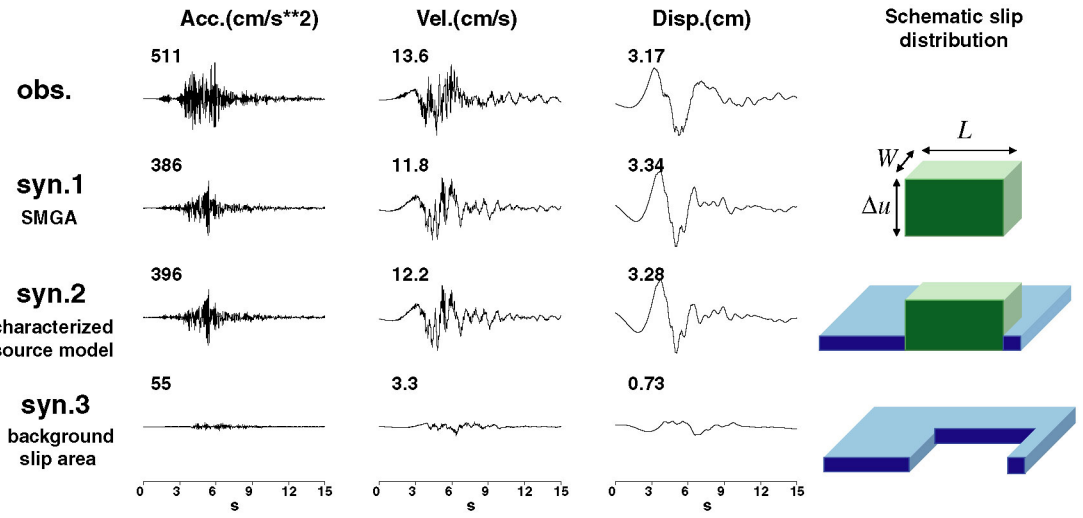

Figure 8. Comparison of the observed and synthetic EW component waveforms (0.2–10 Hz) at station KGS002 for the March 1997 Kagoshima-ken Hokuseibu earthquake. From top to bottom: The traces show the observed waveforms and synthetic waveforms from the strong motion generation area, of the combination of the strong motion generation area and background slip area in our characterized source model, and the background slip area. From left to right: Acceleration, velocity, and displacement waveforms. The numbers above the waveforms are the maximum amplitude values (after Miyake *et al*., 2003).

Conclusions

We estimated the strong motion generation area using the empirical Green's function method, and then confirmed that the strong motion generation areas coincided with the areas of the asperities of the heterogeneous slip distributions derived from low-frequency (< 1 Hz) waveform inversions. The self-similar scalings for the size of the strong motion generation area and risetime, as functions of the seismic moment, were found for the range of earthquakes smaller than M_w 6.0. These scalings were compatible with those for larger earthquakes obtained by Somerville *et al*. (1999).

Source characterization for simulating broadband frequency ground motion

requires strong motion generation areas that produce high-frequency motions with large slip velocities, as well as a background slip area that produces low-frequency motions with a small slip velocity. The near-source strong ground motions are controlled mainly by the size of the strong motion generation area and risetime there. The characterized source model looks different from the high-frequency source models from envelope inversions. However, we addressed the fact that strong motion generation areas with a stress drop of 10 MPa can also reproduce a series of high-frequency motions.

A strong motion generation area contains both low- and high-frequency information, scaled to the wave generations and rupture dynamics of a small earthquake. We verified that quantified strong motion generation areas and the concept of characterized source modeling are sufficiently capable of performing broadband ground motion simulations for acceleration, velocity, and displacement.

References

Aki, K. (1967). Scaling law of seismic spectrum, *J. Geophys. Res.,* **72**, 1217-1231.

Beroza, G. C. (1991). Near-source modeling of the Loma Prieta earthquake: evidence for heterogeneous slip and implications for earthquake hazard, *Bull. Seismol. Soc. Am*., **81**, 1603-1621.

Bouchon, M., M. N. Toksöz, H. Karabulut, and M. -P. Bouin (2002). Space and time evolution of rupture and faulting during the 1999 İzmit (Turkey) earthquake, *Bull. Seismol. Soc. Am*., **92**, 256-266.

Boatwright, J. (1988). The seismic radiation from composite models of faulting, *Bull. Seismol. Soc. Am*., **78**, 489-508.

Brune, J. N. (1970). Tectonic stress and the spectra of seismic shear waves from earthquakes, *J. Geophys. Res*., **75**, 4997-5009.

Brune, J. N. (1971). Correction, *J. Geophys. Res*., **76**, 5002.

Chi, W. C., D. Dreger, and A. Kaverina (2001). Finite-source modeling of the 1999 Taiwan (Chi-Chi) earthquake derived from a dense strong-motion network *Bull. Seismol. Soc. Am*., **91**, 1144-1157.

Cohee, B. P. and G. C. Beroza (1994). Slip distribution of the 1992 Landers earthquake and its implications for earthquake source mechanics, *Bull. Seismol. Soc. Am*., **84**, 692-172.

Cotton, F. and M. Campillo (1995). Frequency domain inversion of strong motions: Application to the 1992 Landers earthquake, *J. Geophys. Res*., **100**, 3961-3975.

Das, S. and B. V. Kostrov (1986). Fracture of a single asperity on a finite fault: A model for weak earthquakes?, in *Earthquake Source Mechanics* (Geophysical Monograph

Series Volume 37), S. Das, J. Boatwright, and C. H. Scholz (editors), American Geophysical Union, Washington, D.C., 91-96.

Delouis, B., D. Giardini, P. Lundgren, and J. Salichon *et al*. (2002). Joint inversion of InSAR, GPS, teleseismic, and strong-motion data for the spatial and temporal distribution of earthquake slip: Application to the 1999 İzmit mainshock, *Bull. Seismol. Soc. Am*., **92**, 278-299.

Dziewonski, A. M., G. Ekstrom, and M. P. Salganik (1996). Centroid-moment tensor solutions for January-March 1995, *Phys. Earth Planet. Interiors,* **93**, 147-157.

Dziewonski, A. M., G. Ekstrom, N. N. Maternovskaya, and M. P. Salganik (1997). Centroid-moment tensor solutions for July-September, 1996, *Phys. Earth Planet. Interiors,* **102**, 133-143.

Faculty of Science, Kagoshima University (1997). The earthquakes with M6.3 (March 26, 1997) and with M6.2 (May 13, 1997) occurred in northwestern Kagoshima prefecture, *Rep. Coord. Comm. Earthq. Pred*., **58**, 630-637 (in Japanese).

Faculty of Science, Kyushu University (1997). Seismic activity in Kyushu (November 1996-April 1997), *Rep. Coord. Comm. Earthq. Pred*, **58**, 605-618 (in Japanese).

Fukuoka District Meteorological Observatory, JMA (1998). On an M6.3 earthquake in the northern Yamaguchi prefecture on June 25, 1997, *Rep. Coord. Comm. Earthq. Pred*, **59**, 507-510 (in Japanese).

Fukuyama, E., M. Ishida, S. Horiuchi, H. Inoue, S. Hori, S. Sekiguchi, H. Kawai, H. Murakami, S. Yamamoto, K. Nonomura, and A. Goto (2000a). NIED seismic moment tensor catalogue January-December, 1999, *Technical Note of the National Research Institute for Earth Science and Disaster Prevention*, **199**, 1-56.

Fukuyama, E., M. Ishida, S. Horiuchi, H. Inoue, S. Hori, S. Sekiguchi, A. Kubo, H. Kawai, H. Murakami, and K. Nonomura (2000b). NIED seismic moment tensor catalogue January-December, 1997, *Technical Note of the National Research Institute for Earth Science and Disaster Prevention*, **205**, 1-35.

Fukuyama, E., M. Ishida, S. Horiuchi, H. Inoue, A. Kubo, H. Kawai, H. Murakami, and K. Nonomura (2001). NIED seismic moment tensor catalogue January-December, 1998 (revised), *Technical Note of the National Research Institute for Earth Science and Disaster Prevention*, **218**, 1-51.

Graduate School of Science, Tohoku University (1999). On the seismic activity of the M6.1 earthquake of 3 September 1998 in Shizukuishi, Iwate prefecture, *Rep. Coord. Comm. Earthq. Pred*, **60**, 49-53 (in Japanese).

Hartzell, S. H. (1978). Earthquake aftershocks as Green's functions, *Geophys. Res. Lett.*, **5**, 1- 4.

Harzell, S. H. and T. H. Heaton (1983). Inversion of strong ground motion and teleseismic waveform data for the fault rupture history of the 1979 Imperial Valley, California, earthquake, *Bull. Seismol. Soc.. Am.*, **73**, 1553-1583.

Holland, J. H. (1975). *Adaptation in natural and artificial systems*, The University of Michigan Press, Ann Arbor.

Horikawa, H., K. Hirahara, Y. Umeda, M. Hashimoto, and F. Kusano (1996). Simultaneous inversion of geodetic and strong motion data for the source process of the Hyogo-ken Nanbu, Japan, earthquake, *J. Phys. Earth*, **44**, 455-471.

Horikawa. H. (2001). Earthquake doublet in Kagoshima, Japan: Rupture of asperities in a stress shadow, *Bull. Seismol. Soc. Am*., **91**, 112-127.

Hurukawa, N. (1981). Normal faulting microearthquakes occurring near the Moho discontinuity in the northeastern Kinki district, Japan, *J. Phys. Earth*, **29**, 519-535.

Ide, S., M. Takeo, and Y. Yoshida (1996). Source process of the 1995 Kobe earthquake: determination of spatio-temporal slip distribution by Bayesian modeling, *Bull. Seismol. Soc. Am*., **86**, 547-566.

Ide, S. (1999). Source process of the 1997 Yamaguchi, Japan, earthquake analyzed in different frequency bands, *Geophys. Res. Lett.*, **26**, 1973-1976.

Irikura, K., Semi-empirical estimation of strong ground motions during large earthquakes, *Bull. Disast. Prev. Res. Inst., Kyoto Univ., 33*, 63-104, 1983.

Irikura, K. (1983). Semi-empirical estimation of strong ground motions during large earthquakes, *Bull. Disast. Prev. Res. Inst., Kyoto Univ.*, **33**, 63-104.

Irikura, K. (1986). Prediction of strong acceleration motions using empirical Green's function, *Proc. 7th Japan Earthq. Eng. Symp*., 151-156.

Irikura, K. and K. Kamae (1994). Estimation of strong ground motion in broad-frequency band based on a seismic source scaling model and an empirical Green's function technique, *Annali di Geofisica,* **37**, 1721-1743.

Irikura, K., T. Kagawa, and H. Sekiguchi (1997). Revision of the empirical Green's function method by Irikura (1986), *Programme and abstracts, Seism. Soc. Japan,* **2**, B25 (in Japanese).

Kakehi, Y. and K. Irikura (1996). Estimation of high-frequency wave radiation areas on the fault plane by the envelope inversion of acceleration seismograms, *Geophys. J. Int*., **125**, 892-900.

Kakuta, T., H. Miyamachi, and A. Takagi (1991). Intermediate earthquakes in a northern part of the Kyushu-Ryukyu arc, *Zisin*, **44**, 63-74 (in Japanese with English abstract).

Kamae, K. and K. Irikura (1998a). Source model of the 1995 Hyogo-ken Nanbu earthquake and simulation of near-source ground motion, *Bull. Seismol. Soc. Am*., **88**,

400-412.

Kamae, K. and K. Irikura (1998b). A source model of the 1994 Northridge earthquake (M_w=6.7), *Proc. 10th Japan Earthq. Eng. Symp*., 643-648 (in Japanese with English abstract).

Kanamori, H. (1977). The energy release in great earthquakes, *J. Geophys. Res.,* **82**, 2981-2987.

Kanamori, H. (1979). A semi-empirical approach to prediction of long-period ground motions from great earthquakes*, Bull. Seismol. Soc. Am*., **69**, 1645-1670.

Kanamori, H. and D. L. Anderson (1975). Theoretical basis of some empirical relations in seismology, *Bull. Seismol. Soc. Am*., **65**, 1073-1095.

Kawase, H. (1998). Metamorphosis of near-field strong motions by underground structures and their destructiveness to man-made structures – Learned from the damage belt formation during the Hyogo-ken Nanbu earthquake of 1995 –, *Proc. 10th Japan Earthq. Eng. Symp*., 29-34 (in Japanese with English abstract).

Kinoshita, S. (1998). Kyoshin Net (K-NET), *Seismol. Res. Lett.,* **69**, 309-332.

Kuge, K. (2003). Source modeling using strong-motion waveforms: Toward automated determination of earthquake fault planes and moment-release distributions, *Bull. Seismol. Soc. Am*., **93**, 639-654.

Kuge, K., T. Iwata, and K. Irikura (1997). Automatic estimation of earthquake source parameters using waveform data from the K-NET, *Programme and abstracts, Seism. Soc. Japan*, **2**, B16 (in Japanese).

Ma, K. F., J. Mori, S. J. Lee, and S. B. Yu (2001). Spatial and temporal distribution of slip for the 1999 Chi-Chi, Taiwan, earthquake, *Bull. Seismol. Soc. Am*., **91**, 1069-1087.

Madariaga, R., (1979). On the relation between seismic moment and stress drop in the presence of stress and strength heterogeneity, *J. Geophys. Res*., **84**, 2243-2250.

Mai, P. M. and G. C. Beroza (2000). Source scaling properties from finite-fault rupture models, *Bull. Seismol. Soc. Am*., **90**, 604-615.

Mai, P. M. and G. C. Beroza (2002). A Spatial random-field model to characterize complexity in earthquake slip, *J. Geophys. Res*., **107**, 10.1029/2001JB000588.

Miyake, H., T. Iwata, and K. Irikura (1999). Strong ground motion simulation and source modeling of the Kagoshima-ken Hokuseibu earthquakes of march 26 (M_{JMA}6.5) and May 13 (M_{JMA}6.3), 1997, using empirical Green's function method, *Zisin*, **51**, 431-442 (in Japanese with English abstract).

Miyake, H., T. Iwata, and K. Irikura (2001). Estimation of rupture propagation direction and strong motion generation area from azimuth and distance dependence of source

amplitude spectra, *Geophys. Res. Lett.*, **28**, 2727-2730.

Miyake H, T. Iwata, and K. Irikura (2003). Source characterization for broadband ground motion simulation: Kinematic heterogeneous source model and strong motion generation area, *Bull. Seismol. Soc. Am.*, **93**, 2531-2545.

Miyakoshi, K., T. Kagawa, H. Sekiguchi, T. Iwata, and K. Irikura (2000). Source characterization of inland earthquakes in Japan using source inversion results, *Proc. 12th World Conf. Earthq. Eng.* (CD-ROM).

Miyamachi, H., K. Iwakiri, H. Yakiwara, K. Goto, and T. Kakuta (1999). Fine structure of aftershock distribution of the 1997 Northwestern Kagoshima earthquakes with a three-dimensional velocity model, *Earth Planet Space,* **51**, 233-246.

Nakahara, H., T. Nishimura, H. Sato, and M. Ohtake (1998). Seismogram envelope inversion for the spatial distribution of high-frequency energy radiation from the earthquake fault: Application to the 1994 far east off Sanriku earthquake, Japan, *J. Geophys. Res.,* **103**, 855-867.

Nakahara, H., T. Nishimura, H. Sato, M. Ohtake, S. Kinoshita, and H. Hamaguchi (2002). Broad-band source process of the 1998 Iwate Prefecture, Japan, earthquake as revealed from inversion analyses of seismic waveforms and envelopes, *Bull. Seismol. Soc. Am.*, **92**, 1708-1720.

Nakamura, H. and T. Miyatake (2000). An approximate expression of slip velocity time function for simulation of near-field strong ground motion, *Zisin*, **53**, 1-9 (in Japanese with English abstract).

Ogue, Y., Y. Wada, A. Narita, and S. Kinoshita (1997). Deconvolution for the K-NET data from earthquake in southern Kyushu, *Programme and abstracts, Seism. Soc. Japan*, **2**, B23 (in Japanese).

Okada, T., N. Umino, A. Hasegawa, and N. Nishide (1997). Source processes of the earthquakes in the border of Akita and Miyagi prefectures in August, 1996 (2), *Programme and abstracts, Seism. Soc. Japan*, **2**, B69 (in Japanese).

Okada, T., N. Umino, Y. Ito, T. Matsuzawa, A. Hasegawa, and M. Kamiyama (2001). Source processes of 15 September 1998 *M* 5.0 Sendai, northeastern Japan, earthquake and its *M* 3.8 foreshock by waveform inversion, *Bull. Seismol. Soc. Am.*, **91**, 1607-1618.

Satoh, T., H. Kawase, and S. Matsushima (1998). Source spectra, attenuation function, and site amplification factors estimated from the K-NET records for the earthquakes in the border of Akita and Miyagi prefectures in August, 1996, *Zisin*, **50**, 415-429 (in Japanese with English abstract).

Sekiguchi, H., K. Irikura, T. Iwata, Y. Kakehi, and M. Hoshiba (1996). Minute locating

of faulting beneath Kobe and the waveform inversion of the source process during the 1995 Hyogo-ken Nanbu, Japan, earthquake using strong ground motion records, *J. Phys. Earth*, **44**, 473-487.

Sekiguchi, H., K. Irikura, and T. Iwata (2000). Fault geometry at the rupture termination of the 1995 Hyogo-ken Nanbu Earthquake, *Bull. Seismol. Soc. Am*., **90**, 117-133.

Sekiguchi, H. and T. Iwata (2002). Rupture process of the 1999 Kocaeli, Turkey, earthquake estimated from strong-motion waveforms, *Bull. Seismol. Soc. Am*., **92**, 300-311.

Somerville, P., K. Irikura, R. Graves, S. Sawada, D. Wald, N. Abrahamson, Y. Iwasaki, T. Kagawa, N. Smith, and A. Kowada (1999). Characterizing crustal earthquake slip models for the prediction of strong ground motion, *Seismol. Res. Lett.,* **70**, 59-80.

Umino, N., T. Matsuzawa, S. Hori, A. Nakamura, A. Yamamoto, A. Hasegawa, and T. Yoshida (1998). 1996 Onikobe earthquakes and their relation to crustal structure, *Zisin*, **51**, 253-264 (in Japanese with English abstract).

Wald, D. J., D. V. Helmberger, and T. H. Heaton (1991). Rupture model of the 1989 Loma Prieta earthquake from the inversion of strong motion and broadband teleseismic data, *Bull. Seismol. Soc.. A*m**.**, **81**, 1540-1572.

Wald, D. J. and T. H. Heaton (1994). Spatial and temporal distribution of slip of the 1992 Landers, California earthquake, *Bull. Seismol. Soc. A*m**.**, **84**, 668-691.

Wald, D. J. (1996). Slip history of the 1995 Kobe, Japan, earthquake determined from strong motion, teleseismic, and geodetic data, *J. Phys. Earth*, **44**, 489-503.

Wald, D. J., T. H. Heaton, and K. W. Hudnut (1996). The slip history of the 1994 Northridge, California, earthquake determined from strong-motion, teleseismic, GPS, and leveling data, *Bull. Seismol. Soc. A*m**.**, **86**, S49-S70.

Wessel, P. and W. H. F. Smith (1995). New version of the Generic Mapping Tools released, *EOS Trans. Am. Geophys. Union.,* **76**, 329.

Wu. C., M. Takeo, and S. Ide (2001). Source process of the Chi-Chi earthquake: A joint inversion of strong motion data and global positioning system data with a multifault model, *Bull. Seismol.. Soc. Am*., **91**, 1028-1043.

Yoshida, S., K. Koketsu, B. Shibazaki, T. Sagiya, T. Kato, and Y. Yoshida (1996). Joint inversion of near- and far-field waveforms and geodetic data for the rupture process of the 1995 Kobe earthquake, *J. Phys. Earth*, **44**, 437-454.

Zeng, Y., K. Aki, and T. Teng (1993). Mapping of the high-frequency source radiation for the Loma Prieta earthquake, California, *J. Geophys. Res.,* **98**, 11981-11993.

Zeng, Y. and C. H. Chen (2001) Fault rupture process of the 20 September 1999 Chi-Chi, Taiwan, earthquake, *Bull. Seismol. Soc. Am*., **91**, 1088-1098.

Note: A program of the empirical Green's function method by Irikura (1986) will be provided upon request.

Chapter 3. Theoretical Simulation of Long-Period Ground Motion using Three-Dimensional Finite Difference Method (3D FDM)

Summary

Long-period ground motions were simulated using the fourth order finite difference method with the variable spacing staggered-grid of Pitarka (1999) and a frequency-dependent attenuation factor (Graves, 1996). The calculations were performed in the frequency range of 0.05–0.4 Hz. Basin models for the Osaka basin were constructed using geophysical and geological data, such as borehole, seismic reflection survey, microtremor, and gravity anomaly data. The Q value of the sedimentary layers in the Osaka Basin for long period ground motion were estimated by comparing the synthetic motions, including later phases, with the observed ones. The optimum Q value was found to be S-wave dependent, as represented by $Q = f \cdot V_s/2$. Furthermore, we simulated the long period ground motions in the Osaka basin from great subduction-zone earthquakes occurring along the Nankai Trough. This chapter was partly based on Kawabe and Kamae (2008).

Introduction

Osaka and Nagoya, representative mega cities of Japan, have repeatedly suffered from earthquake disasters caused by great subduction-zone earthquakes with magnitudes greater than eight occurring along the Nankai Trough. The 30-year probabilities were estimated as 48% and 61% for Nankai and Tonankai earthquakes, respectively, showing the very high possibility that an earthquake will occur. Osaka and Nagoya are located in a basin with thick sediments (about 1 to 3 km), causing long-period motions to be strongly enhanced during subduction-zone earthquakes.

There are numerous long period and low damping structures (such as tall buildings and oil tanks) inside the Osaka basin. For earthquake disaster mitigation, it is very important to predict the amplitude and duration of the long period strong ground motions from future Tonankai and Nankai earthquakes. A highly accurate three-dimensional (3-D) velocity model and the attenuation factor for this sedimentary basin are required to increase the prediction precision for long period ground motions.

Various 3-D subsurface structural models of the Osaka sedimentary basin have been developed over the last few years (Kagawa *et al*., 1993; Miyakoshi *et al.*, 1999; Horikawa *et al*., 2003). These models have been constructed using geophysical and geological data, such as the borehole, seismic reflection survey, microtremor, and gravity anomaly data. However, these models cannot accurately reproduce the seismic waveforms because of a lack of sufficient investigation of the attenuation factor (Q value) and modeling using observed records. In this study, we focused on the Osaka basin, using simulations of the observed seismic waveforms to optimize the Q value of the sedimentary layers, which primarily control the amplitude of the *S*-wave. First, we constructed a 3-D velocity model of the Osaka basin by referring to some data sets. Next, we searched for the optimum Q value of the sedimentary layers from the fittings between the synthetic *S*-wave amplitudes and those observed for several actual earthquakes. Finally, we simulated the long period ground motions in the Osaka basin from a great subduction zone earthquake occurring along the Nankai trough.

Numerical Method

The following sets of equations describe wave propagation within 3-D, linear, isotropic elastic media.

Conservation of momentum equations:

$$\rho\partial_{tt}u_x = \partial_x\tau_{xx} + \partial_y\tau_{xy} + \partial_z\tau_{xz} + f_x\,,$$

$$\rho\partial_{tt}u_y = \partial_x\tau_{xy} + \partial_y\tau_{yy} + \partial_z\tau_{yz} + f_y\,, \qquad (1)$$

$$\rho\partial_{tt}u_z = \partial_x\tau_{xz} + \partial_y\tau_{yz} + \partial_z\tau_{zz} + f_z\,.$$

Stress-strain relations:

$$\tau_{xx} = (\lambda + 2\mu)\partial_x u_x + \lambda(\partial_y u_y + \partial_z u_z)\,,$$

$$\tau_{yy} = (\lambda + 2\mu)\partial_y u_y + \lambda(\partial_x u_x + \partial_z u_z)\,,$$

$$\tau_{zz} = (\lambda + 2\mu)\partial_z u_z + \lambda(\partial_x u_x + \partial_y u_y)\,, \qquad (2)$$

$$\tau_{xy} = \mu(\partial_y u_x + \partial_x u_y)\,,$$

$$\tau_{xz} = \mu(\partial_z u_x + \partial_x u_z)\,,$$

$$\tau_{yz} = \mu(\partial_z u_y + \partial_y u_z)\,.$$

In these equations, (u_x, u_y, u_z) are the displacement components, (τ_{xx}, τ_{yy}, τ_{zz}, τ_{xy}, τ_{yz}, τ_{xz}) are the stress components, (f_x, f_y, f_z) are the body force components, ρ is the density, λ and μ are Lamé coefficients, and the symbols ∂_x, ∂_y, ∂_z, and ∂_{tt} are shorthand representations of the differential operators $\partial/\partial x$, $\partial/\partial x$, $\partial/\partial x$, and $\partial^2/\partial t^2$.

In the 3-D calculations, we used the fourth-order staggered-grid 3-D finite difference method with variable grid spacing (Pitarka, 1999). Fig. 1 illustrates the layout of the wave-field variables and media parameters on a staggered-grid mesh. By using second-order approximation for the time derivatives, the discrete forms of equations (1) and (2) are given by

$$
\begin{aligned}
v_{x\,i+1/2,j,k}^{\,n+1/2} &= v_{x\,i+1/2,j,k}^{\,n-1/2} + \Delta t b_x (D_x \tau_{xx} \\
&\quad + D_y \tau_{xy} + D_z \tau_{xz} + f_x)\,|^n_{i+1/2,j,k} \\
v_{y\,i,j+1/2,k}^{\,n+1/2} &= v_{y\,i,j+1/2,k}^{\,n-1/2} + \Delta t b_y (D_x \tau_{xy} \\
&\quad + D_y \tau_{yy} + D_z \tau_{yz} + f_y)\,|^n_{i,j+1/2,k} \\
v_{z\,i,j,k+1/2}^{\,n+1/2} &= v_{z\,i,j,k+1/2}^{\,n-1/2} + \Delta t b_z (D_x \tau_{xz} \\
&\quad + D_y \tau_{yz} + D_z \tau_{zz} + f_z)\,|^n_{i,j,k+1/2}
\end{aligned}
\tag{3}
$$

for the velocities, and

$$
\begin{aligned}
\tau_{xx\,i,j,k}^{\,n+1} &= \tau_{xx\,i,j,k}^{\,n} + \Delta t[(\lambda + 2\mu) D_x v_x \\
&\quad + \lambda (D_y v_y + D_z v_z)]\,|^{n+1/2}_{i,j,k} \\
\tau_{yy\,i,j,k}^{\,n+1} &= \tau_{yy\,i,j,k}^{\,n} + \Delta t[(\lambda + 2\mu) D_y v_y \\
&\quad + \lambda (D_x v_x + D_z v_z)]\,|^{n+1/2}_{i,j,k} \\
\tau_{zz\,i,j,k}^{\,n+1} &= \tau_{zz\,i,j,k}^{\,n} + \Delta t[(\lambda + 2\mu) D_z v_z \\
&\quad + \lambda (D_x v_x + D_y v_y)]\,|^{n+1/2}_{i,j,k} \\
\tau_{xy\,i+1/2,j+1/2,k}^{\,n+1} &= \tau_{xy\,i+1/2,j+1/2,k}^{\,n} + \Delta t[\mu_{xy} (D_y v_x \\
&\quad + D_x v_y)]\,|^{n+1/2}_{i+1/2,j+1/2,k}
\end{aligned}
\tag{4}
$$

$$\tau_{xz\,i+1/2,j,k+1/2}^{\,n+1} = \tau_{xz\,i+1/2,j,k+1/2}^{\,n} + \Delta t[\mu_{xz}(D_z v_x + D_x v_z)]\big|_{i+1/2,j,k+1/2}^{n+1/2}$$

$$\tau_{yz\,i,j+1/2,k+1/2}^{\,n+1} = \tau_{yz\,i,j+1/2,k+1/2}^{\,n} + \Delta t[\mu_{yz}(D_z v_y + D_y v_z)]\big|_{i,j+1/2,k+1/2}^{n+1/2}$$

for the stress. In these equations, the superscripts refer to the time index and the subscripts refer to the spatial indices. Δt is the time step and D_x, D_y, and D_z represent the central finite difference operators of the spatial derivatives ∂_x, ∂_y, and ∂_z, respectively.

The finite difference operators D_x, D_y, and D_z in the computation are implemented on a mesh with nonuniform grid spacing developed by Pitarka (1999). We use the effective parameters for the buoyancy b and rigidity μ suggested by Graves (1996). This technique can significantly reduce the necessary computer memory while efficiently calculating the ground motions at realistic 3-D structures. It handles shorter wavelengths and larger areas than conventional methods, as indicated by Pitarka (1999).

We set an absorbing region outside the finite computational region, and applied the non-reflecting boundary condition of Cerjan *et al*. (1985) and the A1 absorbing boundary condition of Clayton and Engquist (1977) to this region. The implementation of the attenuation in the finite difference method was based on the Graves (1996) technique, which considers Q to be the same for both *P*- and *S*-waves, and frequency dependent. Q has the linear form

$$Q(f) = Q_0\,(f/f_0), \qquad (5)$$

where Q_0 is the frequency-independent factor, f is the frequency, and f_0 is the reference frequency. In this study, the reference frequency was set at 1 Hz. Here, we assumed that the anelastic attenuation factor Q_0 was proportional to the *S*-wave velocity, and given by

$$Q_0 = \alpha_0\, V_s, \qquad (6)$$

where α_0 is the proportionality factor (s/m) and V_s is the *S*-wave velocity (m/s).

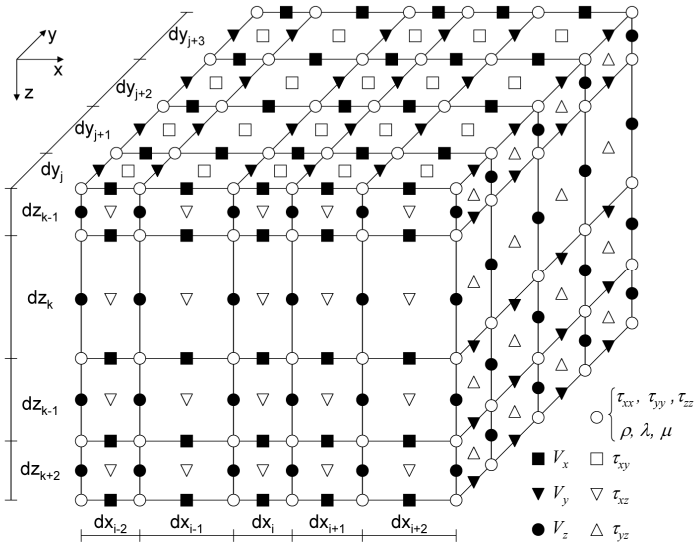

Figure 1. Grid layout for staggered-grid formulation.

3-D Velocity Model and Verification

We tried to produce a 3-D velocity model of the Osaka basin and estimate the optimum attenuation factors for long period ground motion simulation from a comparison between the synthetic and observed waveforms. Our velocity model was constructed based on three data sets: (1) the background 3-D crustal structure model, (2) the sedimentary-layer model of the Osaka basin by Miyakoshi *et al*. (1999) and Horikawa *et al*. (2003), and (3) the boundary between the oceanic and land plates based on the Philippine Sea plate boundary model (Hori *et al*., 2004). The area of our model, the epicenter of one event (Table 1), and the ground-motion-recording stations used in this study are shown in Fig. 2. The 3-D bedrock topography of the corresponding area is shown in Fig. 3.

We simulated the long-period ground motions of the M_w 5.5 Mieken–Nanbu earthquake of 2000 (Table 1) using six different values for Q (α_0=1/10, 1/5, 1/2, 1/1, infinity). Fig. 4 shows an example of a comparison between the synthetic waveforms and those observed at the ABN station. Both the synthetic and recorded waveforms were bandpass filtered at 0.05–0.4 Hz. This figure shows that our 3-D velocity model can reproduce the direct *S*-wave amplitude and phase characteristics of the observed ground motions. The amplitude of the *S*-wave synthesized using α_0=1/2 was in good agreement with the observed one. Therefore, we can recommend $Q = f \cdot V_s/2$ as the optimum Q for waveform simulations. To investigate the frequency dependence of Q, we compared the synthetic waveforms with the observed ones for three frequency bands. As an example, Fig. 5 shows a comparison of the synthetic waveforms using $Q = f \cdot V_s/2$

with those observed at the ABN station. The amplitudes and phases of the synthesized *S*-waves were in good agreement with those observed for each frequency band. These results indicate that the Graves (1996) technique with $Q = f \cdot V_s/2$ can be used for the actual frequency dependence of the attenuation for the 0.05–0.4 Hz frequency band.

Table 1. Source model of the Mieken–Nanbu earthquake.

Origin Time (JST)	Lon. (°)	Lat. (°)	Depth (km)	Strike (°)	Dip (°)	Rake (°)	Mo (Nm)
2000/10/31, 1:42	136.34	34.30	35.4	295.8	59.8	121.7	1.7×10^{17}

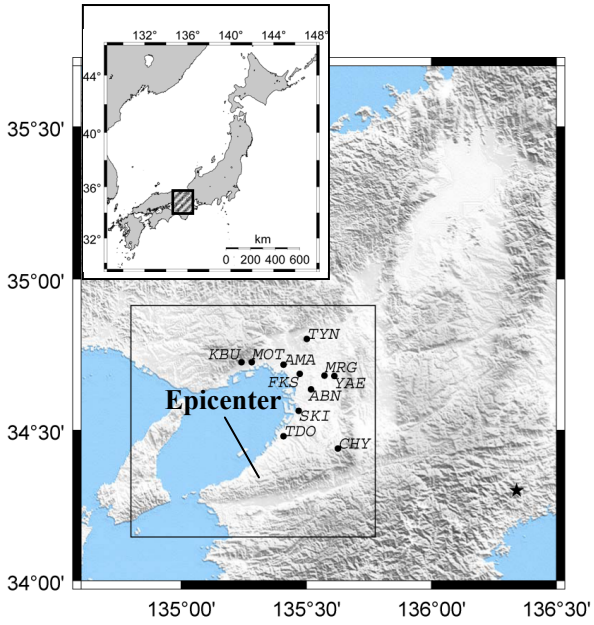

Figure 2. A map showing the locations of the epicenter shown in Table 1, observation stations, and the region of the sedimentary-layer model of the Osaka basin. The solid line indicates the location of the sedimentary layer model of the Osaka basin.

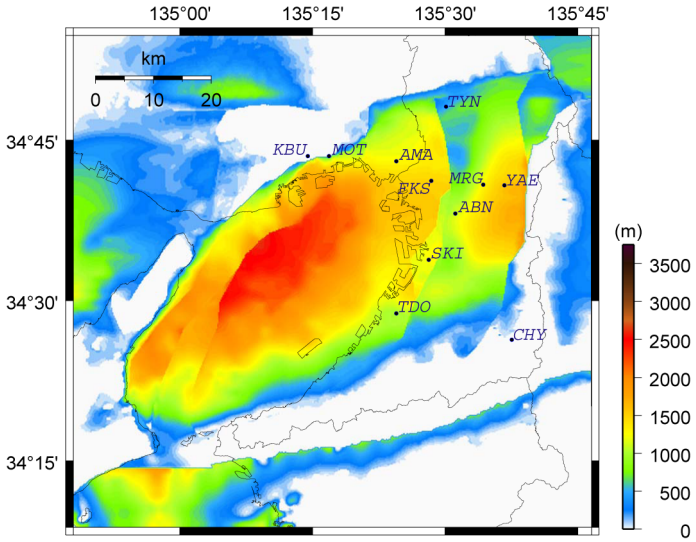

Figure 3. 3-D basement surface depth of the Osaka basin (after Kawabe and Kamae, 2008 base on Horikawa *et al*., 2003).

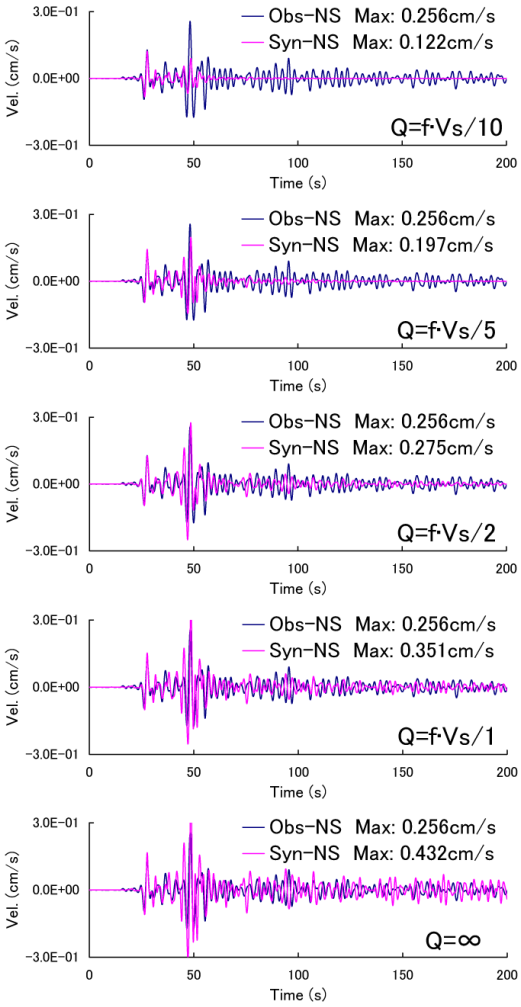

Figure 4. Comparison of the observed waveforms (blue line) with the synthetic ones (pink line) for the Mieken-Nanbu earthquake for five cases of *Q* (Bandpass Filter: 0.05–0.4Hz) (after Kawabe and Kamae, 2008).

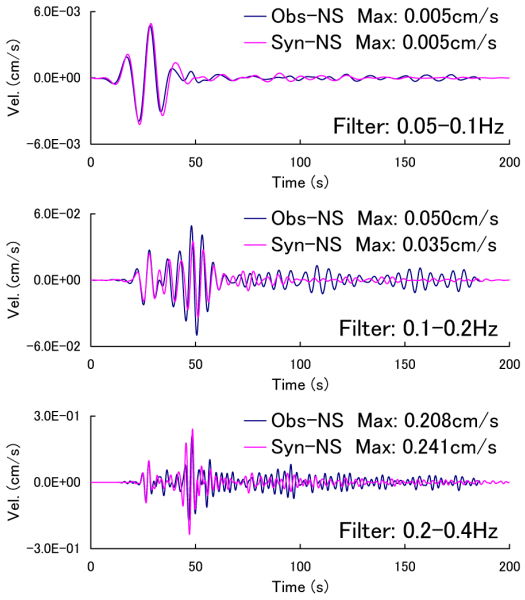

Figure 5. Comparison of the observed waveforms (blue line) with the synthetic ones (pink line) for the Mieken-Nanbu earthquake for three frequency bands ($Q=f \cdot V_s/2$) (after Kawabe and Kamae, 2008).

Prediction of Long Period Ground Motions

We tried to predict the long-period ground motions of future Tonankai and Nankai earthquakes using the 3-D finite difference method. We used the characterized source model proposed by the Earthquake Research Committee (2005). The approach for the source characterization was based on the recipe for estimating strong ground motions from scenario earthquakes by Irikura *et al*. (2004). The location of the source region and the region for the 3D-FD simulation of the Tonankai and Nankai earthquakes are shown in Fig. 6.

Figs. 7 and 8 illustrate the maximum velocity distributions in the Osaka basin for Tonankai and Nankai earthquakes, respectively. The strong ground motion areas (the red areas in Fig. 7) simulated for a Tonankai earthquake are different from those (Fig. 8) for a Nankai earthquake. This is because the ground motion responses vary with the incidental azimuth of the seismic waves in the basins.

Fig. 9 shows the distributions of the pseudo velocity response spectral amplitudes of the predicted ground motions for a Nankai earthquake in the Osaka basin. Figs. 10 and 11 illustrate the velocity waveform and pseudo velocity response spectra at the FKS station shown in Fig. 3. Long period ground motions with periods of 4 to 6 seconds are mainly predominant in the Osaka basin. The characteristics of the long-period ground motions are related to the thicknesses of the sediments in the basins. The long period ground motions inside the basins have durations of more than 4 minutes.

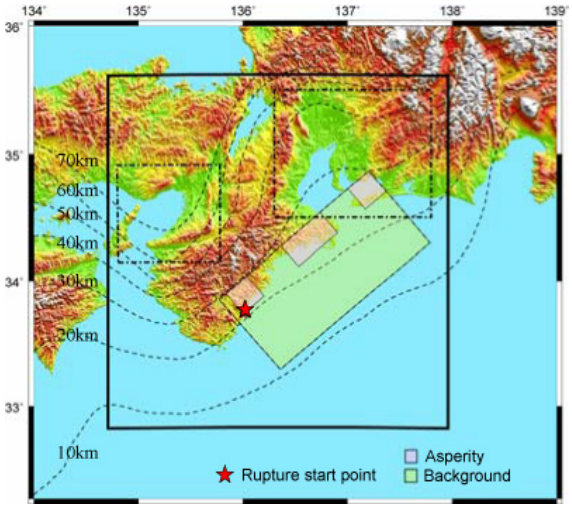

(a) The region for the 3D-FD simulation of a Tonankai earthquake.

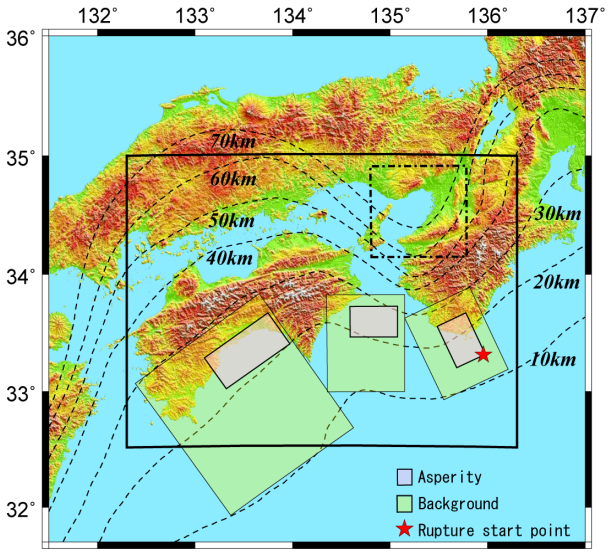

(b) The region for the 3D-FD simulation of a Nankai earthquake.

Figure 6. Maps showing the region of western Japan. The thick rectangular box depicts the region for the 3D-FD simulation of the Nankai and Tonankai earthquakes. The broken lines indicate the area of the velocity structure model of the Osaka basin and the Nobi basin. The contours show the isodepth lines of the Philippine Sea plate boundary (after Kawabe and Kamae, 2008).

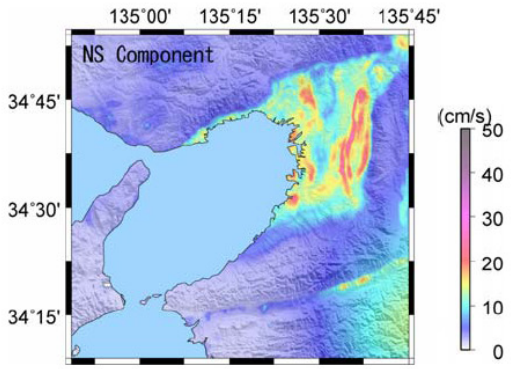

Figure 7. Maximum velocity distribution for the Tonankai earthquake in the Osaka basin (0.05-0.4Hz)

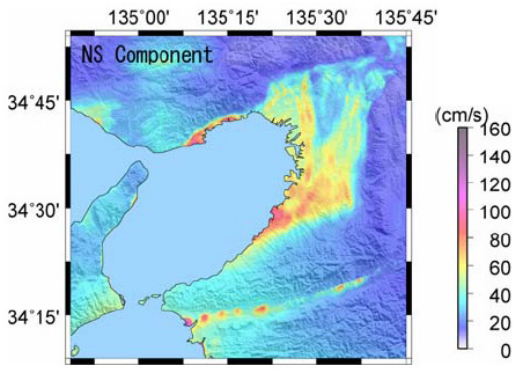

Figure 8. Maximum velocity distribution for the Nankai earthquake in the Osaka basin (0.05-0.4Hz)

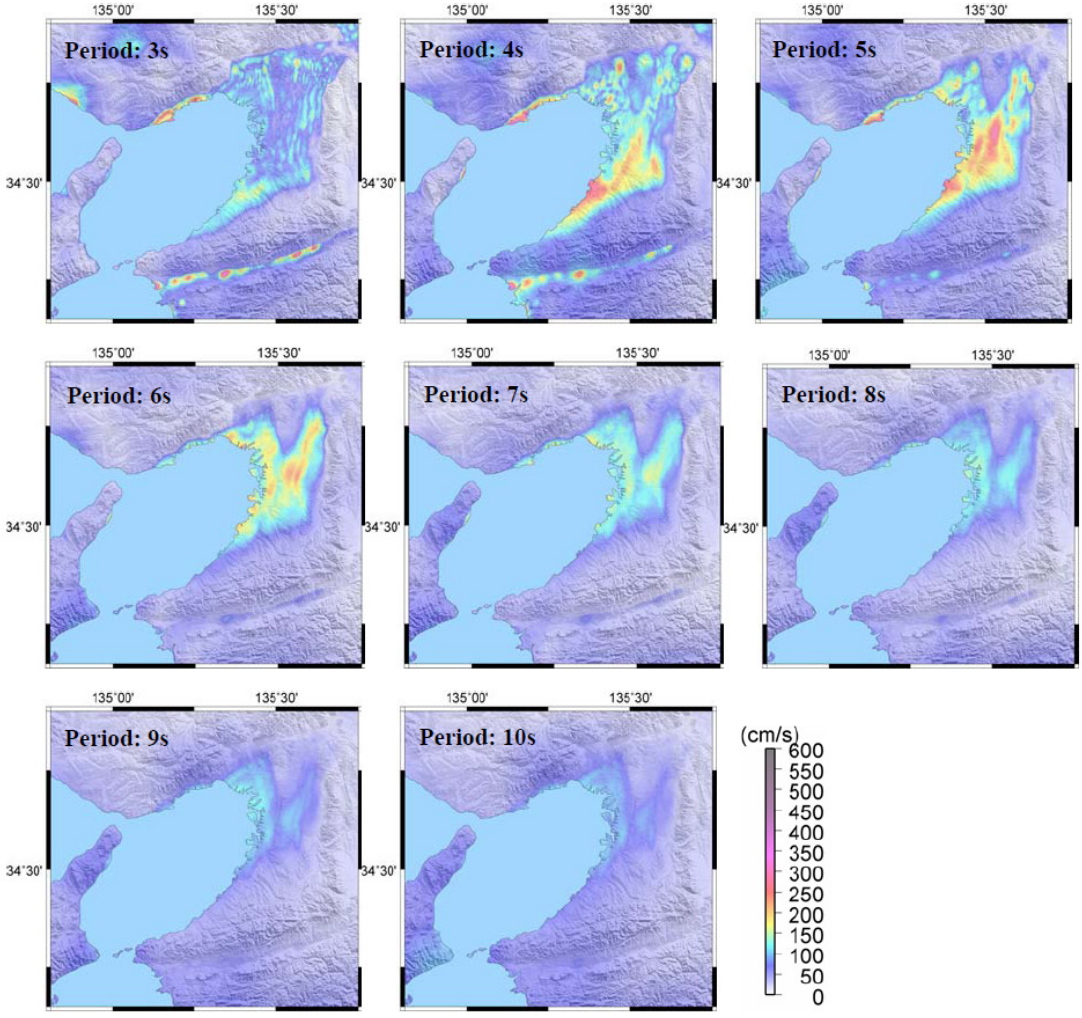

Figure 9. Distributions of pseudo velocity response spectral amplitudes of the predicted ground motions for the Nankai earthquake in Osaka basin. (Damping factor: 5%)

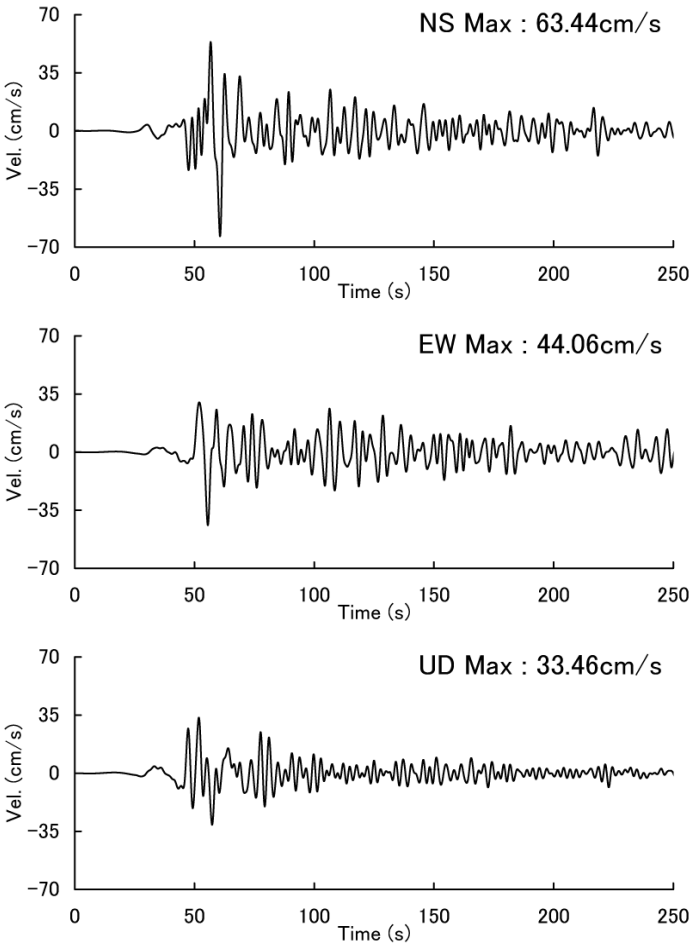

Figure 10. Simulated ground motion at FKS (Bandpass Filter: 0.05-0.4Hz) (after Kawabe and Kamae, 2008).

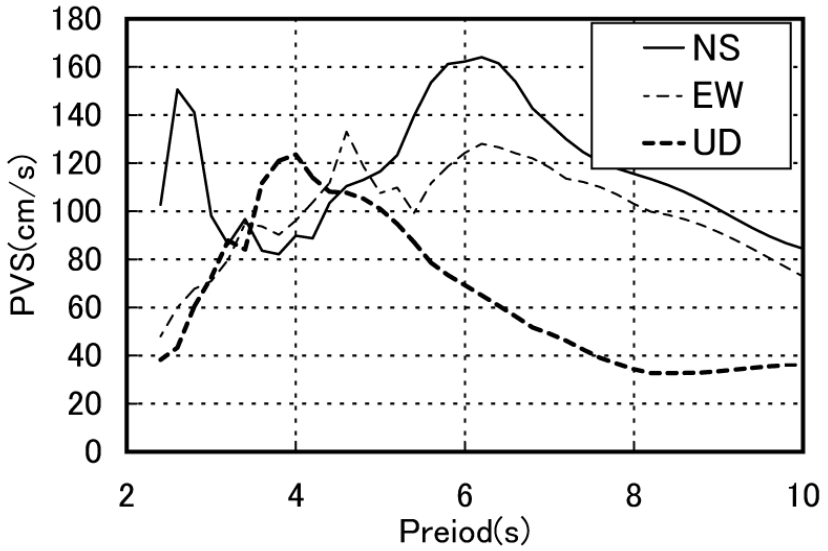

Figure 11. Pseudo velocity response spectra with 5% damping at FKS (after Kawabe and Kamae, 2008).

References

Cerjan, C., D. Kosloff, R. Kosloff, and M. Reshef (1985). A nonreflecting boundary condition for discrete acoustic and elastic wave equations, *Geophysics*, **50**, 705-708.

Clayton, R. and B. Engquist (1977). Absorbing boundary conditions for acoustic and elastic wave equations, *Bull. Seismol. Soc. Am*., **67**, 1529-1540.

Earthquake Research Committee (2005). Seismic Hazard Maps for Specified Seismic Faults, *National Seismic Hazard Map for Japan (2005)*, http://www.jishin.go.jp/main/index-e.html, 59-61.

Graves, R. W. (1996). Simulating seismic wave propagation in 3D elastic media using staggered-grid finite differences, *Bull. Seismol. Soc. Am*., **86**, 1091–1106.

Hori, T., N. Kato, K. Hirahara, T. Baba, and Y. Kaneda (2004). A numerical simulation of earthquake cycles along the Nankai Trough in southwest Japan: lateral variation in frictional property due to the slab geometry controls the nucleation position, *Earth and Plan. Sci. Lett*., **228**, 215-226.

Horikawa, H., K. Mizuno, T. Ishiyama, K. Satake, H. Sekiguchi, Y. Kase, Y. Sugiyama, H. Yokota, M. Suehiro, T. Yokokura, Y. Iwabuchi, N. Kitada, A. Pitarka (2003). A three-dimensional model of the subsurface structure beneath the Osaka sedimentary basin, southwest Japan, with fault-related structural discontinuities, *Annual Report on Active Fault and Paleoearthquake Researches*, Geological Survey of Japan/AIST, 3, 225-259 (in Japanese with English abstract).

Irikura, K, H. Miyake, T. Iwata, K. Kamae, H. Kawabe, and L. A. Dalguer (2004). Recipe for predicting strong ground motions from future large earthquakes, *Proc. 13th World Conference of Earthquake Engineering*, Vancouver, Canada, Paper No.1371.

Kagawa, T., S. Sawada, Y. Iwasaki, and A. Nanjo (1993). Modeling of deep sedimentary structure of the Osaka Basin, *Proc. 22nd JSCE Eqrthq. Eng. Symp.*, 199-202 (in Japanese with English abstract).

Kawabe, H. and K. Kamae (2008). Prediction of long-period ground motions from huge subduction earthquakes in Osaka, Japan, *J. Seismol*., **12**, 173–184.

Miyakoshi, K., T. Kagawa, B. Zhao, T. Tokubayashi and S. Sawada (1999). Modeling of deep sedimentary structure of the Osaka Basin (3), *Proc. 25th JSCE Eqrthq. Eng. Symp*., 185-188 (in Japanese with English abstract).

Pitarka, A. (1999). 3D elastic finite-difference modeling of seismic wave propagation using staggered grid with non-uniform spacing, *Bull. Seismol. Soc. Am*., **89**, 54–68.

Hidenori Kawabe, Katsuhiro Kamae, and Kojiro Irikura

Chapter 4.

Hybrid Method for Simulating Strong Ground Motion

Summary

It has become possible to estimate strong ground motions in the long-period range near the source area of a large earthquake as long as the detailed slip distribution of the source fault and the geological configurations from the source to the site are known. However, strong ground motions in the short-period range are difficult to calculate theoretically because of insufficient information about the source and geological-structures. Hybrid methods for estimating the broadband strong ground motions of interest to engineers have been developed by combining deterministic and stochastic approaches. The long-period motions from the source fault of a large event are deterministically calculated using the 3-D finite-difference method. Short-period ground motions from small events occurring in the source area are stochastically simulated using Boore's method (1983). Short-period ground motions from the large event are estimated by following the empirical Green's function method (Irikura, 1986). Finally, the broadband ground motions from the large event are synthesized by summing the long-period and short-period motions after passing them through a matched pair filter. This chapter was partly based on Kamae and Irikura (1998).

Introduction

It is still difficult to numerically compute the Green's functions at short-periods (< 1 sec), i.e., at the low frequencies (> 1 Hz) that are of interest to engineers. It is necessary to know the detailed geological configuration from the source to the site to compute such short-period motions. Even if it could be done, another problem would be how to compute the ground motions in such a fine meshed 3-D structure, because of the large amount of memory and time required.

If records exist of small events that have occurred in the source area for a future large earthquake, it is possible to simulate the strong ground motions in the broadband range of 0.1 to 10 s, using the empirical Green's function method (1986). However, in most cases, appropriate records from such small events to not exist in sufficient quantities for a ground motion simulation. Therefore, hybrid methods for estimating broadband strong ground motions of interest to engineers have been

developed by combining deterministic and stochastic approaches.

There are two kinds of methods for estimating strong ground motions from large earthquakes. One is the Hybrid Green's Function (HGF) Method proposed by Kamae *et al*. (1998). In this method, the ground motions from small events inside the source area of the target large earthquake are first calculated theoretically for a long-period range by considering a double couple point source in the 3-D structure from the source to the site using a 3-D finite difference method, as well as stochastically in the short-period range using the simulation method of Boore (1983). Then, the hybrid Green's functions are calculated by combining the low and high frequency parts of the ground motions after using a matched pair of filters. Finally, the strong ground motions from a large earthquake in the target source area are obtained by summing the hybrid Green's functions following the empirical Green's functions (Irikura, 1986).

The other type of method used is the Hybrid Synthetic Method proposed by Irikura and Kamae (1999). In this method, the long period motions from a large earthquake are directly simulated with the 3-D finite difference method, taking into account the slip distributions on the source fault. At the same time, the short-period motions from the large event are estimated using the Stochastic Green's Function (SGF) Method (Kamae *et al*., 1991). The procedure is exactly the same as the simulation for the short-period range described above. The broadband ground motions from the large earthquake are obtained by summing the long-period ground motions calculated theoretically and the short-period motions found with the SGF method.

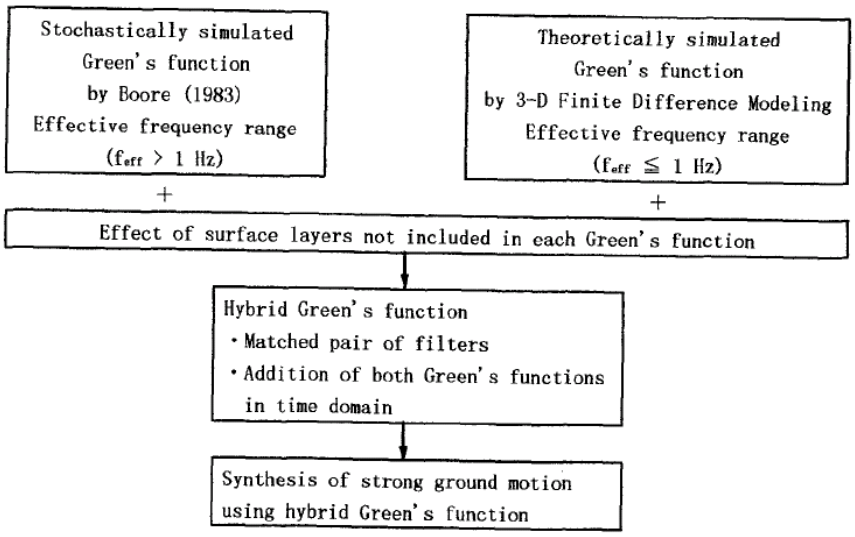

Figure 1. Flow chart for simulating strong ground motions from large earthquakes using the hybrid Green's function (HGF) method (after Kamae *et al*., 1998).

Method and Application

Hybrid Green's function method

A flow chart for the hybrid Green's function method (HGF method, hereafter) is presented in Fig. 1. First, we simulate the high frequency ground motion (f > 1 Hz) from a hypothetical small-event located in the fault plane of the target earthquake using the stochastic simulation technique of Boore (1983), assuming a point source. We introduce a frequency-dependent Q value to his specified acceleration spectrum. We can also take into account additional factors, such as the source mechanism (e.g. a double couple) and frequency-dependent radiation pattern (Pitarka *et al*., 2000). Boore's method is available only for simulating the ground motions from a small-event, not for a large event, because the rupture propagation on the source fault is not taken into account. By using Boore's method, the high frequency part of the simulated Green's function has an acceleration amplitude spectrum that follows the ω-2 model with a high-frequency cutoff (f_{max} = 15 Hz). In the second step we calculate the low frequency part of the Green's function (f < 1 Hz) using the 3-D finite difference method, assuming a point source and adopting a 3-D velocity model for the heterogeneous structure. We apply a correction for the effect of the local surface layers not included in Boore's method or the 3-D calculation. After that, we calculate the hybrid Green's function by combining the low and high frequency motions in the time domain. A matched pair of filters is then used to remove the low (less than 1 Hz) and high frequency content (more than 1 Hz) from the stochastically simulated motion and the finite difference synthetic motion, respectively, and to follow the ω^{-2} spectral contents with respect to its source effect. Finally, the strong ground motions from the large earthquake are simulated by the summation of the hybrid Green's functions, following the EGF method of Irikura (1986).

We applied this method to simulating the ground motions from the 1995 Kobe earthquake (M_w 6.9). The assumed source model consisted of three asperities (No. 1, 2, and 3), as shown in Fig. 2. The hybrid Green's functions were calculated for three point sources located at the centers of those three asperities, assuming a magnitude of 4.7, which almost coincided with the aftershock records used in the empirical Green's function simulation (Kamae and Irikura, 1998).

For each point source, we assumed a pure right-lateral strike-slip mechanism, with the strike and dip corresponding to each subfault. The map and station locations are shown in Fig. 3. The basin velocity model used in the 3-D finite difference calculations included a single sedimentary layer with an S wave velocity V_s = 0.8 km/s, P-wave velocity V_p = 1.6 km/s, density ρ = 2.1 g/cm^3, constant attenuation factor Q = 80,

and a background 1-D velocity. The underground bedrock tomography is depicted in Fig. 4.

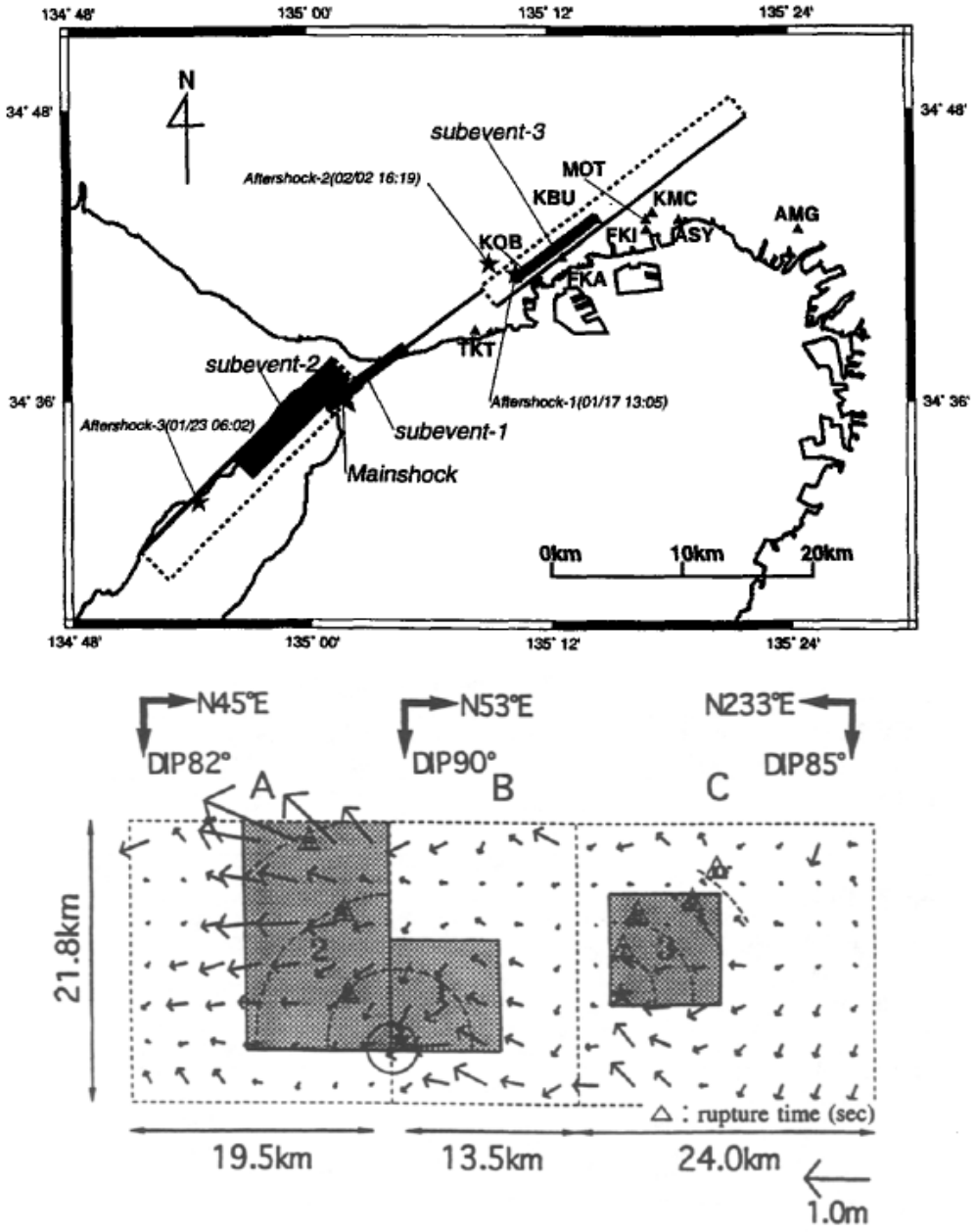

Figure 2. Source model consisting of three asperities (Kamae and Irikura, 1998a). Asperities 1, 2, and 3 are indicated by the hatched areas (after Kamae *et al*., 1998).

The acceleration hybrid Green's functions at MOT for the second and third asperities are schematically shown in Fig. 5. The upper figure (3D-sim) shows the low frequency motion assuming a pure right-lateral strike slip source in the 3-D basin velocity structure. The middle figure (STOC-sim) is the high frequency motion found

by the stochastic simulation technique, considering the propagation-path effects due to a frequency-dependent Q factor (Q_s = 33f) estimated from the linear inversion of the ground motion spectra observed around the basin and the local site effects from the 1-D structure modeling. The bottom figure (HYBRID) shows the hybrid Green's function.

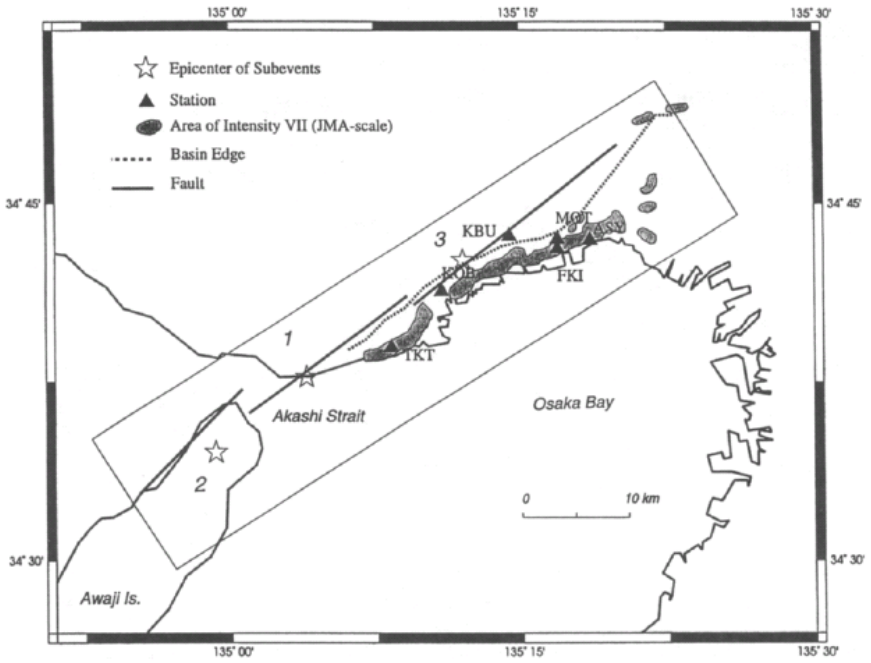

Figure 3. Map of the Kobe area and station locations. The locations of the heavily damaged zone are shown by shading. The solid triangles indicate the locations of the mainshock observation stations (TKT, KOB, KBU, and MOT) and the aftershock observation stations (FKI and ASY). The solid lines show the surface intersections of the causative faults (after Kamae *et al*., 1998).

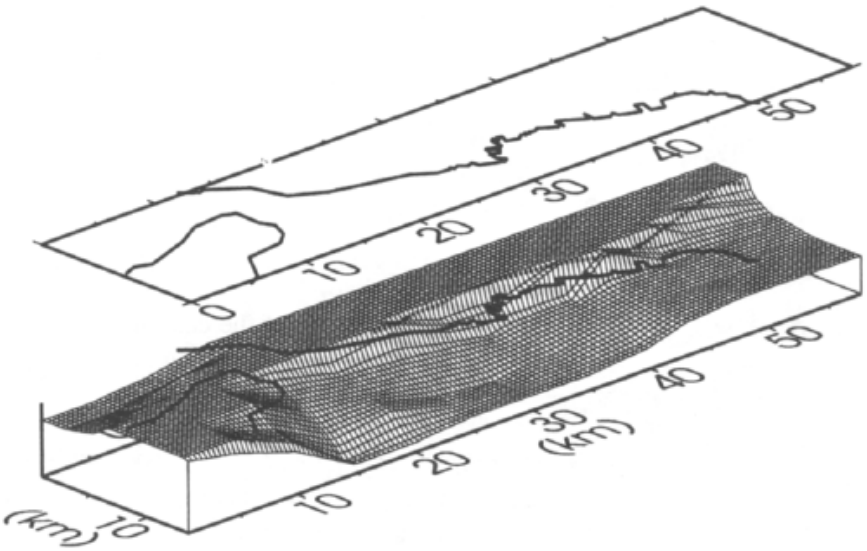

Figure 4. The bedrock topography in the Kobe area used in the 3-D finite difference modeling (after Pitarka *et al*., 1998).

Fig. 6 shows a comparison between the observed and synthesized seismograms (acceleration and velocity) at KBU, KOB, TKT, and MOT. The synthesized seismogram for each station was selected from 20 simulations, as the one whose peak acceleration amplitude was the closest to the simulated mean value. The standard deviations of the simulated peak amplitudes varied from 10 to 20%. Fig. 7 shows a comparison of the pseudo velocity response spectra. Also shown in this figure is the variation (the mean value and the mean value plus/minus one standard deviation) of the response amplitude in the short period range. The peak amplitudes of the simulated accelerations were close to those of the observed ones. The simulated velocity motions agreed well with those observed.

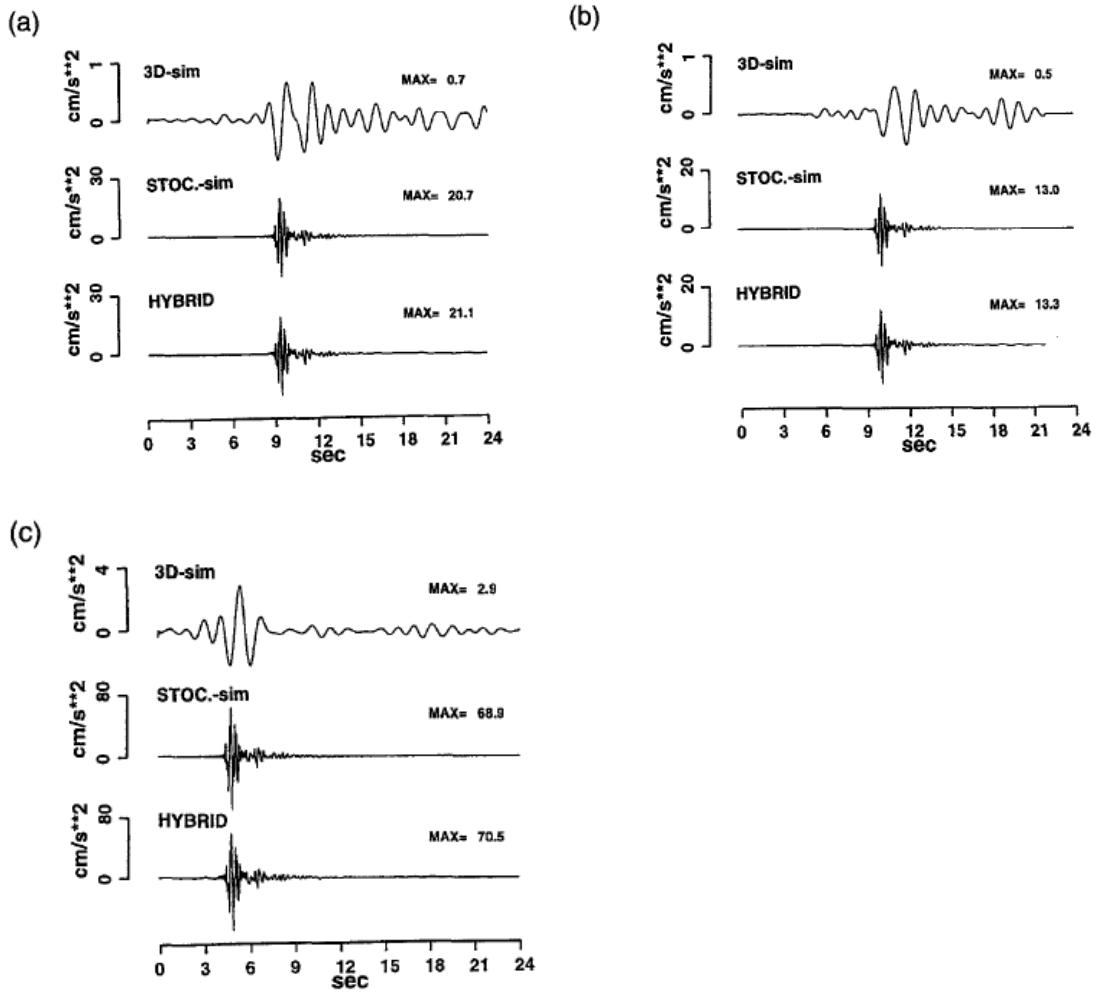

Figure 5. An example of the entire procedure used for estimating the acceleration of the hybrid Green's function. (a), (b), and (c) show the Green's functions for numbers 1, 2, and 3 hypothetical small events at MOT, respectively. In each figure, "3D-sim" shows the corrected low frequency Green's function, bandpass filtered between 0.2 and 1.0 Hz; "STOC-sim" shows the corrected

high-frequency Green's function, bandpass filtered between 1.0 and 10 Hz; and "HYBRID" shows the hybrid Green's function obtained by seismograms (after Kamae *et al*., 1998).

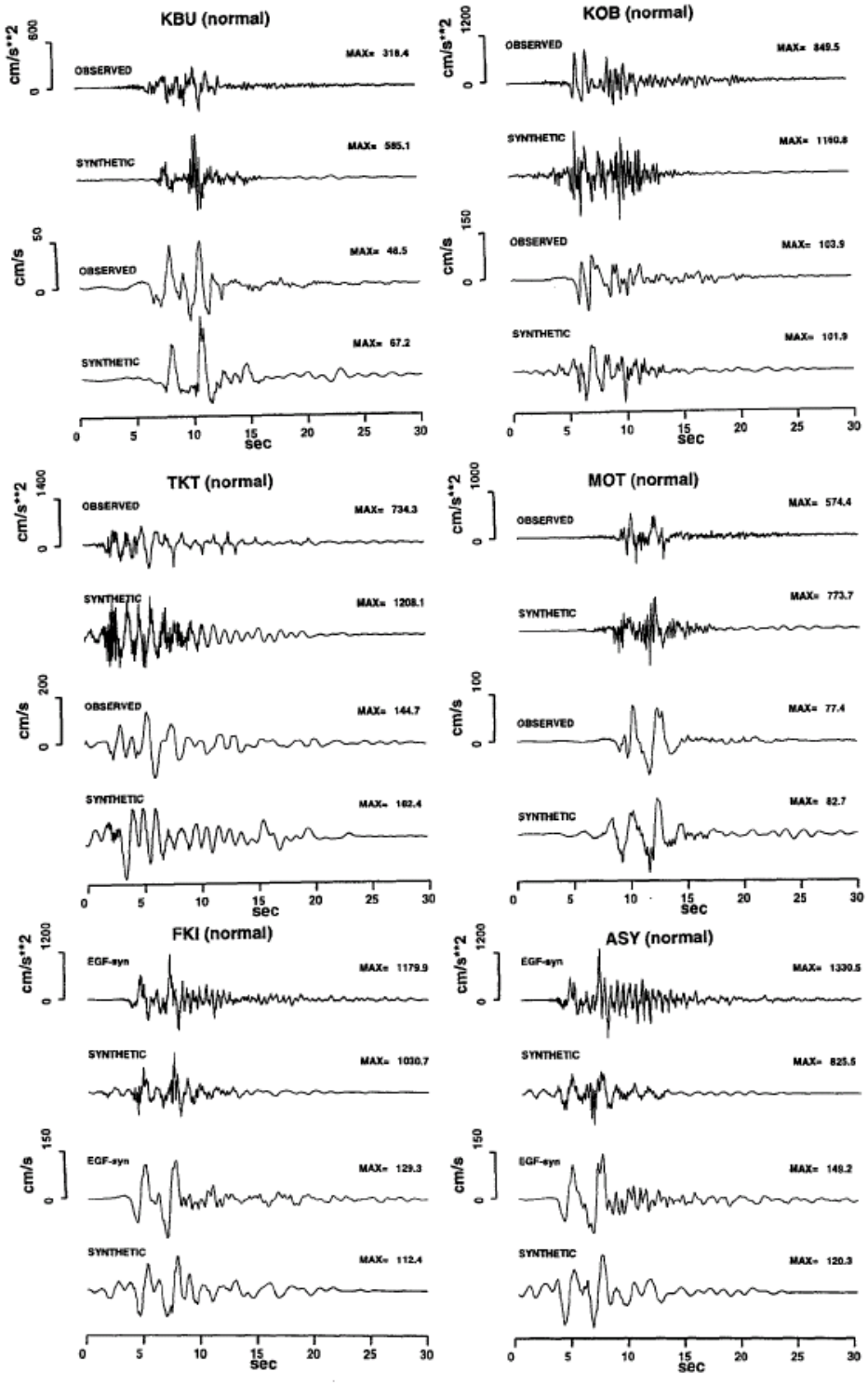

Figure 6. Comparison between the synthetic acceleration and velocity seismograms (fault-normal component) using hybrid Green's functions and those observed from the mainshock. The seismograms were bandpass filtered between 0.2 and 10.0 Hz. The synthetic seismograms were

selected from 20 simulations, based on the one whose peak acceleration amplitude was the closest to the simulated mean value (after Kamae *et al*., 1998).

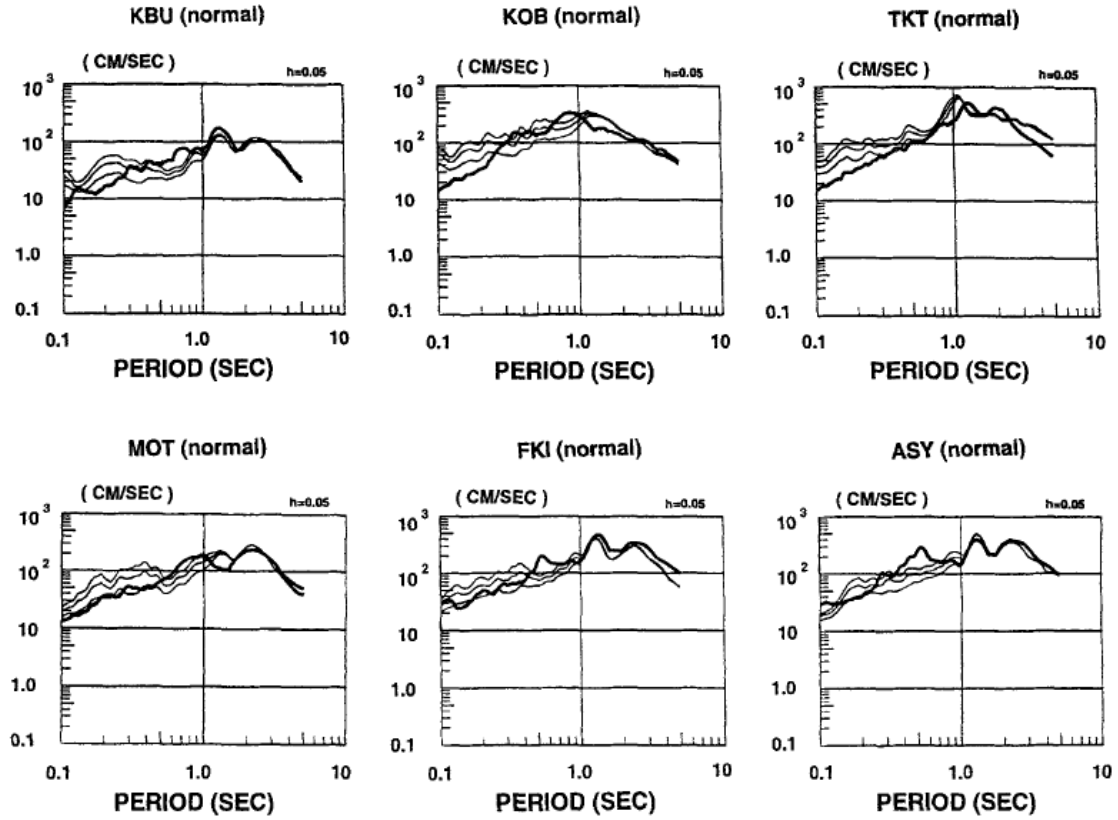

Figure 7. Comparison between the synthetic pseudo-velocity response spectra (the average plus/minus one standard deviation: light solid line) and the observed one (heavy solid line) (after Kamae *et al*., 1998).

The bottom of Figure 6 also shows a comparison between the seismograms synthesized with the hybrid Green's function method and those based on the EGF method at FKI and ASY in the heavily-damaged zone, where we did not have records of the mainshock ground motions. The excellent agreement between the synthetic seismograms shows that in regions where we have enough information about the deep and shallow geological structure, the HGF method performs as well as the EGM method.

The HGF method has the advantage of being very robust in simulating the broadband ground motions from a large earthquake without influence from detailed fault parameters, such as the variable rupture velocity and slip time function on the source fault. On the other hand, it is difficult to obtain theoretically simulated waveforms that precisely fit the observed waveforms, even at low frequencies. The other difficulty is that high frequency motions near the causative faults are

overestimated at soft-sediment sites because, according to Aguirre and Irikura (1997), this simulation does not account for non-linear soil behavior.

The Hybrid Synthetic Method

A flow chart for the hybrid synthetic method is shown in Fig. 8. The procedure that it uses for estimating the broadband ground motion from a large target earthquake is slightly different from the HGF method. The low-frequency motions from the large earthquake are directly simulated with the 3-D finite difference method, taking into account the slip distributions on the source fault and the velocity structures extending from the source to the sites. On the other hand, the high-frequency ground motions from the large earthquake are estimated using the same technique as the empirical Green's function method, using stochastically simulated small-event motions instead of observed ones. After that, the low and high frequency ground motions simulated by these two methods are summed in the time domain after passing through a pair of filters, as shown in Fig. 9.

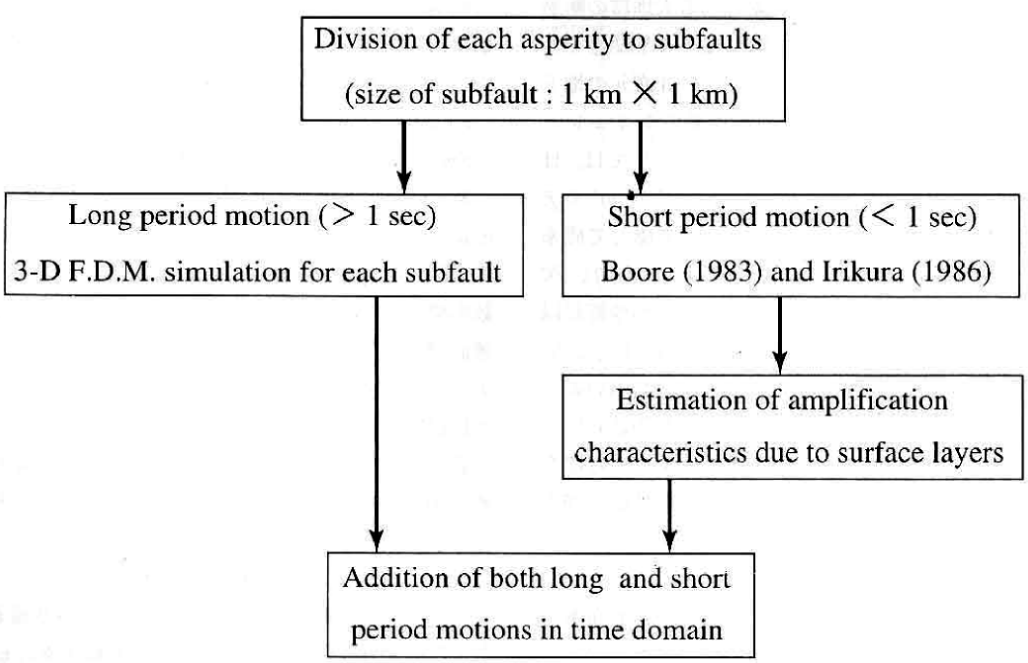

Figure 8. Flow chart for simulating strong ground motions from large earthquakes using the hybrid synthetic method (after Irikura and Kamae, 1999).

This method was adopted in Japan for the creation of the "Seismic Hazard Maps for Specified Seismic Source Faults" (Earthquake Research Committee, 2005a). This method was verified by simulating the broadband ground motions from the M_w 8.0

Tokachi-oki earthquake of 2003, a great subduction-zone earthquake that occurred off the Tokachi Region, Hokkaido, Japan (Earthquake Research Committee, 2005b; Morikawa *et al*., 2006). There was a large amount of strong motion data recorded for this earthquake at more than 600 K-NET and KiK-net stations. These data were very helpful in verifying the methodology for estimating strong ground motions by a comparison between the simulated results and observed results.

Fig. 10 shows a map and the observation stations, together with the source model. The rupture process of this earthquake has been studied by many researchers, through waveform inversions using strong motion data (e.g. Honda *et al*., 2004) and teleseismic body-wave data (Yamanaka and Kikuchi, 2003), a joint inversion of strong motion and geodetic data (Koketsu *et al*., 2004), and so on. The location and geometry of the source fault can be given from the aftershock distribution and the inversion results (e.g., Honda *et al*., 2004).

The outer fault parameters, such as the seismic moment and rupture area, can be estimated as follows. A seismic moment of 1.05 x 10^{21} Nm was estimated from the inversion results of the teleseismic data. The average stress drop was assumed to be 30 MPa (Kanamori and Anderson, 1975) and the fault area was estimated to be 30 x 30 km^2.

The inner fault parameters, such as the combined asperity areas and stress drop on asperities, were estimated following the "recipe" for subduction-zone earthquakes (e.g., Irikura, 2004). The number of asperities and their locations are not given by the "recipe," but can be inferred by reference to the inversion results from the strong motion data (Honda *et al*., 2004), as shown in Fig. 10.

The 3-D velocity structure model was based on the velocity profiles from the source area and reflection surveys obtained in the target site. It is very important to construct accurate structure models with deep sediments for simulating strong ground motions. However, the information for modeling the 3-D velocity structures is not sufficient to simulate ground motions higher than 0.2 Hz in this area. Therefore, the low frequency motions at less than 0.2 Hz (longer than 5 seconds) were theoretically simulated by the FDM, while the high frequency motions at more than 0.2 Hz (shorter than 5 seconds) were simulated by the SGF method. The low and high frequency motions simulated above were first calculated on engineering bedrock (V_s = 400- 600 m/s). The ground motions on the ground surface were calculated with a 1-D linear transfer function, due to the soil-sediments between the engineering bedrock and ground surface.

Fig. 11 shows an example of the comparison between the observed and

simulated waveforms (velocity) at HKD129. The uppermost two traces are the observed NS and EW components and the third is the high frequency motions synthesized by the SGF method. The observed waveforms shown in the forth and fifth traces of Fig. 11 were band-pass-filtered between 0.2 and 0.04 Hz (5 and 25 seconds) to compare them with the theoretically simulated low frequency motions and the high frequency motions derived from the SGF method, both of which were band-pass-filtered in the same frequency range as those observed. A comparison of the pseudo velocity response spectra of the observed and simulated motions are shown at the bottom of Fig. 11. We found that the theoretical waveforms and response-spectra agreed well with the observed ones at periods between 5 and 25 seconds. The high frequency motions from the SGM method also coincided with the observed ones at spectral levels higher than 1 Hz, i.e., shorter than 1 second.

Fig. 12 shows a comparison of the totally synthesized motions and those observed at three sites, TKCH11, HDKH05, and HKD093, very near the source fault. We found that the synthesized motions at those sites agreed well with the observation records. However, there were several stations where the theoretically simulated motions were not consistent with the observed ones in waveform and/or spectral level. This can be attributed to the unreliability of the 3-D structural model, and the fact that some of the fault parameters, such as the rupture velocity and slip time function, are very sensitive to the ground motions in theoretical simulations. On the other hand, the high frequency motions calculated by the SGF method are not sensitive to such fault parameters, but are strongly dependent on the inner fault parameters related to asperities, such as location, size, and stress drop.

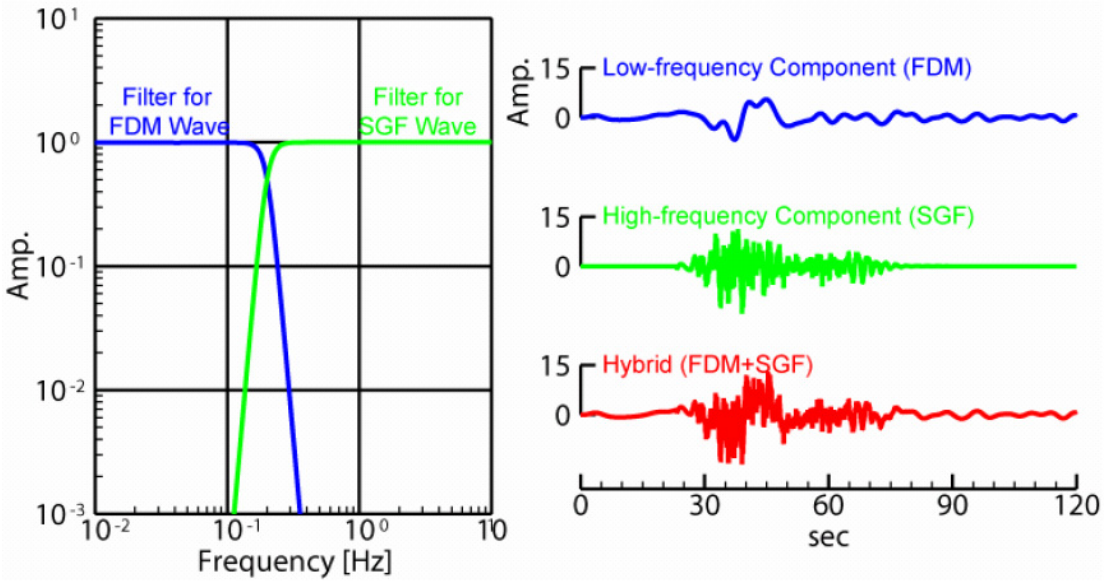

Figure 9. A pair of filters for the hybrid method and an example of synthesizing the broadband ground motions from a large earthquake (after Morikawa *et al*., 2006).

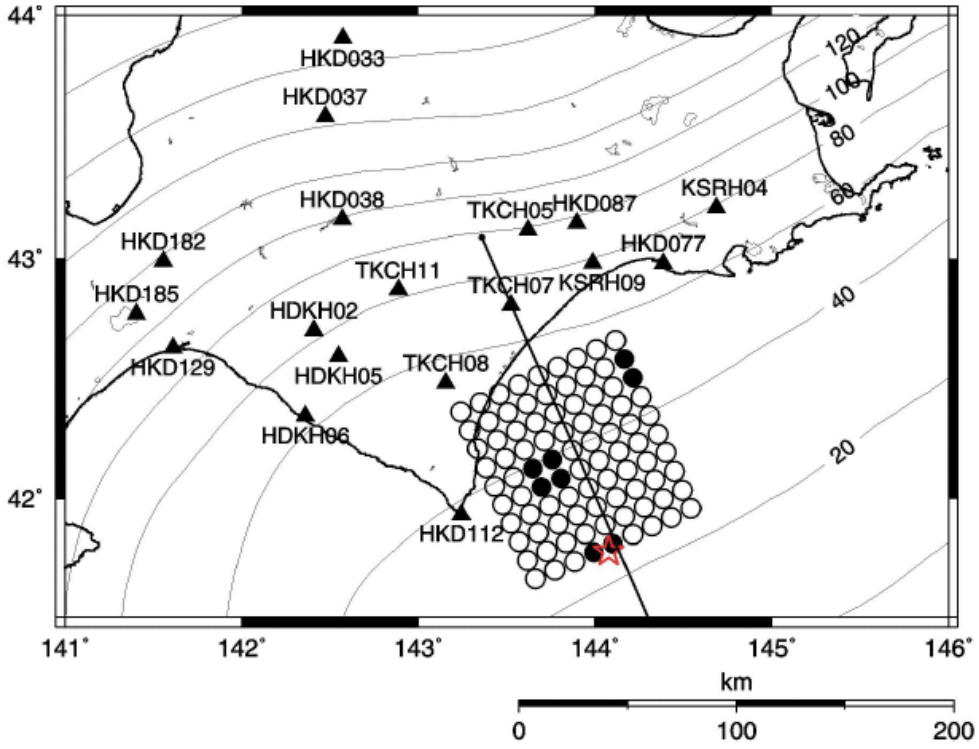

Figure 10. Source model of the 2003 Tokachi-oki earthquake (M_w 8.0), with three asperities. The fault plane is divided into 9 x 9 subfaults. The asperity areas and backward area are indicated by solid and open circles, with each circle corresponding to a subfault. Solid triangles show the locations of the observation stations (after Earthquake Research Committee, 2004).

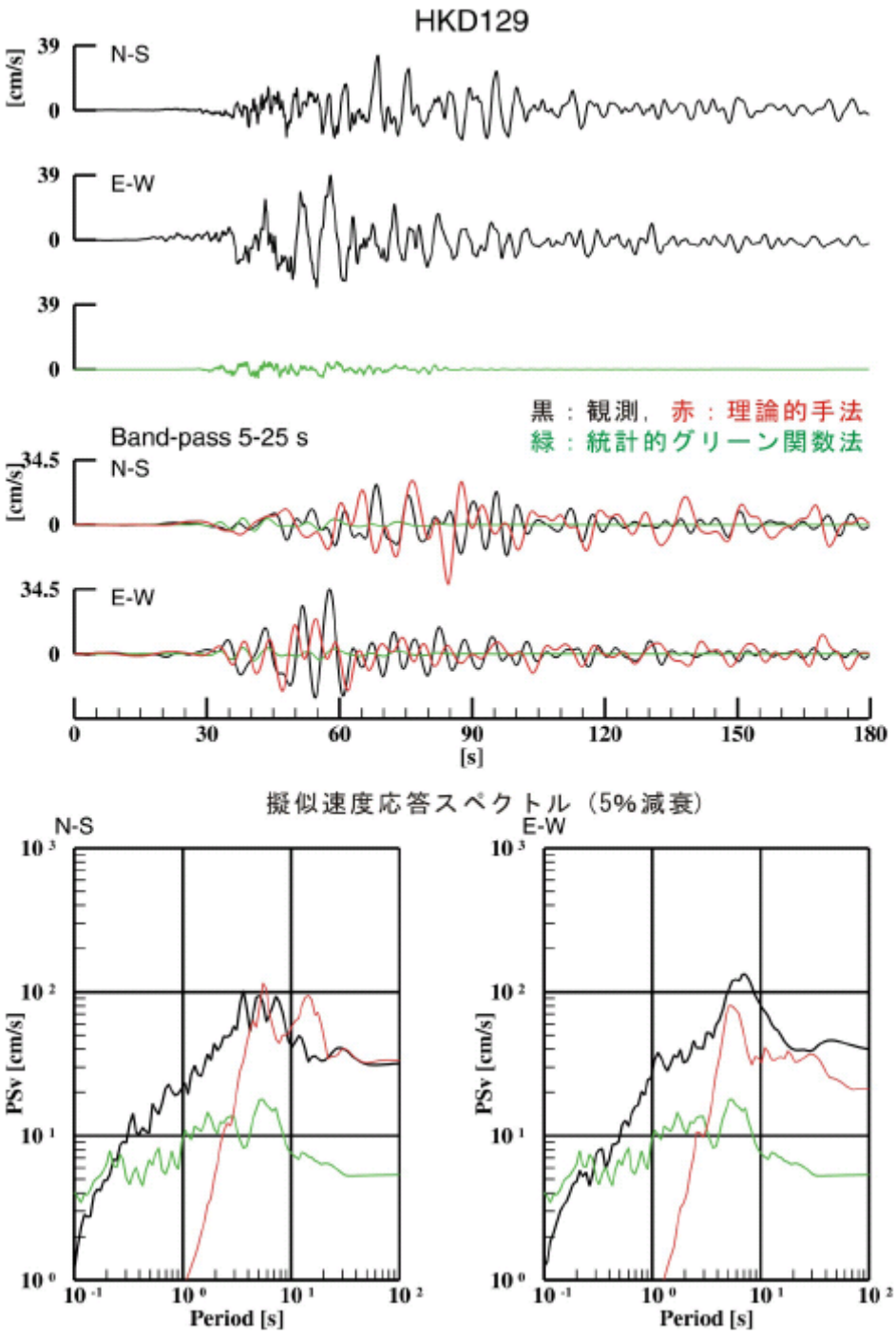

Figure 11. A comparison between the observed motions (black) and motions simulated by the theoretical method (FDM) (red) and the stochastic Green's function method (green). The bottom two panels show the corresponding pseudo-velocity response spectra (5% damping) (after Earthquake Research Committee, 2004).

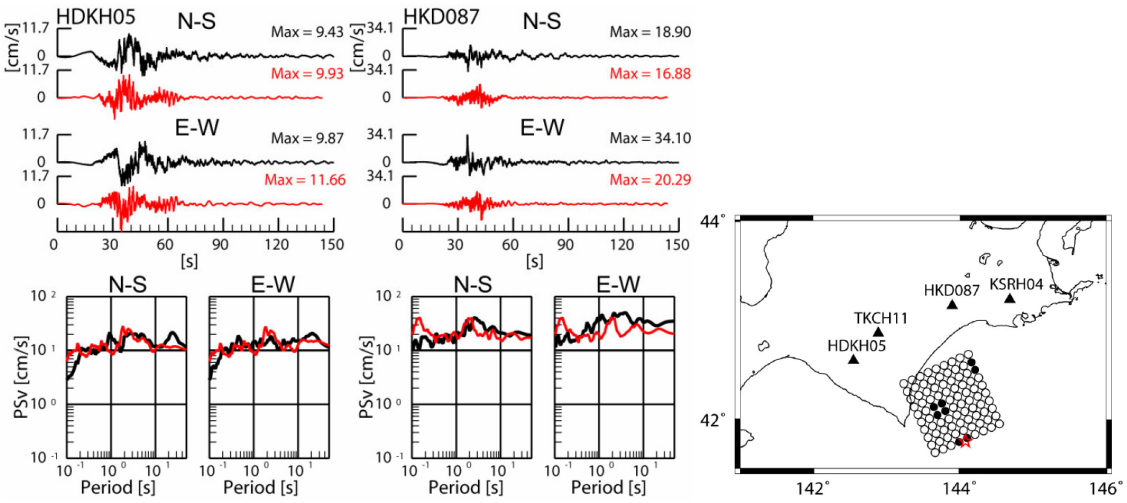

Figure 12. Comparison of observed (black) and simulated (red) velocity ground motions and pseudo-velocity response spectra (PSv, h = 0.05) for the 2003 Tokachi-oki earthquake (after Morikawa *et al*., 2006). A map showing the source model and observation stations is at the right (after Morikawa *et al*., 2007).

Conclusion

We introduced two methods for simulating the broadband ground motions from large earthquakes, the hybrid Green's function (HGF) method and the hybrid synthetic method.

In the HGF method, the hybrid Green's function is first estimated by combining the low frequency motions calculated by the finite-difference method and the high frequency motions calculated by the stochastic method. After that, the strong ground motions from the large earthquake are simulated by the summation of the hybrid Green's functions, following the EGF method of Irikura (1986). This method was examined by comparing synthetic ground motions with observation records from the 1995 Kobe earthquake (M_w 6.9). This comparison suggested that the HGF method is effective at simulating near-source ground motions in the broad-frequency range of interest to engineers. The HGF method has the advantage of being very robust in simulating the broadband ground motions from a large earthquake without influence from detailed fault parameters, such as a variable rupture velocity and slip time function on the source fault. On the other hand, the theoretically simulated waveforms are not precise enough to compare with the observed waveforms, even at low frequencies. One of the other problems is that high-frequency motions near the causative faults are overestimated at soft-sediment sites, because this simulation is not considered to have non-linear soil behavior.

In the hybrid synthetic method, the low-frequency motions and

high-frequency motions from a large earthquake are simulated separately, theoretically by the finite difference method and stochastically by the stochastic Green's function method. After that, the low and high frequency ground motions simulated by these two methods are summed in the time domain after passing through a pair of filters. This method was verified by comparing the simulated broadband ground motions with the observed motions from the 2003 Tokachi-oki earthquake (M_w 8.0). The totally synthesized motions agreed well with the observation records from many stations near the source fault. However, there were some stations where the theoretically simulated motions were not consistent with the observed ones in waveform and/or spectral level. These discrepancies between the synthesized and observed motions are attributed to the unreliability of the 3-D structural model, as well as the inaccuracy of the rupture velocity and slip time function. On the other hand, the high frequency motions calculated by the SGF method are not sensitive to such fault parameters, but are strongly dependent on the inner fault parameters related to asperities, such as location, size, and stress drop.

References

Aguirre, J. and K. Irikura (1997). Nonlinearity, liquefaction, and velocity of soft soil layers in Port Island, Kobe, during the Hyogo-ken Nanbu earthquake, *Bull. Seismol. Soc. Am*., **87**, 1244-1258.

Boore, D. M. (1983). Stochastic simulation of high-frequency ground motions based on seismological models of the radiated spectra, *Bull. Seismol. Soc. Am*., **73**, 1865-1894.

Graves, R. W. (1995). Preliminary analysis of long-period basin response in the Los Angeles region from the 1994 Northridge earthquake, *Geophys. Res. Lett*., **22**, 101-104.

Earthquake Research Committee (2005a). National Seismic Hazard Map for Japan (2005), *Report published by the Headquarter of Earthquake Research Promotion under the Ministry of Education, Culture, Sports, Science, and Technology,* 121p. (in Japanese).

Earthquake Research Committee (2005b). Verification results using observed records of the 2003 Tokachi-Oki Earthquake, *National Seismic Hazard Map for Japan (2005)*, http://www.jishin.go.jp/main/index-e.html

Hartzell, S. H. (1978). Earthquake aftershocks as Green's functions, *Geophys. Res. Lett*., **5**, 1-4.

Hartzell, S., A. Leeds, A. Frankel, and J. Michael (1996). Site response for urban Los Angeles using aftershocks of the Northridge earthquake, *Bull. Seismol. Soc. Am*., **86**,

S168-S192.

Heaton, T. H., J. F. Hall, D. J. Wald, and M. N. Halling (1995). Response of high-rise and base-isolated buildings to hypothetical M_w 7.0 blind thrust earthquake, *Science*, **267**, 206-211.

Honda, R., S. Aoi, N. Morikawa, H. Sekiguchi, K. Kunugi, and H. Fujiwara (2004). Ground motion and rupture process of the 2003 Tokachi-oki earthquake obtained from strong motion data of the K-NET and KiK-net, *Earth Planets Space*, **56**, 317-322.

Horikawa, H., K. Hirahara, Y. Umeda, M. Hashimoto, and F. Kusano (1996). Simultaneous inversion of geodetic and strong motion data for the source process of the Hyogo-ken Nanbu, Japan, earthquake, *J. Phys. Earth*, **44**, 455-472.

Ide, S. and M. Takeo (1996). Source process of the 1995 Kobe earthquake: Determination of spatio-temporal slip distribution by Bayesian modeling, *Bull. Seismol. Soc. Am*., **86**, 547-566.

Irikura, K. (1986). Prediction of strong acceleration motion using empirical Green's function, *Proc. 7th Japan Earthq. Symp*.,151-156.

Iwata, T., K. Hatayama, H. Kawase, K. Irikura, and K. Matsushima (1995). Array observation of aftershocks of the 1995 Hyogoken-Nanbu earthquake at Higashinada ward, Kobe city, *J. Natural Disaster Science*, **16**, 41-48.

Iwata, T., K. Hatayama, H. Kawase, and K. Irikura (1996). Site amplification of ground motions during aftershocks of the 1995 Hyogo-ken Nanbu earthquake in severely damaged zone -Array observation of ground motions at Higashinada ward, Kobe city, Japan-, *J. Phys. Earth*, **44**, 553-562.

Kagawa, T., K. Irikura, and I. Yokoi (1996). Restoring clipped records of near-field strong ground motion during the 1995 Hyogo-ken Nanbu (Kobe), Japan earthquake, *J. Natural Disast. Science*, **18**, 43-57.

Kamae, K., P. Y. Bard, and K. Irikura (1998). Prediction of strong ground motion in a EURO-SEISTEST using the empirical Green's function method, *Journal of Seismology*, **2**, 193-207.

Kamae, K. and K. Irikura (1998). Source model of the 1995 Hyogo-ken Nanbu earthquake and simulation of near-source ground motion, *Bull. Seismol. Soc. Am*., **88**, 400-412.

Kawase, H. (1996). The cause of the damage belt in Kobe: "The basin edge effect," constructive interference of the direct S wave with the basin-induced diffracted/Rayleigh waves, *Seismol. Res. Lett*., **67**, 25-34.

Kinoshita, S. (1998). Kyoshin-net (K-NET), *Seismol. Res. Lett*. **69**, 309-332.

Koketsu, K., K. Hikima, S. Miyazaki, and S. Ide (2004). Joint inversion of strong

motion and geodetic data for the source rupture process of the 2003 Tokachi-oki, Hokkaido, earthquake, *Earth Planets Space*, **56**, 329-334.

Morikawa, N., S. Aoi, R. Honda, S. Senna, Y. Hayakawa, and H. Fujiwara (2006). Application of the "recipe for strong ground motion evaluation" to the 2003 Tokachioki, Japan, earthquake, *Third International Symposium on the Effects of Surface Geology on Seismic Motion*, Paper No. 48.

Morikawa, N., H. Fujiwara, S. Kawai, S. Aoi, T. Kunugi, T. Ishii, Y. Hakayawa, R. Honda, K. Kobayashi, M. Ooi, S. Senna, and N. Okumura (2007). Application of the strong-motion prediction method to the 2003 Tokachi-oki earthquake, *Technical Note of the National Research Institute for Earth Science and Disaster Prevention*, **303,** 149pp.

Motosaka, M. and M. Nagano (1996). Analysis of ground motion amplification characteristics in Kobe city considering a deep irregular underground structure - Interpretation of heavily damaged belt zone during the 1995 Hyogo-ken Nanbu earthquake, *J. Phys. Earth*, **44**, 577-590.

Nakamura, Y., F. Uehara, and H. Inoue (1996). Waveform and its analysis of the 1995 Hyogo-Ken-Nanbu earthquake (-6), JR Earthquake Information No. 23d, *Railway Technical Research Institute*, March. (in Japanese)

Pitarka, A. and K. Irikura (1996). Basin structure effects on long period strong motions in the San Fernando valley and the Los Angeles Basin from the 1994 Northridge earthquake and an aftershock, *Bull. Seismol. Soc. Am*., **86**, S126-S137.

Pitarka, A., K. Irikura, T. Iwata, and T. Kagawa (1996). Basin structure effects in the Kobe area inferred from the modeling of ground motions from two aftershocks of the January 17, 1995 Hyogoken-Nanbu earthquake, *J. Phys. Earth*, 44, 563-576.

Pitarka, A., K. Irikura, and T. Iwata (1997a). Modeling of ground motion in Higashinada (Kobe) area for an aftershock of the January 17, 1995 Hyogo-ken Nanbu, Japan, earthquake, *Geophys. J. Int*., **131**, 231-239.

Pitarka, A., K. Irikura, T. Iwata, and H. Sekiguchi (1998). Three-dimensional simulation of the near-fault ground motion for the 1995 Hyogo-ken Nanbu (Kobe), Japan earthquake, *Bull. Seismol. Soc. Am*., **88**, 428-440.

Pitarka, A., P. Somerville, Y. Fukushima, T. Uetake, and K. Irikura (2000). Simulation of Near-Fault Strong-Ground Motion Using Hybrid Green's Functions, *Bull. Seismol. Soc. Am*., **90**, 566-586.

Sekiguchi, H., K. Irikura, T. Iwata, Y. Kakehi, and M. Hoshiba (1996). Minute locating of faulting beneath Kobe and the waveform inversion of the source process during the 1995 Hyogo-ken Nanbu, Japan, earthquake using strong ground motion records, *J.*

Phys. Earth, **44**, 473-488.

Wald, D. J. (1996). Slip history of the 1995 Kobe, Japan, earthquake determined from strong motion, teleseismic, and geodetic data, *J. Phys. Earth*, **44**, 489-504.

Yamanaka, Y. and M. Kikuchi (2003). Source process of the recurrent Tokachi-oki earthquake on September 26, 2003, inferred from teleseismic body waves, *Earth Planets Space*, **55**, e21-e24.

Yoshida, S., K. Koketsu, B. Shibazaki, T. Sagita, T. Kato, and Y. Yoshida (1996). Joint inversion of near- and far-field waveforms and geodetic data for the rupture process of the 1995 Kobe earthquake, *J. Phys. Earth*, **44**, 437-454.

Chapter 5. Recipe for Predicting Strong Ground Motion

Summary

A recipe for estimating the strong ground motions from specific earthquakes is proposed based on the source characteristics from the waveform inversion using strong motion data. The main features of the source model are characterized by three kinds of parameters, which we call: outer, inner, and extra fault parameters. The outer fault parameters are used to outline the overall picture of a target earthquake, such as the entire source area and seismic moment. The inner fault parameters are used to characterize the stress heterogeneity inside the fault area. The extra fault parameters are considered to complete the source model, and include the starting point and propagation pattern of the rupture. Two governmental organizations, the Headquarters of the Earthquake Research Center and the Central Disaster Prevention Council of Japan, used the idea behind the recipe proposed here to make seismic hazard maps for future large earthquakes with a high probability of occurrence.

Introduction

From recent developments in relation to waveform inversion analyses for estimating the rupture process using strong motion data during large earthquakes, we now understand that strong ground motion is related to the slip heterogeneity inside the source rather than the average slip over the entire rupture area. Asperities are characterized as regions that have large slip relative to the average slip of the rupture area, based on heterogeneous slip distributions estimated from the source inversion (Somerville *et al*., 1999). Somerville *et al*. (1999) also found that the asperity areas, as well as the entire rupture areas, scale with the total seismic moment. Another important study for strong motion prediction found that the strong motion generation areas approximately coincided with the asperity areas, which were the primary areas where stresses were released (Miyake *et al*., 2001; 2003).

Based on the two kinds of scaling relationships, for the entire rupture area and for the asperity areas with respect to the total seismic moment, we found that the source model for the prediction of strong ground motions was characterized by three kinds of parameters: outer, inner, and extra fault parameters. The outer fault parameters are conventional parameters characterizing the size of an earthquake, such as the rupture area and seismic moment, which give an overall picture of the source fault. The inner

fault parameters are newly introduced in this study to define the slip heterogeneity inside the seismic source. These include the combined area of the asperities and the stress drop of each asperity, which have a much greater influence on the strong ground motions. The extra fault parameters are used to characterize the rupture nucleation and termination, such as the starting point and propagation pattern of the rupture.

So far, most of strong motion predictions in earthquake hazard analyses have been made using empirical attenuation-distance curves for PGA (peak ground acceleration) and PGV (peak ground velocity), in which the source information is defined exclusively by the seismic magnitude and fault area, as types of outer fault parameters. However, from the source inversion studies mentioned above, we realized that such parameters are not sufficient for estimating strong ground motions.

We therefore developed a "recipe" for predicting strong ground motions (Irikura and Miyake, 2001; Irikura, 2004), which involves characterizing the three previously mentioned kinds of fault parameters for the source modeling of future large earthquakes. The idea behind this "recipe" was applied in the creation of the Seismic Hazard Map for Specified Seismic Source Faults by the Headquarters for Earthquake Research Promotion and the Central Disaster Prevention Council of Japan.

Strong Motion Prediction Program in Japan

The basic policy for defining seismic hazards in Japan is based on the 1999 fundamental mission statement governing earthquake research over the next ten years as "The promotion of earthquake research – comprehensive basic policies for the promotion of seismic research through the observation, measurement, and survey of earthquakes–," established by the Headquarters for Earthquake Research Promotion (Director: Ministry of Education, Culture, Sports, Science, and Technology). It initiated the creation of seismic hazard maps by promoting the survey of active faults, long-term evaluation of occurrence potentials, and prediction of strong ground motion.

Two subcommittees were established under the Headquarters. The Subcommittee for Long Term Evaluations was formed in 1995 to evaluate the probabilities of earthquakes occurring at active faults and plate boundaries. The Subcommittee for Strong Motion Evaluations was formed in 1998 to create seismic hazard maps using two different approaches, probabilistic and deterministic.

A probabilistic seismic hazard map shows the predicted likelihood of a ground motion level, such as a PGA, PGV, or seismic intensity, occurring in a given area within a set period of time, as shown in Fig. 1. It provides important information for land use planning, structural design standards, and enlightening the public about seismic risks.

A deterministic seismic hazard map shows a distribution of the ground motion level predicted for individual specific earthquakes, assuming their fault models. The strong ground motions at specific sites near each source fault are estimated as a time history, based on a recipe characterizing the source and a numerical synthesis of waveforms with a hybrid scheme. Long-period motions are calculated with the finite difference method, considering the 3-D structures from the source to the target sites, and short-period motions are simulated with the stochastic Green's function method (e.g. Irikura and Kamae, 1999). The PGA, PGV, seismic intensity, and so on are easily evaluated once the time histories of the ground motions are estimated. The time histories of the ground motions are useful for nonlinear dynamic analyses of structures, which are needed to design earthquake-resistant buildings and critical structures, such as bridges, lifelines, electric power plants, and so on.

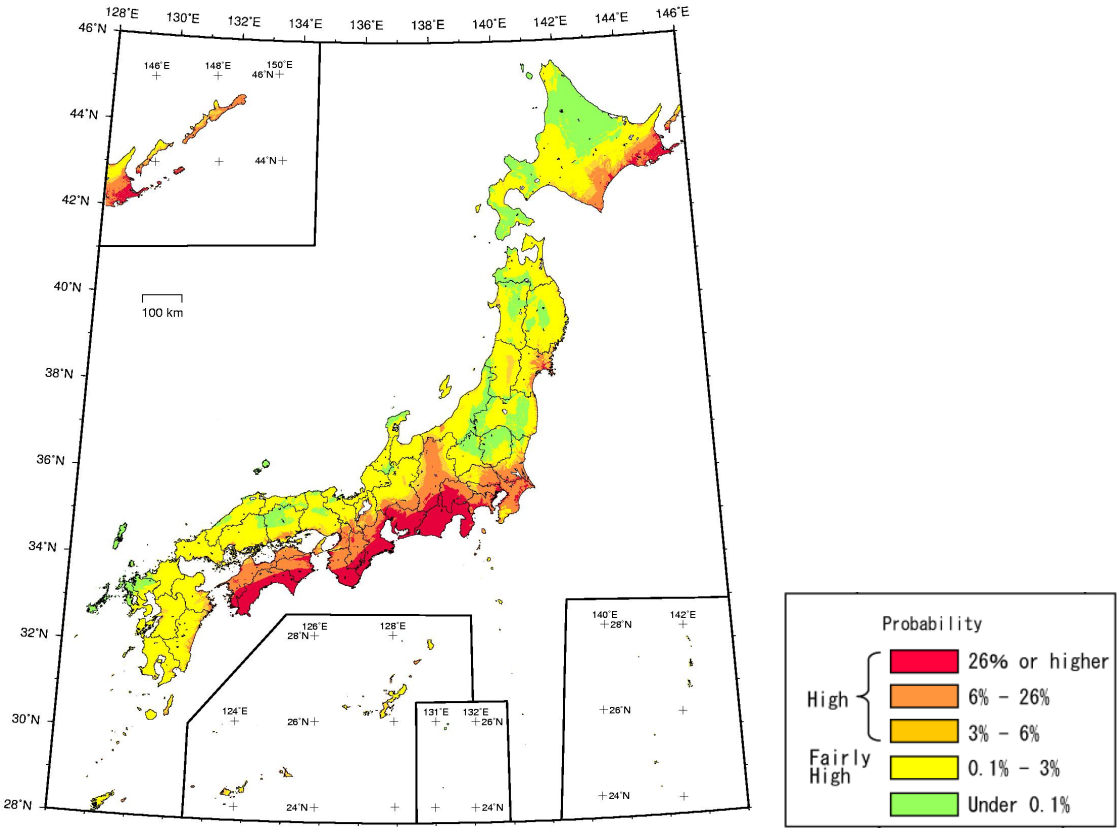

Figure 1. Probability of experiencing strong motion greater than seismic intensity 6- within 30 years, from 2005 (Earthquake Research Committee, 2005).

As shown in Fig. 2, the Central Disaster Prevention Council of the Cabinet Office also made deterministic seismic hazard maps for earthquakes in Tokai, Tonankai,

and Nankai, which are feared to be likely to occur within the next half century. They made damage and causality estimates to determine disaster management plans for those earthquakes.

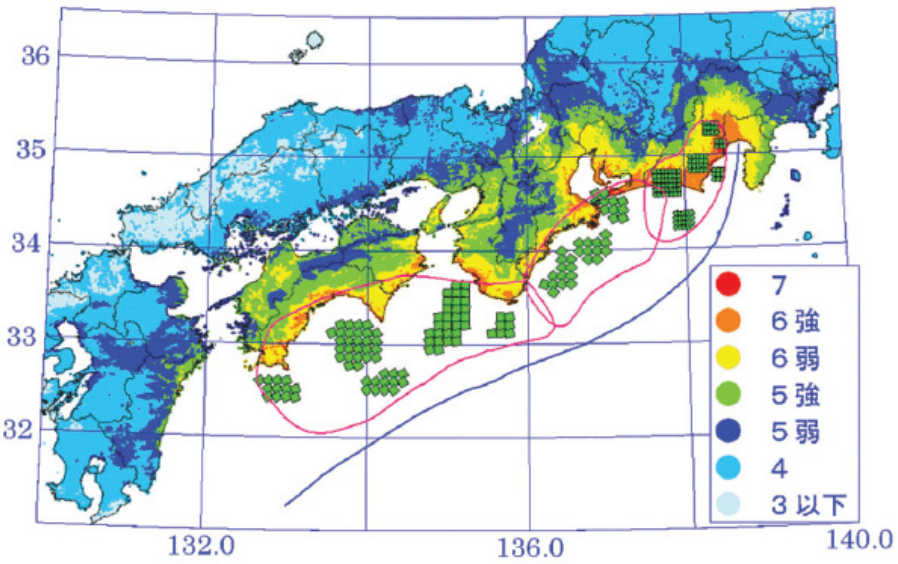

Figure 2. Seismic intensity map for three earthquakes, the Tokai, Tonankai, and Nankai earthquakes continuously activated (after Irikura, 2006 based on Central Disaster Prevention Council, 2003).

Scaling Relationships of Fault Parameters

Most of the difficulties in predicting strong ground motion are related to characterizing the source models for future earthquakes. Conventional scaling relations for the fault parameters, such as the fault length and average slip on the fault based on the seismic magnitude, are mostly determined geologically from surface offsets and geophysically from forward source modeling, using teleseismic data and geodetic data (e.g., Kanamori and Anderson, 1975). Those data are only available for very long period motions and are insufficient for the near-source strong motions dominating short period motions of less than 1 sec, which are of interest to engineers. The scaling of the fault parameters based on the waveform inversion results for the source process using the strong motion data gives a clue to solve this problem. We found two kinds of scaling relationships, one for the outer and the other for the inner fault parameters.

Outer Fault Parameters

The scaling for the outer fault parameters, i.e., the relationship between the seismic moment and rupture area, for inland crustal earthquakes are summarized as shown in Fig. 1(a) (Irikura *et al*., 2004). For earthquakes with a relatively small seismic

moment of less than 10^{19} Nm, the total fault area S seems to follow the self-similar scaling relation, with a constant static stress drop in proportion to the two-thirds power of the seismic moment M_0. For large earthquakes of more than 10^{-19} Nm, the scaling tends to depart from the self-similar model (Irikura and Miyake, 2001), corresponding to the saturation of the fault width due to the seismogenic zone size. Such a two-stage scaling relationship was also found by Hanks and Bakun (2002). We added one more stage for extra large earthquakes of more than 10^{-21} Nm, based on the idea of Scholz (2002), changing from an L-model into a W-model. As shown by the broken lines in Fig. 3(a), the scaling relationships in this study were drawn assuming that the fault width saturates with 20 km.

(a)

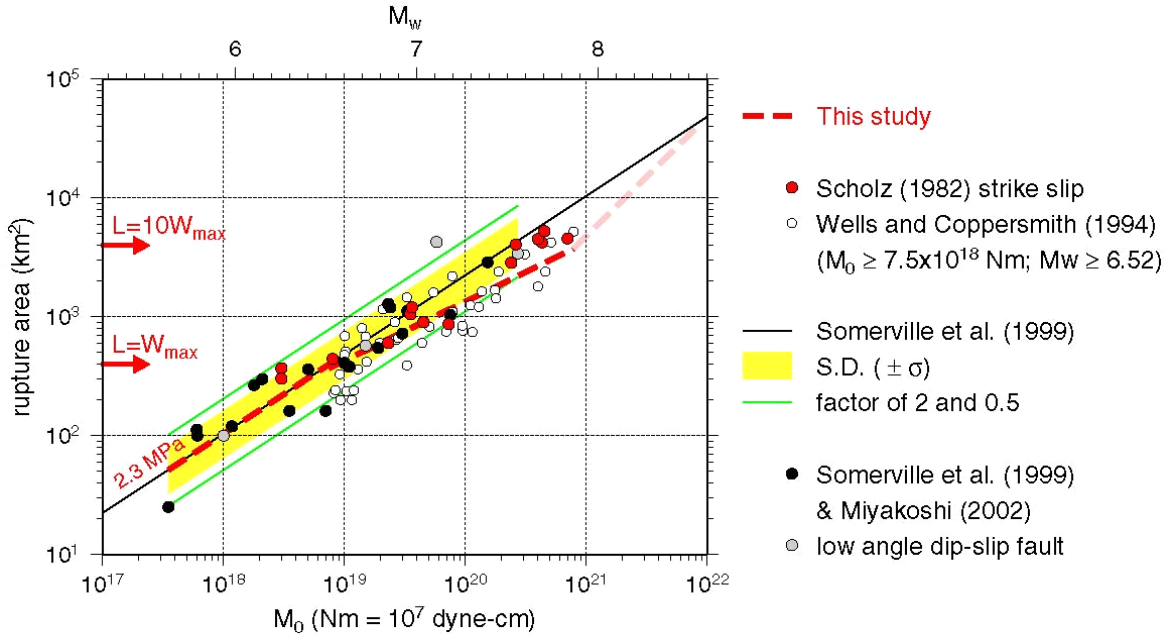

(b)

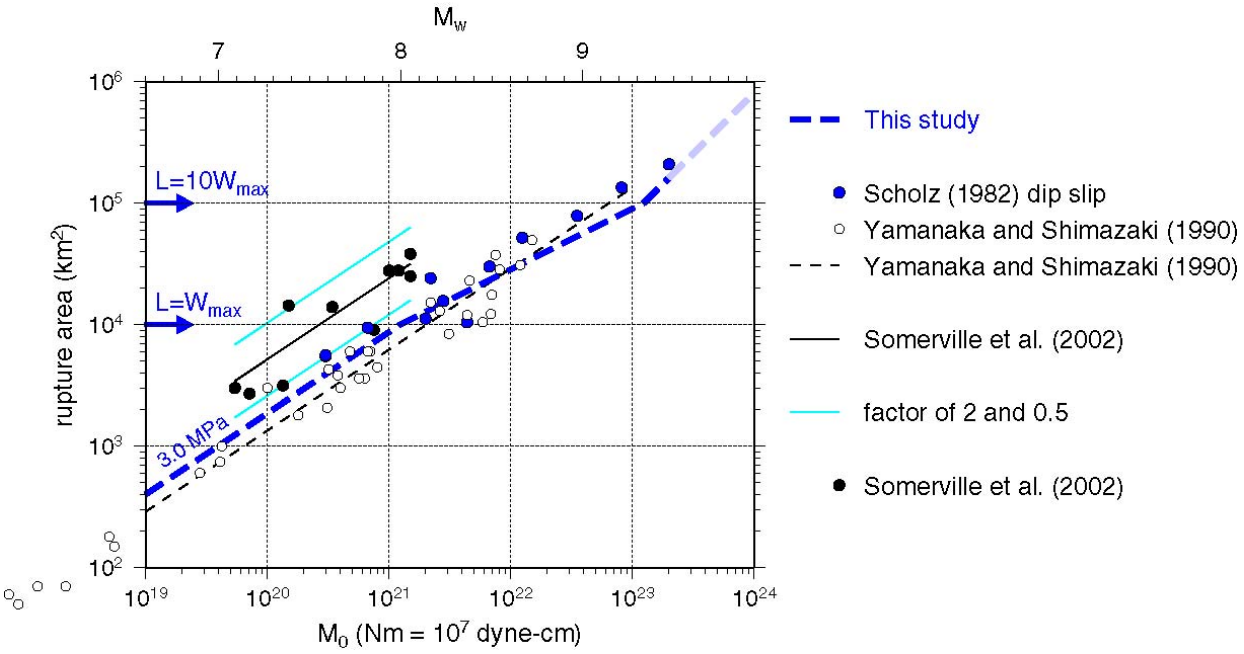

Figure 3. Empirical relationships between seismic moment and rupture area for inland crustal earthquakes (a) and subduction-zone earthquakes (b). The thick broken lines are the 3-stage scaling relationships proposed by our studies (e.g., Irikura *et al*., 2004).

Three-stage scaling also seems to be applicable for subduction-zone earthquakes, as shown in Fig. 3(b), although the bending points are different. The saturation of the fault width for the subduction-zone earthquakes becomes longer.

Inner Fault Parameters

Strong ground motions are more influenced by the inner fault parameters representing the slip heterogeneity than by the outer fault parameters. The relationships between the rupture area S, as the outer fault parameter, and the combined area of the asperities S_a, as the inner fault parameter, are shown in Fig. 4 (Irikura *et al*., 2004). The ratio S_a/S seems to be constant regardless of the rupture area, with a value of about 0.22 for an inland earthquake and about 0.25 for a subduction earthquake. Then, the stress drop on the asperities $\Delta\sigma_a$ is derived by multiplying the average stress drop over the fault $\Delta\overline{\sigma}_c$ by the ratio of the total rupture area S to the asperity area S_a (e.g., Madariaga, 1979).

$$\Delta\sigma_a = \Delta\overline{\sigma}_c \cdot \frac{S}{S_a} \tag{1}$$

Another empirical-relationship related to the inner source parameters is shown in Fig. 3. The relationship between the seismic moment M_0 and acceleration source spectral level A_0 was originally found by Dan *et al.* (2001) and was confirmed by other researchers (Morikawa and Fujiwara, 2003; Satoh, 2004).

$$A_0^a\,(dyne \cdot cm) = 2.46 \cdot 10^{17} \cdot {M_0}^{1/3}\,(dyne \cdot cm) \tag{2}$$

The acceleration level A_0 was theoretically related to the combined asperity areas and the stress drop in the asperities for a circular asperity by Madariaga (1977).

$$A_0^a = 4\sqrt{\pi}\beta v_r \Delta\sigma_a \sqrt{S_a} \tag{3}$$

By putting together the relationships $A_0 \propto {M_0}^{1/3}$ and ${A_0}^a \propto {M_0}^{1/3}$, which were obtained empirically (Irikura and Miyake, 2001), the combined area of the asperities can be estimated as follows.

$$S_a = \left(\frac{7\pi^2}{4}\beta v_R\right)^2 \cdot \frac{(M_0)^2}{S \cdot ({A_0}^a)^2} \tag{4}$$

In this case the stress drop is also given by (1).

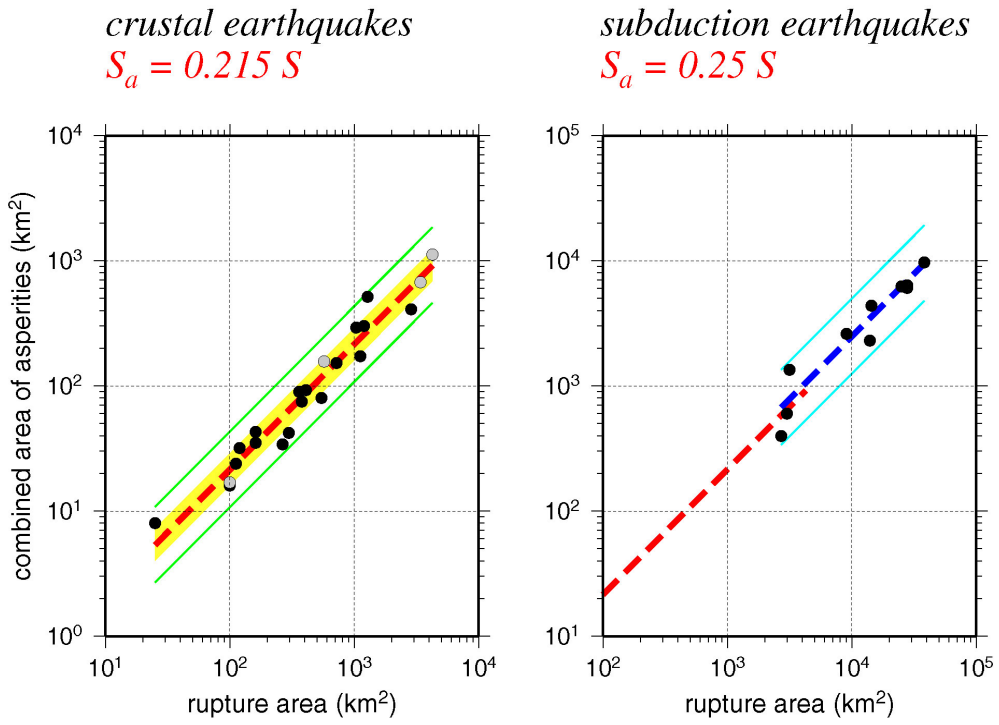

Figure 4. Empirical relationships between the combined area of the asperities and the total rupture area (thick broken line) for inland crustal earthquakes (left: after Irikura and Miyake, 2001) and subduction-zone earthquakes (right). Shaded areas represent $\pm\sigma$ (standard deviation). The thin solid lines show a factor of 2 and 1/2 for the average. The database obtained by waveform inversions for inland crustal earthquakes is from Somerville *et al*. (1999) and Miyakoshi (2002), and that for subduction-zone earthquakes is from Somerville *et al*. (2002).

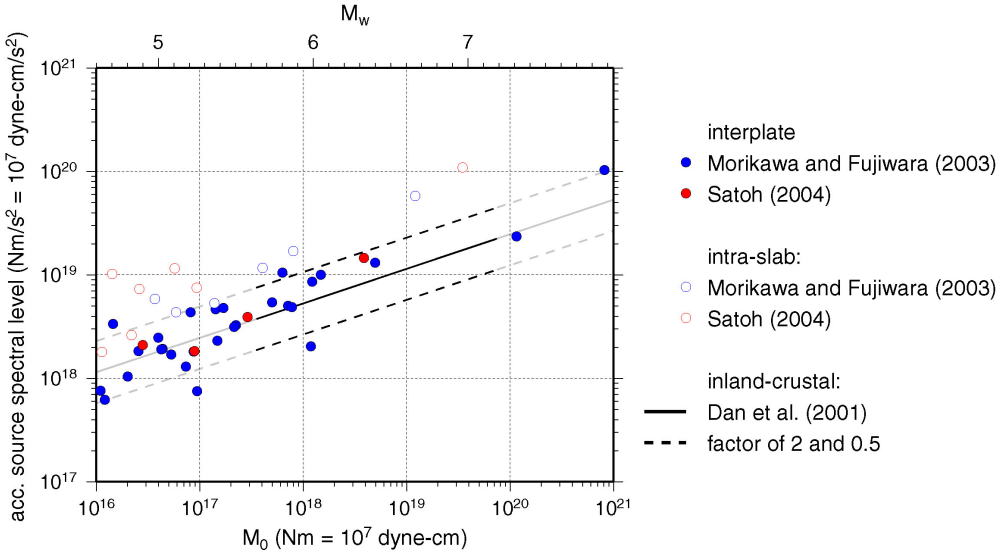

Figure 5. Empirical relationships between seismic moment and acceleration source spectral level for inland crustal earthquakes and for subduction-zone earthquakes.

Recipe for Source Modeling

The procedure for characterizing the source model is outlined as a recipe for estimating the three kinds of source parameters, outer, inner, and extra fault parameters, as follows:

Outer Fault Parameters - Estimation of Seismic Moment for Possible Earthquake

Step 1: Total Rupture Area ($S = LW$)

The total fault length L of the possible earthquake is defined as the sum of the lengths of the fault segments, grouping those simultaneously activated. The fault width W is related to the total fault length before reaching the thickness of the seismogenic zone W_{max} and saturated at $W_{max}/\sin\theta$, where θ is the dip angle.

$$W\,(\mathrm{km}) = L \quad (\mathrm{km}) \qquad \text{for } L < W_{max}$$
$$W\,(\mathrm{km}) = W_{max}/\sin\theta\,(\mathrm{km}) \qquad \text{for } L >= W_{max} \qquad (5)$$

Step 2: Total Seismic Moment (M_0)

The total seismic moment is estimated from the relationship between the seismic moment and rupture area (Fig. 3(a) and (b)).

Step 3: Average Stress Drop ($\Delta\bar{\sigma}_c$) on the Fault

The average static stress-drop for the rupture area is estimated by the formula for a circular crack model given by Eshelby (1957) in the first stage, and then by other formulae considering the tectonic loading stress (e.g., Fujii and Matsu'ura, 2000) at the second and third stages, to naturally explain the 3-stage scaling relationships of the seismic moment and rupture area.

Inner Fault Parameters - Slip Heterogeneity or Roughness of Faulting

Step 4. Combined Area of Asperities (S_a)

Two methods are used to determine the combined area of asperities. One is from the empirical relation of Sa-S (Somerville *et al*. 1999; Irikura and Miyake 2001), where the combined area of asperities is specified to be about 22%. The other is from equation (4), which estimates the acceleration level from empirical relations or observed records.

Step 5. Stress Drop on Asperities ($\Delta\sigma_a$)

As shown in equation (1), $\Delta\sigma_a$, as the inner fault parameter, is derived by multiplying $\Delta\bar{\sigma}_c$, as the outer fault parameter, by S_a/S from Step 4.

Step 6. Number of Asperities (N)

The asperities in the entire fault rupture are related to the segmentation of the active faults. The locations of the asperities are assumed from various kinds of

information, such as the surface offsets measured along a fault, the back-slip rate found by GPS observations, and the weak reflection coefficients in the fault plane.

Step 7: Average Slip on Asperities (D_a)

The average slip on asperities is based on Step 6 and the empirical relationships from the dynamic simulations of the slip distribution for the multiple-asperity source model (Dalguer et al, 2004).

(Examples: $D_a/D = 2.3$ for $N = 1$, $D_a/D = 2.0$ for $N = 2$, $D_a/D = 1.8$ for $N = 3$)

Step 8: Effective Stress on Asperity (σ_a) and Background Slip Areas (σ_b)

The effective stress (σ_a) on an asperity for strong motion generation is considered to be identical to the stress drop on the asperity ($\Delta\sigma_a$). The effective stress on a background slip area is constrained by the empirical relationship between the seismic moment and acceleration source spectral level.

Step 9: Parameterization of Slip-Velocity Time Functions

The Kostrov-like slip-velocity time functions are assumed to be functions of the peak slip-velocity and risetime based on the dynamic simulation results of Day (1982). The peak slip-velocity is given as the effective stress, rupture velocity, and f_{max}.

Extra Fault Parameters - Propagation Pattern of Rupture

The extra fault parameters of the rupture starting point and rupture velocity are used to characterize the rupture propagation pattern in the fault plane. For inland crustal earthquakes, the rupture nucleation and termination are related to the geomorphology of the active faults (e.g., Nakata *et al*., 1998; Kame and Yamashita, 2003). For subduction earthquakes, the information from past earthquakes is applied as much as possible.

Applicability and Validity of "Recipe"

The "recipe" proposed here was applied to the creation of deterministic seismic-hazard maps for specific seismic source faults with a high probability of occurrence for the National Seismic Hazard Maps for Japan (2005). The distributions of ground shaking levels, such as the PGV and seismic intensity, were evaluated for 10 inland crustal earthquakes and 2 subduction earthquakes. The applicability of the "recipe" was tested in each case by a comparison between the PGVs of the synthesized motions and those derived from the empirical attenuation relationship by Si and Midorikawa (1999).

A more detailed examination was attempted to show the validity and

applicability of the "recipe" by comparing simulated ground motions with those observed for inland crustal earthquakes and subduction earthquakes. We introduce two cases, the 1995 Kobe earthquake as an inland earthquake example and the 2003 Tokachi-oki earthquake as a subduction earthquake example.

1995 Kobe earthquake (M_w 6.9)

The source slip model of this earthquake was determined from the inversion of strong ground motion data by several researchers (e.g., Sekiguchi *et al*., 1996; Yoshida *et al*.,1996). The slip distributions on the fault plane were roughly similar to each other, although there were clear differences based on the frequency range of the data, the smoothing techniques used, etc. Even if the inverted source model was almost uniquely determined, it was not always available for strong motion simulation. The inversion was usually done using only long-period motions of more than 1 sec. Therefore, it might not be useful for broadband motions that include short-period motions of less than 1 sec, which are of interest to engineers.

Thus, for broadband ground motions, we referred to the slip model derived from forward modeling using the empirical Green's function method (Kamae and Irikura, 1998). This model consists of three segments, two on the Kobe side and one on the Awaji side, as shown in Fig. 6(a). The outer parameters included a total rupture of 51 x 20.8 km^2 and total seismic moment of 3.29 10^{23} MPa, assuming that $\Delta\overline{\sigma}_c$ was 2.3 MPa, following Steps 1, 2, and 3. Next, the inner fault parameters were given as a Sa/S value of 0.22, a $\Delta\sigma_a$ value of 10.5 MPa, with 3 asperities and the other parameters given in the rest of Steps 4 through 9. The stress drop of the background area was estimated to be about 4.0 MPa from the difference between the stress drop of the asperity from (1) and that from (3) and (4) using the empirical relation, acceleration level vs. seismic moment, by Dan *et al*. (2001). The stress drop of the background area was 0.0 for Model 1 and 4.0 for Model 4. The source parameters mentioned above are summarized in Fig. 6(b).

The strong ground motions were calculated using the stochastic Green's function method (Kamae *et al*., 1998). In this method, the Green's functions are stochastically calculated based on band-limited-white-noise with spectra following the omega-square model and site effects empirically estimated from the observation records for small events. Fig. 6(c) compares the synthesized acceleration and velocity motions for Models 1 and 4 with the observed motions at KBU, which was close to the source fault. The right side of Fig. 6(c) shows that there was a very good fit between the synthesized and observed velocity motions, both of which have two significant

directivity pulses caused by two asperities in the forward rupture direction. We found that the most important parameters for the strong ground motions were the sizes of the asperities and the effective stress on each asperity, which characterize the amplitudes and periods of the directivity pulses causing earthquake damage. On the other hand, the left side of Fig. 6(c) shows that the synthesized acceleration motions had peaks larger than the observed ones. There are two possibilities for the overestimation of the acceleration motions. One is that a uniform rupture velocity might cause the directivity effect from an asperity near KBU to the synthesized acceleration motions to be too strong. The other possibility is that the overestimation is due to the non-linear behavior of soil layers near the surface. Such high frequency motions are less effective for the evaluation of the instrumental seismic intensity.

(a)

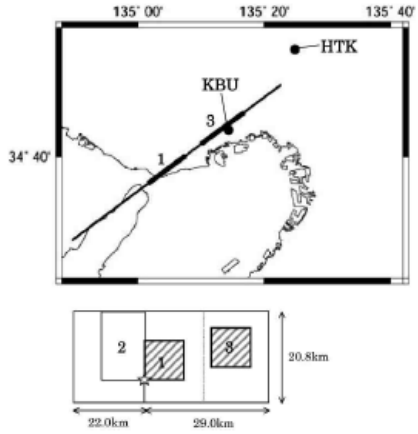

(b)

	M_0 dyne-cm	S km²	D cm	$\Delta\sigma$ MPa	A dyne-cm/sec²
total fault area	3.29×10^{26}	1062	103	2.3	1.70×10^{26}
segment 1 (total)	8.43×10^{25}	300	94	2.3	9.03×10^{25}
(asperity)	3.57×10^{25}	64	186	10.5	7.29×10^{25}
(background)	4.86×10^{25}	236	69	4.0	5.33×10^{25}
segment 2 (total)	1.60×10^{26}	462	115	2.3	1.12×10^{26}
(asperity)	6.96×10^{25}	100	232	10.5	9.12×10^{25}
(background)	9.04×10^{25}	362	83	4.0	6.50×10^{25}
segment 3 (total)	8.43×10^{25}	300	94	2.3	9.03×10^{25}
(asperity)	3.57×10^{25}	64	186	10.5	7.29×10^{25}
(background)	4.86×10^{25}	236	69	4.0	5.33×10^{25}

(c) (d)

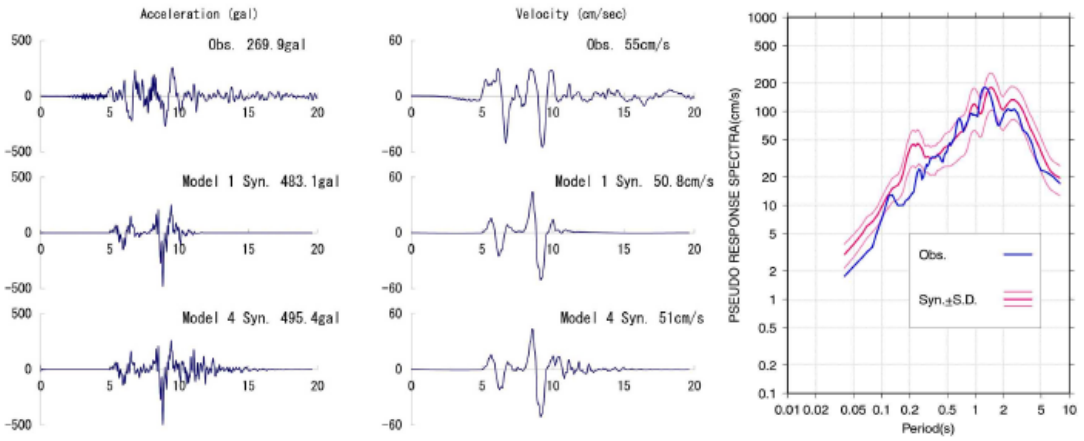

Figure 6. Ground motion simulation for the 1995 Kobe earthquake using the stochastic Green's function method. (a) Characterized source model based on Kamae and Irikura (1998). (b) Source

parameters for synthetic motions. (c) Comparison between observed and synthetic velocities of NS component at KBU station. (d) Variability of synthetic pseudo-velocity response spectra using 10 trials of stochastic Green's functions (after Irikura *et al*., 2002).

The variability of the synthesized pseudo-velocity response spectra calculated with 10 trials of the stochastic Green's functions is shown with the observed ones in Fig. 6(d). The observed ones ranged within one standard deviation at periods longer than 0.2 sec, which are effective for measuring seismic intensity. The large deviations of the synthesized motions at higher frequencies coincide with the overestimation of the acceleration motions. We found that the strong ground motions from the Kobe earthquake calculated using the "recipe" were practical for predicting the distribution of the seismic intensity.

2003 Tokachi-oki Earthquake (M_w 8.0)

So far, very few strong motion records from seismic-zone earthquakes have been obtained anywhere in the world. Therefore, we only have the less accurate inversion results of slip models for subduction-zone earthquakes. The 2003 Tokachi-oki earthquake provided many strong ground motion records near the source area. Slip models for this earthquake have been proposed by several researchers, using strong motion records (e.g., Honda *et al*., 2004), teleseismic data (e.g., Yamanaka and Kikuchi, 2003), joint inversions of strong motion and teleseismic data (e.g., Yagi, 2004), strong motion and geodetic data (Koketsu *et al*., 2004), and so on. Their results provided us with a great opportunity to discuss the validity and applicability of the recipe to subduction-zone earthquakes.

Verification of the strong ground motion estimation for this earthquake based on the "recipe" was shown in the National Seismic Hazard Map (2005) by the Earthquake Research Committee (2005). We next summarize this verification. The location and geometry of the seismic source fault was referred to by Honda *et al*. (2004), as shown at the bottom right of Fig. 7. The rupture initiation point was taken as the epicenter determined by the Japan Meteorological Agency.

The order used to set the outer fault parameters is somewhat different from that for inland earthquakes. The most stable and reliable parameter was the seismic moment, which had a value of 1.05 10^{21} N-m, according to an analysis of the teleseismic data by Kikuchi and Yamanaka (2003). The rupture area was given to be 9000 km^2, assuming a $\Delta\bar{\sigma}_c$ of 3.0 MPa (Kanamori and Anderson, 1975), in the order of Step 2, Step 3, and Step 1 for the outer fault parameters.

The inner fault parameters are given as follows. First, the number of asperities was assumed to be three, based on the source inversion results (Yamanaka and Kikuchi, 2003; Honda *et al*., 2004; Koketsu *et al*., 2004; Yagi, 2004). The locations of those three asperities were set, as shown by the solid circles inside the source fault in Fig. 7, by referring to the results of forward modeling using the empirical Green's function method by Kamae and Kawabe (2004). The large asperity had an area of 361.2 km^2 and the other two asperities had areas that were half the size of the large one. The stress drop of each asperity was estimated to be 37.4 MPa from the empirical relation Mo vs. acceleration level, following Steps 4 and 5. The rest of parameters were given by the "recipe."

The synthesized motions were calculated using a hybrid method (Irikura and Kamae, 1999) with a crossover period of 5 sec, summing up longer period motions with a theoretical procedure and shorter period motions with the stochastic Green's function method. Examples are shown in Fig. 7, in which a comparison is made between the waveforms and pseudo-velocity-response spectra of the observed and synthesized motions at three sites, TKCH11, HDKH05, and HKD093, very near the source fault. We found that the synthesized motions agreed well with the observation records.

The instrumental seismic intensity distributions estimated from the observed records and synthesized motions are shown at the left of Fig. 8. A comparison of the seismic intensity between the observation records and the synthesized data is shown at the right of Fig. 8. The seismic intensities from the synthesized motions were generally consistent with the observed ones. However, we can see overestimated synthesized motions in some regions that contain thick underlying sedimentary layers. This might be due to the empirical formula for estimating instrumental seismic intensity from peak ground velocity. This formula tends to overestimate the instrumental seismic intensity with respect to ground motions having predominant periods longer than 2 s.

There are still many other problems to solve in order to apply the "recipe" to subduction-zone earthquakes. One of the difficulties is specifying the number of asperities and their locations when no historical records exist. The other problems comes from the lack of a deep basin and off-shore structures from the source areas to objective regions, detailed geometries of plate boundaries, and so on.

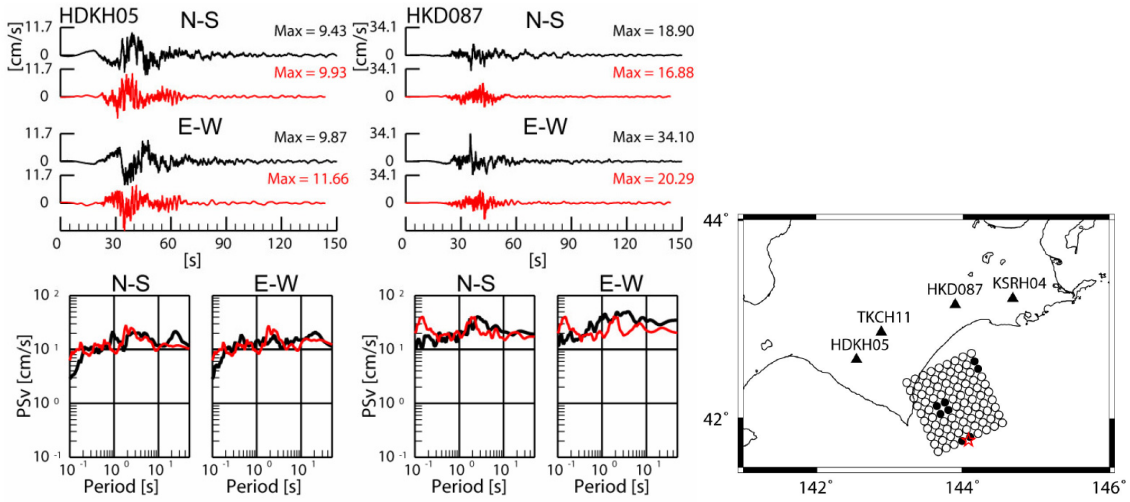

Figure 7. Comparison of observed (black) and simulated (red) velocity ground motions and pseudo-velocity response spectra (PSv, h = 0.05) for the 2003 Tokachi-oki earthquake (after Morikawa *et al*., 2006). A map showing the source model and observation stations is at the right (after Morikawa *et al*., 2007).

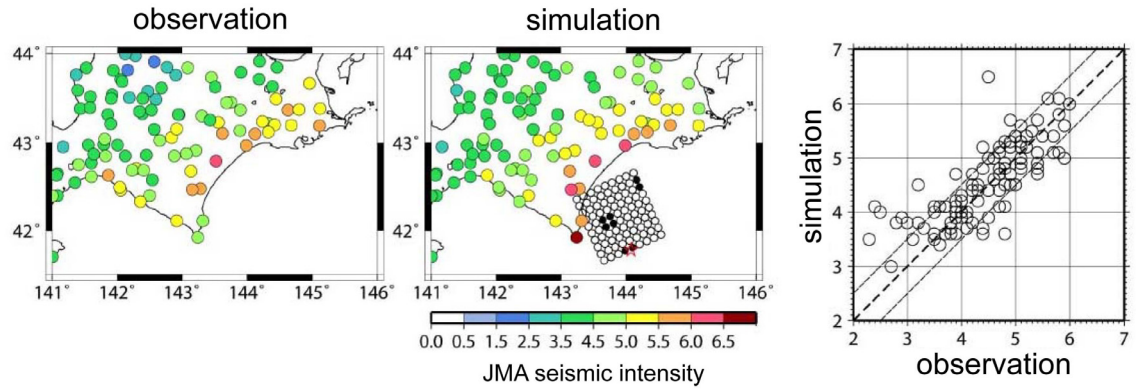

Figure 8. Comparison of observed and simulated seismic intensities for the 2003 Tokachi-oki earthquake. Distribution of the JMA seismic intensities from observed records (left) and simulated (middle) ground motions at the ground surface. Right: comparison of observed and simulated JMA seismic intensities (after Morikawa *et al*., 2007).

Conclusions

A "recipe" for predicting the strong ground motions from future large earthquakes was constructed based on recent findings in earthquake source physics in seismology and structural damage mechanisms in earthquake engineering. Two kinds of scaling relationships were found from the source process results by the waveform inversion using strong motion data. These were the seismic moment Mo versus the entire source area S for the outer fault parameters, and the Mo versus asperity areas Sa for the inner fault parameters.

The source model was defined by three kinds of parameters: outer, inner, and extra fault parameters, following the "recipe" based on those scaling relationships. In this study, the validity and applicability of the procedures for characterizing the earthquake sources based on the "recipe" were examined in comparison with the observation records and broadband simulated motions for the 1995 Kobe and 2003 Tokachi-oki earthquakes.

The ground motions synthesized by following the "recipe" for the 1995 Kobe earthquake were consistent with the observation records for the velocity and seismic intensity but the acceleration was overestimated. The most important parameters for the strong ground motions were the sizes of the asperities and the effective stress on each asperity, which characterizes the amplitudes and periods of directivity pulses causing earthquake damage.

As an example of a subduction earthquake, the ground motions of the 2003 Tokachi-oki earthquake were successfully simulated based on the "recipe," showing good agreement between the observed and synthetic spatial patterns of seismic intensity, as well as for the waveforms. However, we need a priori information to specify the number of asperities and their locations, as well as the location and geometry of the source fault. It is very difficult to specify such source parameters when no historical records exist.

References

Central Disaster Prevention Research Institute (2003). Estimated Seismic Intensity Distribution in the case of Simultaneous Occurrence of Three earthquakes, Tokai, Tonankai, and Nankai, *16th Special Survey Committee of Tonankai and Nankai earthquake*, http://www.bousai.go.jp/jishin/chubou/nankai/16/index.html (in Japanese).

Dalguer, L. A., H. Miyake, and K. Irikura (2004), Characterization of dynamic asperity source models for simulating strong ground motions, *Proceedings of the 13th World Conference on Earthquake Engineering*, No.3286, CD-ROM.

Dan, K., M. Watanabe, T. Sato, and T. Ishii (2001). Short-period source spectra inferred from variable-slip rupture models and modeling of earthquake fault for strong motion prediction, *Journal of Struct. Constr. Eng. AIJ*, **545**, 51-62.

Das, S. and B. V. Kostrov (1986). Fracture of a single asperity on a finite fault, in *Earthquake Source Mechanics*, Geophysical Monograph 37, Maurice Ewing Series 6, American Geophysical Union, 91-96.

Day, S. M. (1982). Three-dimensional simulation of spontaneous rupture: the effect of

nonuniform prestress, *Bull. Seismol. Soc. Am.*, **88**, 512-522.

Earthquake Research Committee (2005). National Seismic Hazard Map for Japan (2005), *Report published by the Headquarters of Earthquake Research Promotion under the Ministry of Education, Culture, Sports, Science, and Technology*, 121p. (in Japanese).

Earthquake Research Committee (2005). Verification results using observed records of the 2003 Tokachi-Oki Earthquake, *National Seismic Hazard Map for Japan (2005)*, http://www.jishin.go.jp/main/index-e.html.

Eshelby J. D. (1957), The determination of the elastic field of an ellipsoidal inclusion, and related problems, *Proc. Roy Soc.*, **A241**, 376-396.

Fujii, Y. and M. Matsu'ura (2000). Regional difference in scaling laws for large earthquakes and its tectonic implication, *PAGEOPH*, **157**, 2283-2302.

Hanks, T. C. and W. H. Bakun (2002). A bilinear source-scaling model for *M*-logA observations of continental earthquakes, *Bull. Seismol.. Soc. Am*, **92**, 1841-1846.

Honda, R., S. Aoi, N. Morikawa, H. Sekiguchi, K. Kunugi, and H. Fujiwara (2004). Ground motion and rupture process of the 2003 Tokachi-oki earthquake obtained from strong motion data of the K-NET and KiK-net, *Earth Planets Space*, **56**, 317-322.

Irikura, K. (2004). Recipe for predicting strong ground motion from future large earthquake, *Annuals of Disaster Prevention Research Institute*, **47A**, 25- 45 (in Japanese with English abstract).

Irikura, K. (2006). Predicting strong ground motions with a “Recipe”, *Bull. Earthq. Res. Inst. Univ. Tokyo*, **81**, 341-352.

Irikura, K. and K. Kamae (1999). Strong ground motions during the 1948 Fukui earthquake, *Zisin*, **52**, 129-150 (in Japanese with English abstract).

Irikura, K. and H. Miyake (2001). Prediction of strong ground motions for scenario earthquakes, *Journal of Geography*, **110**, 849-875 (in Japanese with English abstract).

Kame, N. and T. Yamashita (2003). Dynamic branching, arresting of rupture and the seismic wave radiation in self-chosen crack path modeling, *Geophys. J. Int.*, **155**, 1042-1050.

Kamae, K. and K. Irikura (1998). Rupture process of the 1995 Hyogo-ken Nanbu earthquake and simulation of near-source ground motion, *Bull. Seismol. Soc. Am.*, **88**, 400-412.

Kamae, K., K. Irikura, and A. Pitarka (1998). A technique for simulating strong ground motion using hybrid Green's function, *Bull. Seismol. Soc. Am.*, **88**, 357-367.

Kamae, K. and H. Kawabe (2004). Source model composed of asperities for the 2003 Tokachi-oki, Japan, earthquake (M_{JMA}=8.0) estimated by the empirical Green's

function method, *Earth Planets Space*, **56**, 323-327.

Kanamori, H. and D. L. Anderson (1975). Theoretical basis of some empirical relations in seismology, *Bull. Seismol. Soc. Am*., **86**, 1073-1095.

Kikuchi, M. and Y. Yamanaka (2001). Rupture processes of past large earthquakes = Identification of asperities, *Seismo*, **5**, 6-7 (in Japanese).

Koketsu, K., K. Hikima, S. Miyazaki, and S. Ide (2004). Joint inversion of strong motion and geodetic data for the source rupture process of the 2003 Tokachi-oki, Hokkaido, earthquake, *Earth Planets Space*, **56**, 329-334.

Madariaga, R. (1977). High frequency radiation from crack (stress drop) models of earthquake faulting, *Geophys. J. R. Astron. Soc*., **51**, 625-651.

Madariaga, R. (1979). On the relation between seismic moment and stress drop in the presence of stress and strength heterogeneity, *J. Geophys. Res*., **84**, 2243-2250.

Miyake, H., T. Iwata, and K. Irikura (2001). Estimation of rupture propagation direction and strong motion generation area from azimuth and distance dependence of source amplitude spectra, *Geophys. Res. Lett*., **28**, 2727-2730.

Miyake H, T. Iwata, and K. Irikura (2003). Source characterization for broadband ground-motion simulation: Kinematic heterogeneous source model and strong motion generation area, *Bull. Seismol. Soc. Am*., **93**, 2531-2545.

Miyakoshi, K., T. Kagawa, H. Sekiguchi, T. Iwata, and K. Irikura (2000). Source characterization of inland earthquakes in Japan using source inversion results, *Proc. 12th World Conf. Earthq. Eng*. (CD-ROM).

Morikawa N. and H. Fujiwara (2003). Source and path characteristics for off Tokachi-Nemuro earthquakes, *Programme and Abstracts for the Seismological Society of Japan, 2003 Fall Meeting*, 104 (in Japanese).

Morikawa, N., H. Fujiwara, S. Kawai, S. Aoi, T. Kunugi, T. Ishii, Y. Hakayawa, R. Honda, K. Kobayashi, M. Ooi, S. Senna, and N. Okumura (2007). Application of the strong-motion prediction method to the 2003 Tokachi-oki earthquake, *Technical Note of the National Research Institute for Earth Science and Disaster Prevention*, **303,** 149pp.

Nakata, T., K. Shimazaki, Y. Suzuki, and E. Tsukuda (1998). Fault branching and directivity of rupture propagation, *Journal of Geography,* **107**, 512-528 (in Japanese with English abstract).

Satoh, T. (2004). Short-period spectral level of intraplate and interplate earthquakes occurring off Miyagi prefecture, *Journal of JAEE*, **4**, 1-4 (in Japanese with English abstract).

Scholz, C. H. (1982). Scaling laws for large earthquakes: Consequences for physical

models, *Bull. Seismol. Soc. Am*., **72**, 1-14.

Scholz C. H. (2002). *The mechanics of earthquakes and faulting*, Cambridge University Press.

Sekiguchi, H., K. Irikura, and T. Iwata (2000). Fault geometry at the rupture termination of the 1995 Hyogo-ken Nanbu earthquake, *Bull. Seismol. Soc. Am*., **90**, 974-1002.

Si, H. and S. Midorikawa (1999). New attenuation relationships for peak ground acceleration and velocity considering effects of fault type and site condition, *J. Struct. Constr. Eng., AIJ*, **523**, 63-70 (in Japanese with English abstract).

Somerville, P., K. Irikura, R. Graves, S. Sawada, D. Wald, N. Abrahamson, Y. Iwasaki, T. Kagawa, N. Smith, and A. Kowada (1999). Characterizing earthquake slip models for the prediction of strong ground motion, *Seismol. Res. Lett*., **70**, 59-80.

Somerville, P. G., T. Sato, T. Ishii, N. F. Collins, K. Dan and H. Fujiwara (2002). Characterizing heterogeneous slip models for large subduction earthquakes for strong ground motion prediction, *Proc. 11th Japan Earthquake Symposium* (in Japanese with English abstract).

Wells, D. L. and K. J. Coppersmith (1994). New empirical relationships among magnitude, rupture length, rupture width, rupture area, and surface displacement, *Bull. Seismol. Soc. Am*., **84**, 974-1002.

Yagi, Y. (2004). Source rupture process of the 2003 Tokachi-oki earthquake determined by joint inversion of teleseismic body wave and strong ground motion data, *Earth Planets Space*, **56**, 311-316.

Yamanaka, Y. and M. Kikuchi (2003). Source process of the recurrent Tokachi-oki earthquake on September 26, 2003, inferred from teleseismic body waves, *Earth Planets Space*, **55**, e21–e24.

Yoshida, S., K. Koketsu, B. Shibazaki, T. Sagiya, T. Kato, and Y. Yoshida (1996). Joint inversion of the near- and far-field waveforms and geodetic data for the rupture process of the 1995 Kobe earthquake, *J. Phys. Earth*, **44**, 437-454.

Lecture Note on Strong Motion Seismology by Kojiro Irikura and Hiroe Miyake

Chapter 2

Figure 4: after Figure 3 of Miyake et al. (1999, Zisin)

Miyake, H., T. Iwata, and K. Irikura (1999). Strong ground motion simulation and source modeling of the Kagoshima-ken Hokuseibu earthquakes of march 26 (MJMA6.5) and May 13 (MJMA6.3), 1997, using empirical Green's function method, *Zisin*, **51**, 431-442 (in Japanese with English abstract).

Figure 5: after Figure 4 of Miyake et al. (1999, Zisin)

Miyake, H., T. Iwata, and K. Irikura (1999). Strong ground motion simulation and source modeling of the Kagoshima-ken Hokuseibu earthquakes of march 26 (MJMA6.5) and May 13 (MJMA6.3), 1997, using empirical Green's function method, *Zisin*, **51**, 431-442 (in Japanese with English abstract).

Figure 6: after Figure 12 of Miyake et al. (1999, Zisin)

Miyake, H., T. Iwata, and K. Irikura (1999). Strong ground motion simulation and source modeling of the Kagoshima-ken Hokuseibu earthquakes of march 26 (MJMA6.5) and May 13 (MJMA6.3), 1997, using empirical Green's function method, *Zisin*, **51**, 431-442 (in Japanese with English abstract).

Figure 7: after Figure 6 of Miyake et al. (2003, BSSA)

Miyake H, T. Iwata, and K. Irikura (2003). Source characterization for broadband ground motion simulation: Kinematic heterogeneous source model and strong motion generation area, *Bull. Seismol. Soc. Am.*, **93**, 2531-2545

Figure 8: after Figure 10 of Miyake et al. (2003, BSSA)

Miyake H, T. Iwata, and K. Irikura (2003). Source characterization for broadband ground motion simulation: Kinematic heterogeneous source model and strong motion generation area, *Bull. Seismol. Soc. Am.*, **93,** 2531-2545

Chapter 3

Figure3: after Figure2 of Kawabe and Kamae (2008, Journal of Seismology)

Kawabe, H. and K. Kamae (2008), Prediction of long-period ground motions from huge subduction ,earthquakes in Osaka, Japan, *Journal of Seismology* **12** (2): 173-184 (2008) DOI 10.1007/s10950-008-9089-z

Publisher Springer Netherlands
http://www.springerlink.com/content/v6776852640n1875/

Figure 4: after Figure 4 of Kawabe and Kamae (2008, Journal of Seismology)

Kawabe, H. and K. Kamae (2008), Prediction of long-period ground motions from huge subduction ,earthquakes in Osaka, Japan, *Journal of Seismology* **12** (2): 173-184 (2008) DOI 10.1007/s10950-008-9089-z
Publisher Springer Netherlands
http://www.springerlink.com/content/v6776852640n1875/

Figure 5: after Figure 4 of Kawabe and Kamae (2008, Journal of Seismology)

Kawabe, H. and K. Kamae (2008), Prediction of long-period ground motions from huge s subduction ,earthquakes in Osaka, Japan, *Journal of Seismology* **12** (2): 173-184 (2008) DOI 10.1007/s10950-008-9089-z
Publisher Springer Netherlands
http://www.springerlink.com/content/v6776852640n1875/

Figure 6: after Figure 5 of Kawabe and Kamae (2008, Journal of Seismology)

Kawabe, H. and K. Kamae (2008), Prediction of long-period ground motions from huge s subduction ,earthquakes in Osaka, Japan, *Journal of Seismology* **12** (2): 173-184 (2008) DOI 10.1007/s10950-008-9089-z
Publisher Springer Netherlands
http://www.springerlink.com/content/v6776852640n1875/

Figure 7: after Figure 6 of Kawabe and Kamae (2008, Journal of Seismology)

Kawabe, H. and K. Kamae (2008), Prediction of long-period ground motions from huge subduction ,earthquakes in Osaka, Japan,
Journal of Seismology **12** (2): 173-184 (2008) DOI 10.1007/s10950-008-9089-z
Publisher Springer Netherlands
http://www.springerlink.com/content/v6776852640n1875/

Figure 8: after Figure 7 of Kawabe and Kamae (2008, Journal of Seismology)

Kawabe, H. and K. Kamae (2008), Prediction of long-period ground motions from huge subduction ,earthquakes in Osaka, Japan, *Journal of Seismology* **12** (2): 173-184 (2008) DOI 10.1007/s10950-008-9089-z
Publisher Springer Netherlands

http://www.springerlink.com/content/v6776852640n1875/

Figure 9: after Figure 8 of Kawabe and Kamae (2008, Journal of Seismology)

Kawabe, H. and K. Kamae (2008), Prediction of long-period ground motions from huge s subduction ,earthquakes in Osaka, Japan,
Journal of Seismology **12** (2): 173-184 (2008) DOI 10.1007/s10950-008-9089-z
Publisher Springer Netherlands
http://www.springerlink.com/content/v6776852640n1875/

Figure 10: after Figure 9 of Kawabe and Kamae (2008, Journal of Seismology)

Kawabe, H. and K. Kamae (2008), Prediction of long-period ground motions from huge subduction ,earthquakes in Osaka, Japan,
Journal of Seismology **12** (2): 173-184 (2008) DOI 10.1007/s10950-008-9089-z
Publisher Springer Netherlands
http://www.springerlink.com/content/v6776852640n1875/

Figure 11: after Figure 10 of Kawabe and Kamae (2008, Journal of Seismology)

Kawabe, H. and K. Kamae (2008), Prediction of long-period ground motions from huge s subduction ,earthquakes in Osaka, Japan,
Journal of Seismology **12** (2): 173-184 (2008) DOI 10.1007/s10950-008-9089-z
Publisher Springer Netherlands
http://www.springerlink.com/content/v6776852640n1875/

Chapter 4

Figure 1: after Figure 1 of Kamae et al. (1998, BSSA)

Kamae, K., K. Irikura, and A. Pitarka (1998). A technique for simulating strong ground motion using hybrid Green's function, *Bull. Seismol. Soc. Am.*, **88**, 357-367.

.

Figure 2: after Figure 2 of Kamae et al. (1998, BSSA)

Kamae, K., K. Irikura, and A. Pitarka (1998). A technique for simulating strong ground motion using hybrid Green's function, *Bull. Seismol. Soc. Am.*, **88**, 357-367.

Figure 3: after Figure 3 of Kamae et al. (1998, BSSA)

Kamae, K., K. Irikura, and A. Pitarka (1998). A technique for simulating strong ground motion

using hybrid Green's function, *Bull. Seismol. Soc. Am*., **88**, 357-367.

Figure 4: after Figure 4 of Kamae et al. (1998, BSSA)

Kamae, K., K. Irikura, and A. Pitarka (1998). A technique for simulating strong ground motion using hybrid Green's function, *Bull. Seismol. Soc. Am*., **88**, 357-367.

Figure 5: after Figure 8 of Kamae et al. (1998, BSSA)

Kamae, K., K. Irikura, and A. Pitarka (1998). A technique for simulating strong ground motion using hybrid Green's function, *Bull. Seismol. Soc. Am*., **88**, 357-367.

Figure 6: after Figure 9 of Kamae et al. (1998, BSSA)

Kamae, K., K. Irikura, and A. Pitarka (1998). A technique for simulating strong ground motion using hybrid Green's function, *Bull. Seismol. Soc. Am*., **88**, 357-367.

Figure 7: after Figure 10 of Kamae et al. (1998, BSSA)

Kamae, K., K. Irikura, and A. Pitarka (1998). A technique for simulating strong ground motion using hybrid Green's function, *Bull. Seismol. Soc. Am*., **88**, 357-367.

Figure 8: after Figure 2 of Irikura and Kamae (1999, Zisin)

Irikura, K., and K. Kamae (1999). Strong ground motions during the 1948 Fukui earthquake –Estimation of broad-band ground motion using a hybrid simulation technique, Zisin, 52, 129-150 (in Japanese with English abstract).

Figure 9: after Figure 1 of Morikawa et al. (2006, ESG)

Morikawa, N., S. Aoi, R. Honda, S. Senna, Y. Hayakawa, and H. Fujiwara (2006). Application of the ”recipe for strong ground motion evaluation” to the 2003 Tokachioki, Japan, earthquake, *Third International Symposium on the Effects of Surface Geology on Seismic Motion,* Paper No. 48.

Figure 10: after Figure of Earthquake Research Committee (2004, website)

http://www.jishin.go.jp/main/kyoshindo/04dec_tokachi/f02.pdf

Figure 11: after Figure of Earthquake Research Committee (2004, website)

http://www.jishin.go.jp/main/kyoshindo/04dec_tokachi/f06-1.pdf

Figure 12: after Figure of National Research Institute for Earth Science and Disaster Prevention (2007, website)

Morikawa et al (2007). Application of the Strong-motion Prediction Method to the 2003 Tokachi-oki Earthquake, *Technical Note of the National Research Institute for Earth Science and Disaster Prevention, National Research Institute for Earth Science and Disaster Prevention.*, **303**, 94-95.
http://dil.bosai.go.jp/library/pub/technical_note/PDF/n303.pdf

Chapter 5

Figure 1: after Figure of Earthquake Research Committee (2005, website)
http://www.jishin.go.jp/main/chousa/05mar_yosokuchizu/shubun.pdf

Figure 2: after Figure 2 of Irikura (2006, Bull. Earthq. Res. Inst. Univ. Tokyo)
Kojiro Irikura (2006). Predicting Strong Ground Motions with a "Recipe", *Bulletin of the Earthquake Research Institute, University of Tokyo,* **81**, 341-352.
http://www.eri.u-tokyo.ac.jp/BERI/pdf/IHO81320.pdf

Figure 7: after Figure of National Research Institute for Earth Science and Disaster Prevention (2007, website)
Morikawa et al (2007).Application of the Strong-motion Prediction Method to the 2003 Tokachi-oki Earthquake, Technical Note of the National Research Institute for Earth Science and Disaster Prevention, National Research Institute for Earth Science and Disaster Prevention., 303, 94-95.
http://dil.bosai.go.jp/library/pub/technical_note/PDF/n303.pdf

Figure 8: after Figure of National Research Institute for Earth Science and Disaster Prevention (2007, website)
Morikawa et al (2007).Application of the Strong-motion Prediction Method to the 2003 Tokachi-oki Earthquake, Technical Note of the National Research Institute for Earth Science and Disaster Prevention, National Research Institute for Earth Science and Disaster Prevention., 303, 93.
http://dil.bosai.go.jp/library/pub/technical_note/PDF/n303.pdf